A Multiresonance Thickness-Shear Mode (MTSM) Sensor for Monitoring the Formation of Biological Thin Films

A Thesis

Submitted to the Faculty

of

Drexel University

by

Sun Jong Kwoun

in partial fulfillment of the

requirements for the degree

of

Doctor of Philosophy

July 2006

Acknowledgments

I wish to express my gratitude to everyone who has provided me with advices, feedback, corrections, and criticism. I would like to contribute this page to acknowledge them who made my Ph.D. thesis a reality. I must single out Dr. Ryszard M. Lec who has advised, supported, and encouraged me as an academic advisor.

I also want to thank Dr. Andrzej Fertala, Department of Dermatology & Cutaneous Biology, Thomas Jefferson University, who prepared biological samples and thoughtful advises, and Dr. Richard A. Cairncross, Department of Chemical and Biological Engineering, Drexel University, who provided a thoughtful idea of an evaporation-induced deposition process model.

I am again grateful to Dr. Peter A. Lewin, Dr. Todd Doehring, School of biomedical Engineering, Science and Health Systems, Drexel University, for their academic and technical guidance, and Dr. Guoliang Yang, Department of Physics, Drexel University, for advising in the area of nanotechnology and nanometrology.

I also appreciate to all members of Biosensor Laboratory, especially Dr. Marek Swoboda who has been a best Mentor as a good all time friend, and most of all, I am deeply indebted to my family; lovely wife and kids, Sea Jin Kim, Julian, Stella, and Randy.

Table of Contents

List of Tables

List of Figures

Abstract

A Multiresonance Thickness-Shear Mode (MTSM) Sensor for Monitoring the Formation of Biological Thin Films

Sun Jong Kwoun
Ryszard M. Lec. Supervisor, Ph.D.

In this work, the development and characterization of a Multiresonance Thickness-Shear Mode (MTSM) sensor operating from approximately 10 *MHz* to 70 *MHz* is described which measures the changes in the relative resonant frequency and attenuation as signatures of the sensor. The penetration depth of the acoustic shear waves varies from tens to hundreds of nanometers, depending on the harmonic, so the sensor interrogates the surfaces loaded with biological interfaces at the nano-scale level. The theoretical analysis of MTSM has been developed to model and simulate the signature of the sensor responses at harmonics frequencies. The signature of the entire evaporation-induced deposition processes of biological samples, such as collagen and albumin, including the initial liquid like stage up to the final rigid thin film stage were investigated as case studies and the experimental data were compared with the theoretical simulations. Since the response of the MTSM depends on the interfacial processes, such as mass accumulation (density) or changes in mechanical and geometrical properties (elastic stiffness, viscosity, and thickness) the effect of mechanical and geometrical properties are

studied and analyzed using theoretical and experimental data. The MTSM responses showed qualitatively different signatures for collagen and albumin thin films. In conclusion, a MTSM sensor has exhibited many attractive measurement features for studying the kinetics of biological thin film formation processes in real time with high sensitivity and high temporal resolution and a MTSM sensor is capable to provide unique information from different depths in our experimental study.

1 INTRODUCTION

The study of interfacial processes involving biological interactions, such as the binding of enzymes, proteins, or DNA on specific binding sites and the sedimentation, attachment, or proliferation of cells on a substrate, has been growing rapidly in the last decade. Interfacial processes are strongly influenced by the dynamics of the mechanical properties of the chemical or biochemical interface that binds to the sensor surface [1-6]. Currently, most of the existing technology for the monitoring of biological interfaces are used in a variation of ways; first, to see if two or more interactants bind to each other, second, how strong the interactions are, and, third, to measure the actual association and dissociation rates [7-9].

In this work, acoustic wave devices made of piezoelectric materials have been fabricated and utilized to study the biological interfacial processes. As a main topic of this thesis the multi-harmonic operation of a thickness-shear mode (TSM) sensor has been studied to analyze the signature of the interfacial process involving biological viscoelastic (VE) inhomogeneous anisotropic media. Multi-harmonic operation enables a "*virtual slicing technique*" because the different harmonic relates to a different penetration depth within the sample. The successful interpretation of acoustic signatures obtained over a wide range of multi-harmonic frequencies may provide essential information, such as fundamental physics or mechanical properties of interfacial processes.

For the experiments with biological samples, collagen and albumin were chosen. Collagens are a family of highly characteristic fibrous proteins found in all multicellular animals [10-13]. Albumins are the main protein in human blood and the key to the regulation of blood's osmotic pressure [11, 12, 14, 15]. Generally, collagen samples are prepared in a liquid like phase and end up with a thin rigid (crystallized) film. Albumins are also prepared in a liquid like phase and end up with a thin amorphous (less rigid than collagen) film. Therefore, it is important to know the signatures and kinetics of the deposition process of biological samples as a function of time.

1.1 Biological interfaces

The study of biological interfaces has grown in importance because these interfaces play a significant role in the development of biosensors, where they provide a selective interface for the detection of various biochemical analytes [16-18]. Interactions of DNA and RNA, biocompatibility of surfaces, formation of biofilms, etc. have been the main topic of the research in the biosensor field [19-21].

The basic concept of biosensors can be explained by its two major design elements; a sensing element and a transducer (see Figure 1). The sensing element is a biologically or chemically active medium (usually a thin film), which is exposed to a target measurand. As a result, interfacial reactions take place by manifesting the changes of the bio-physical state of the sensing element. The transducer is a solid-state device, which transduces physical changes of the chemical sensing element into measurable electric signal, such as voltage, current, frequency or phase [22].

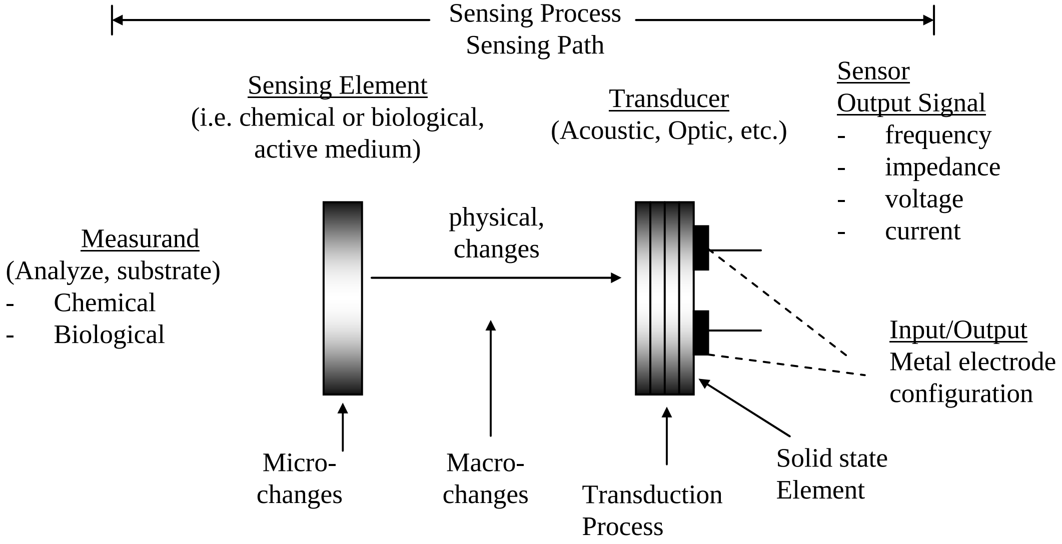

Figure 1. A conceptual model for a biosensor [23].

The research of biological interfaces is of great, practical importance to the pharmaceutical and biomedical industries. In pharmaceutical industry, it is possible to determine how and where in the body the medicine is absorbed by modifying the surface of a medicine. In the biomedical field, surface interaction also plays an important role in implantation operations. The implant must have a surface that is accepted by the body, otherwise it will be rejected. In addition, surface characteristics are involved in the emergence of infections [24]. Figure 2 shows the biological interface of piezoelectric anthrax biosensor as an example. This interface has non-uniform multi-functional multilayer structures and each layer has different bio-physical characteristics.

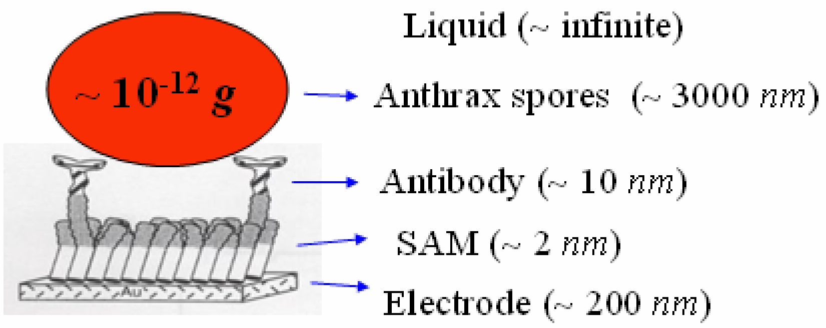

Figure 2. Piezoelectric Anthrax Biosensor with a biological interface multi-layer [25]

1.2 Thin-film deposition techniques

Thin-film deposition is a technique that deposits a thin film of material onto a substrate or onto previously deposited layers. Most deposition techniques allow layer thickness to be controlled within a few tens of nanometers, and some even allow one layer of atoms to be deposited at a time. There are many thin-film deposition techniques, such as Langmuir-Blodgett, Spinning, Sol-gel, RF & DC Sputtering Deposition System, Electron Beam, Pulsed laser deposition, Electron beam evaporator, etc. Langmuir-Blodgett technique deposits one or more monolayers of an organic material from the surface of a liquid onto a solid by immersing the solid substrate into (or from) the liquid (see image (a) in Figure 3) [26]. Sol-gel technique technology involves the transition of a system from a liquid "sol" (mostly colloidal) into a solid "gel" phase [27]. Applying the sol-gel process, it is possible to fabricate ceramic or glass materials in a variety of forms: thin film coatings or monolithic ceramics (see image (b) in Figure 3). Sputtering deposition is a physical process whereby atoms in a solid target material are ejected into the gas phase due to bombardment of the material by energetic ions (see image (c) in Figure 3) [28]. However, a common method of thin film deposition used in biochemical industry is an evaporation-induced deposition process [29, 30].

Based on the fact that the faster rate of thin film deposition process than the sputtering method, evaporation-induced deposition process is a common method of thin film deposition used in industry.

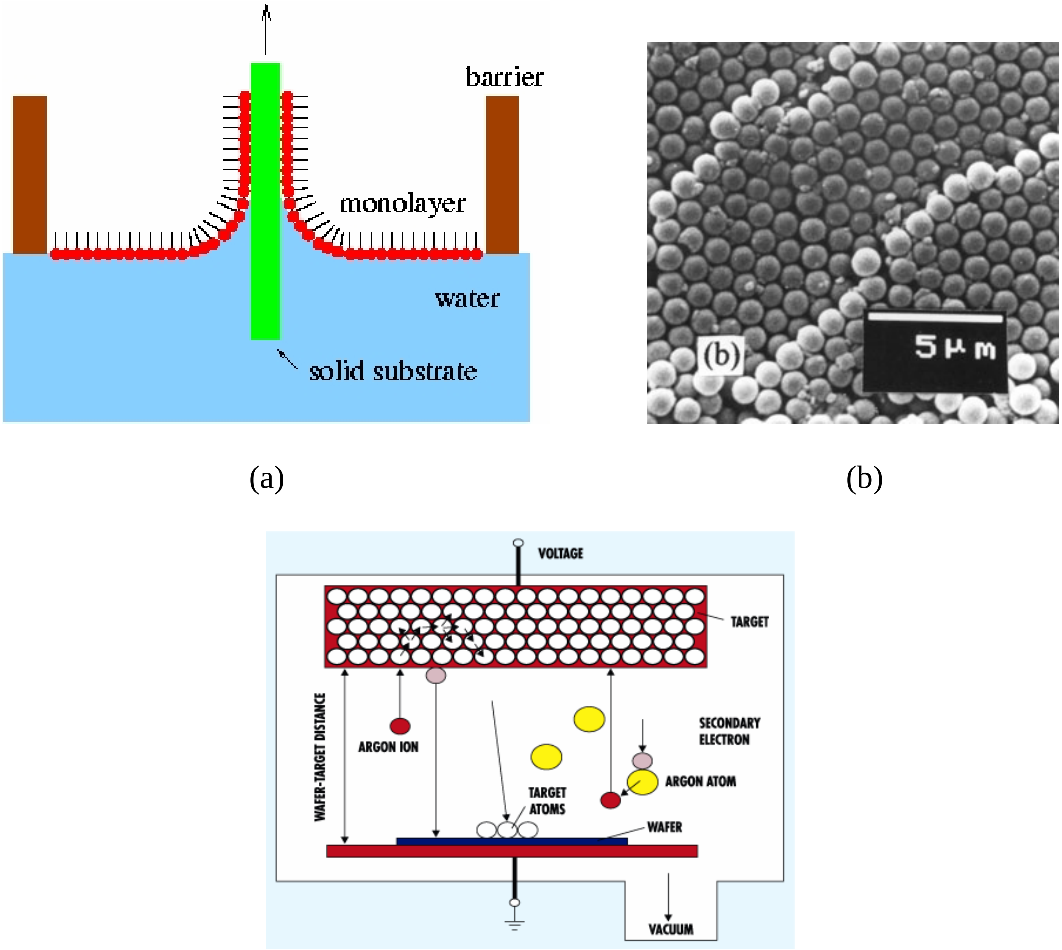

(a) (b)

(c)

Figure 3. Thin film deposition processes: (a) Langmuir-Blodgett, (b) Sol-gel, and (c) Sputtering deposition techniques [26-28].

1.3 Measurement techniques for monitoring interfacial processes

There are basically two methods that monitor the biological interfaces: optical method and other method. Optical method includes surface plasmon resonance (SPR) [8] or total internal reflection fluorescence (TIRF) [9], and other method includes piezoelectric devices [22] or atomic force microscopy (AFM) [31].

Surface Plasmon Resonance (SPR) is a technique to measure biomolecular interactions in real-time in a label free environment. While one of the interactants is immobilized to the sensor surface, the other are free in solution and passed over the surface [32]. A total internal reflection fluorescence microscope (TIRFM) is a type of microscope with which a thin region of a specimen, usually less than 200 *nm*, can be observed [9]. Atomic Force Microscopy (AFM) is a form of scanning probe microscopy where a small probe is scanned across the sample to obtain information about the sample's surface. The information gathered from the probe's interaction with the surface can be as simple as physical topography or as diverse as the material's physical properties, magnetic properties, or chemical properties [33].

However, currently existing technologies that monitor the behavior of biological media at the interface are limited with narrow measurement capabilities. In particular, direct measurements of interfacial mechanical properties of biological media or the characteristics of such processes are difficult to perform or often are unrealizable and still there are many ongoing researches in this field [1, 34]. Therefore, there is a need for developing a novel measurement technique that could provide broader and more precise measurement options with real-time measurement capabilities and a characteristic study that correlates the experimental result and theoretical model of the system and a piezoelectric TSM sensor has been studied to fulfill the above requirements in this work.

2 BACKGROUND

Generally, when piezoelectric sensors transmit acoustic waves into a medium undergoing test, the waves interact with the medium, and the measured parameters of the acoustic waves are correlated with the medium’s properties. The input signal excites an acoustic mode, then acoustic mode interacts with a medium, and the measured variation acoustic mode constitutes the piezoelectric resonator response [35, 36].

There are two basic types of acoustic wave motions, longitudinal and shear. Longitudinal waves propagate with the same direction of the particles vibration, for example, a sound wave, that is propagated in the same direction where the particles of the medium vibrate. Shear waves propagate perpendicular to the direction of propagation of the particle motion and travel slower than longitudinal waves [22]. Longitudinal waves propagate easily over long distances through a liquid. Shear waves, on the other hand, hardly propagate in liquids but rather penetrate a short distance. Therefore, shear waves monitor “local” properties of a liquid in the vicinity of the sensor.

2.1 General features of thickness-shear mode (TSM) sensors

When Acoustic Shear Waves (ASW) from a thickness-shear mode (TSM) sensor are excited into liquid media, they generally do not propagate through these media. Rather, they only penetrate a relatively short distance [22, 37-39]. This penetration depth, which typically varies from several nanometers to tens of microns in viscoelastic media, mainly depends on the mechanical properties of the medium and the frequency of the acoustic wave [40, 41].

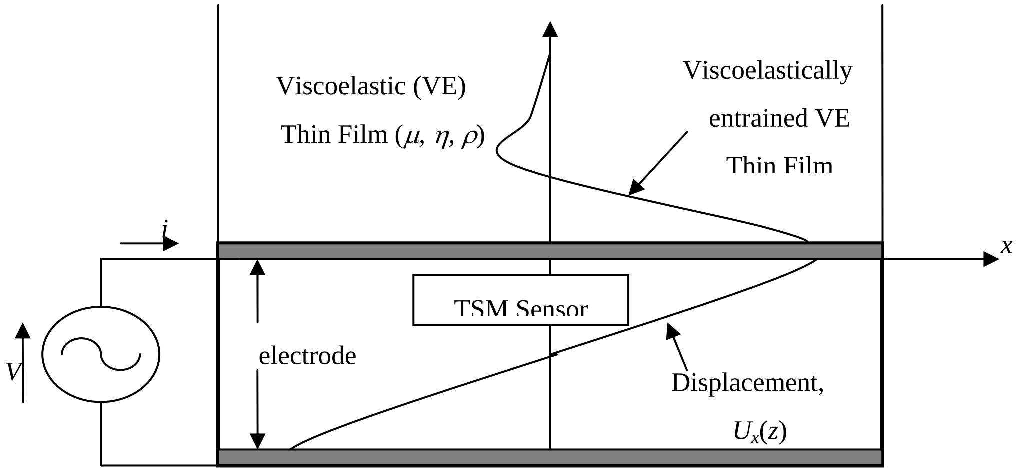

Figure 4. Penetration depth of acoustic shear waves on the TSM sensor.

These ASW are sensitive to changes occurring at the measurand-sensor interface (see Figure 4). The interfacial changes directly influence the mechanical shear vibration of the TSM sensor by affecting its mechanical impedance. The changes in the mechanical impedance of the TSM sensor are usually revealed as changes in the electrical impedance because of the intrinsic electromechanical coupling mechanism in piezoelectric materials [42, 43].

2.2 Previous work with TSM sensors

Among many researches in TSM technology, the recent application of the TSM technique to the study of shear modulus of thin film [44, 45] and polymer [46] are the most relevant to this thesis. These series of studies demonstrate the feasibility of determining the mechanical properties of viscoelastic thin film [47, 48]. Since viscoelastic material behaves either liquid-like or solid-like characteristic, by dividing the working range of TSM sensor to gravimetric (Sauerbrey region with almost linear responses) and non-gravimetric (viscoelastic region with non-linear responses), these authors have worked to relate changes in acoustic load impedance to the complex shear modulus, $G = G' + jG''$ [22]. G' represents the shear storage modulus (elastic part) whereas G'' corresponds to the shear loss modulus (viscous part) [49]. Among many scientists, Martin and Lucklum are the main researchers who dedicate their effort to characterize the viscoelastic medium using a TSM piezoelectric sensor [37, 50] and Thompson has been very well known by his study in slip interfacial condition using a TSM sensor [51].

Though a significant knowledge on the interaction between viscoelastic thin film and piezoelectric sensor (e.g., TSM) has been accumulated over the last decades, there have been not much systematic and comparative studies focused on the quantitative interpretation of measured interfacial phenomena and the signatures of the response of a multiresonance Thickness-Shear Mode (MTSM) sensor. This thesis is targeted to fulfill this gap and provide a comprehensive modeling and experimental foundation which will lead to the development of sensitive, reliable, inexpensive instrumentation for the characterization of a broad range of viscoelastic, especially biological interfacial phenomena.

3 OBJECTIVES

The main objective of the work is to study the MTSM sensor to analyze the variety of interfacial processes. Both theoretical and experimental analyses of MTSM sensors have been examined. These included;

- Analysis, modeling and simulation of MTSM sensor loaded with viscoelastic (VE) mediums
- Experimental study of MTSM sensor under broad range of operating conditions
- Determination and correlation of the acoustic signatures of MTSM sensors with bio-physical characteristics of the medium.
- Application of the MTSM sensor as for monitoring bio thin film formation process.
- Applying MTSM technology for monitoring thin film fabrication processes.

The thesis consists of four major sections: Modeling of an evaporation-induced deposition process, theoretical analysis that includes modeling of the MTSM sensor with VE medium and the simulation of the MTSM sensor, experimental analysis that includes experimentation of MTSM measurement system with biological samples, and discussion.

First, in the modeling of an evaporation process section, an evaporation-induced deposition process is divided and into four stages and described based on the mechanical properties of the medium.

Second, the system with a MTSM sensor and a VE thin layer has been modeled based on the constitutive equations of a TSM sensor and an additional VE layer. Boundary conditions between TSM and VE layer and upper and lower interfaces are also considered to induce the shear mechanical impedance at the TSM surface. Then, the relative changes in resonant frequency and attenuation of the MTSM measurement system are obtained from the above model and saved for comparative studies with later experimental results. Completed derivations of the model are included in Appendix. After the establishment of the system model, the individual effect of the three mechanical properties (density, viscosity, and stiffness) and the geometrical parameter (thickness) to the overall response of MTSM was simulated resulting in 3-dimensional and 2-dimensional graphs which indicated the effect of each of the parameters.

Thirdly, as a verification of the model, the evaporation process of a Newtonian liquid was simulated with only thickness changes (no changes in viscosity or density) and as an application of MTSM technique, the MTSM measurement system has been utilized to study the acoustic signatures of the evaporation-induced deposition process of biological samples (collagen and albumin).

Finally, the discussions of the simulations, and the comparisons between simulation and experimental results are included with an analytical approach at the end of the thesis.

4 MODELING OF AN EVAPORATION-INDUCED DEPOSITION PROCESS

Evaporation-induced deposition process is the process whereby atoms or molecules in a liquid state gain sufficient energy to enter the gaseous state and leaving a thin-film. Especially, during the evaporation-induced deposition process of biological samples, such as, collagen or albumin, there are two major processes involved: evaporation of a solution and deposition of proteins on the surface of the sensor substrate [52, 53]. Figure 5 shows step-by-step typical four-stage evaporation-induced deposition processes of biological thin film on the sensor surface.

Stage I: Initially, collagen monomers or albumin clusters are homogeneously distributed in the solution with uniform mechanical characteristics over the whole volume (stage I in Figure 5 (a)). The movements of monomers or clusters are governed by the Brownian motion due to the nano range size of the solutes in this first stage [54]. In this thesis, the stage I is characterized as a viscous liquid because of the low concentration of the solutes (1 *mg*/*ml*). The elastic modulus of the sample in the stage I is assumed to be zero and the density is also assumed to be same as water like value (1000 kg/m^3) for the simulation [55]. The viscosity of the sample is varied between 0.001 *kg*/*ms* to 0.01 *kg*/*ms* to indicate the water like condition of the sample. Therefore, the main driven parameter in this stage I is the thickness due to the evaporation of the solution while there are slight changes in the viscosity and stiffness and almost no changes in the density of the sample.

Stage II: Next, due to the evaporation of the solvent through the top surface, the concentration of collagen monomers or albumin clusters increases at the surface region of the solution. After reaching the critical concentration, monomers start to aggregate to form larger fibrils or clusters and each cluster also starts to form bigger clusters by an agglomerating process at the surface region. The large fibrils and agglomerated clusters no longer obey the Brownian motion due to their size and mass. Gravity plays a role for the sedimentation of solutes on the surface of the sensor substrate (stage II in Figure 5 (b)) [56]. The stage II is characterized as a soft robber viscoelastic condition. In this stage, both the viscosity and stiffness are increased from the previous stage I. The range of viscosity increased between 0.01 kg/ms and 0.1 kg/ms to describe the higher viscosity of the stage II due to the presence of deposited solutes on the surface of the sensor [55, 57]. However, the range of stiffness also has been maintained same as stage I (between 0 and 10^5 N/m^2) to present a soft rubbery stage of the sample. Therefore, the main driven parameter of the stage II is viscosity according to relatively smaller changes in the thickness and the stiffness of the sample.

Stage III: When most of the aggregated or agglomerated solutes are deposited, the sample forms a gelatin phase film at the bottom of the sensor surface (stage III in Figure 5 (c)) [58]. The stage of the sample is characterized as a hard rubber condition in this thesis. The viscosity of the sample is increased up to 0.1 *kg*/*ms* and the range of the stiffness has been increased from 10^5 to 10^7 N/m^2 to impart the hard rubber condition of the sample than the previous stage II. Therefore, there are two driven parameters (viscosity and stiffness) that characterizing the condition of the sample in this stage III while there are small changes in the density and thickness.

Stage IV: Finally, after all the solution has evaporated, the collagen fibrils and albumin clusters form a thin rigid film on the surface of the sensor (stage IV in Figure 5 (d)) [59]. This stage is characterized as a solid like thin film. There is small changes in the viscosity from the previous stage III (0.1 *kg*/*ms*), but the stiffness has been increased (10^7 ~ 10^8 N/m^2) to indicate the rigidity of the sample condition. Therefore, the main parameter that characterizes the condition of the sample in this stage IV is stiffness while there are relatively small changes in the viscosity and no changes in the thickness and the density.

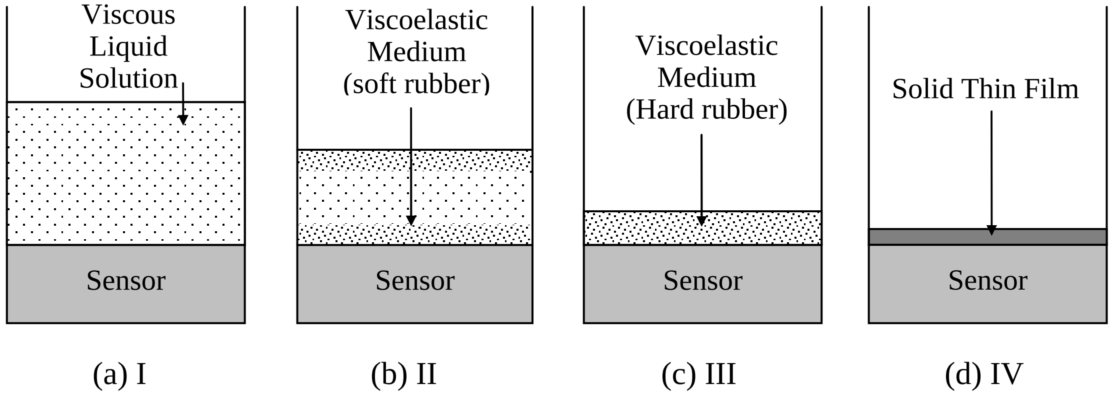

(a) I (b) II (c) III (d) IV

Figure 5. A typical evaporation-induced deposition processes of biological thin film. (a) Stage I, (b) stage II, (c) stage III, and (d) stage IV.

These stages are represented by different viscoelastic properties: stage I (viscous), stage II (viscoelastic: soft rubber), stage III (viscoelastic: hard rubber), and stage IV (rigid). In the next chapter the MTSM modeling for all those different stage is presented.

5 THEORETICAL ANALYSIS OF MTSM

In the previous chapter, the condition of the sample has been divided into four stages: (a) Newtonian viscous liquid, (b) soft rubber like viscoelastic, (c) hard rubber like viscoelastic, and (d) glassy like solid status. Therefore, it is difficult to invoke a simple Sauerbrey [22] or Kanazawa [40] equations to explain the response of MTSM in each condition. Sauerbrey equation might be suitable to explain and simulate the response of MTSM sensors in stage IV in Figure 5 because of the glassy like characteristic (high elastic stiffness ~ 10^8 N/m^2) of the sample, and Kanazawa equation might be appropriate to elucidate the response of MTSM sensor in stage I in Figure 5 because of the Newtonian characteristic (no stiffness or at least smaller than 10^5 N/m^2) of the sample. However, neither equation can not be solely used to describe the stage II or III in Figure 5. When the sample is in viscoelastic (VE) condition, the viscosity and stiffness of the sample play simultaneously to characterize the condition of the sample [60].

Following list shows typical values of the mechanical properties (viscosity (η) and stiffness (μ)) of each stage during the evaporation-induced deposition process of biological samples.

1) Stage **I** - $\eta \neq 0$ and $\mu \approx 0$

   Since the medium is in water like condition, viscosity of the medium is almost same as water (η = 0.001 *kg/ms*) and stiffness can be assumed to be zero. Kanazawa equation is suitable in this case [40, 61].

2) Stage **II** - $\eta \neq 0$ and $\mu \neq 0$

   In this stage, the sample is in soft rubber condition. Viscosity has been slightly increased ($\eta \approx 0.01 \sim 0.1$ *kg/ms*) and stiffness also starts to play role ($\mu \approx 10^5$ N/m^2) [31].

3) Stage **III** - $\eta \neq 0$ and $\mu \neq 0$

   Viscosity and stiffness are increased up to $\eta = 1$ *kg/ms* and $\mu = 10^8 \sim 10^9$ N/m^2 to reveal the hard rubber condition of the sample [57, 62].

4) Stage **IV** - $\eta \neq 0$ and $\mu \neq 0$

   The sample is in a rigid condition in this stage. Viscosity has been decreased slightly ($\eta \approx 0.5$ *kg/ms*) to represent the hardening process of the sample while stiffness stays same at the value of stage **III** [37, 63].

In this chapter, the model of a MTSM sensor with a viscoelastic load is presented based on the existing TSM Sauerbrey and Kanazawa models. The MTSM model has been validated by simulating an evaporation process of a Newtonian liquid (water) and comparing it with the experimental data. The library of the signatures of a MTSM with a viscoelastic medium has been prepared by studying the effect of changes in mechanical and geometrical properties (viscosity, stiffness, density, and thickness) on the MTSM sensor response. Finally, the simulations of a MTSM sensor for an evaporation-induced deposition process of biological samples (collagen and albumin) have been presented.

5.1 Modeling of a MTSM sensor with a viscoelastic load

One important feature of the MTSM sensor is its capability of being excited at higher harmonics. As higher harmonics are applied, the information (changes in the resonant frequency and attenuation) from the MTSM sensor represents the information (mechanical properties) of the different distance from the sensor surface due to the different penetration depth of the acoustic wave through the medium. In other words, the medium can be sliced in a multilayered thin film by applying higher harmonic frequencies. Figure 6 shows the principles of this concept. For example, if the medium has different mechanical properties through the thickness, then it can be observed by analyzing the different responses of the MTSM sensor at each harmonics.

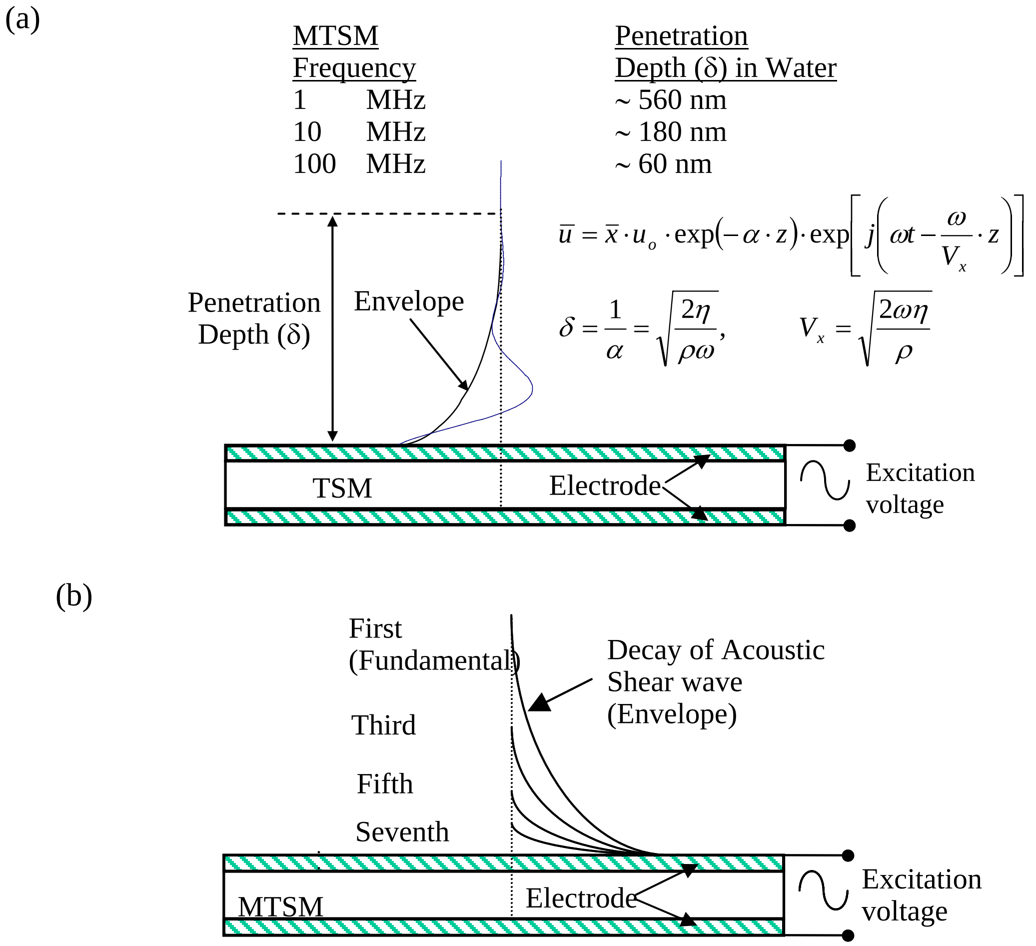

Figure 6. A conceptual model of the MTSM sensor, (a) a sensor operating at the fundamental frequency mode, (b) a sensor operating at the fundamental frequency and at higher harmonics.

A simplified model of the system was developed to study and analyze the shift in resonant frequency, Δf, as a function of changes in thickness, density, viscosity and elastic stiffness during the deposition process of the sample. The well known Maxwell model (two elements of a spring and a dashpot in series) was invoked to describe and model the shear modulus and the deposition process of a biological sample [64]. New effective complex elastic stiffness, μ_{eff}, which contains an elastic term and a viscosity term, was calculated for the viscoelastic characteristics of the sample. Figure 7 shows two layered structure of a MTSM sensor and a viscoelastic sample with boundary condition at the interface. Subscripts f and q represent the viscoelastic medium and quartz TSM sensor.

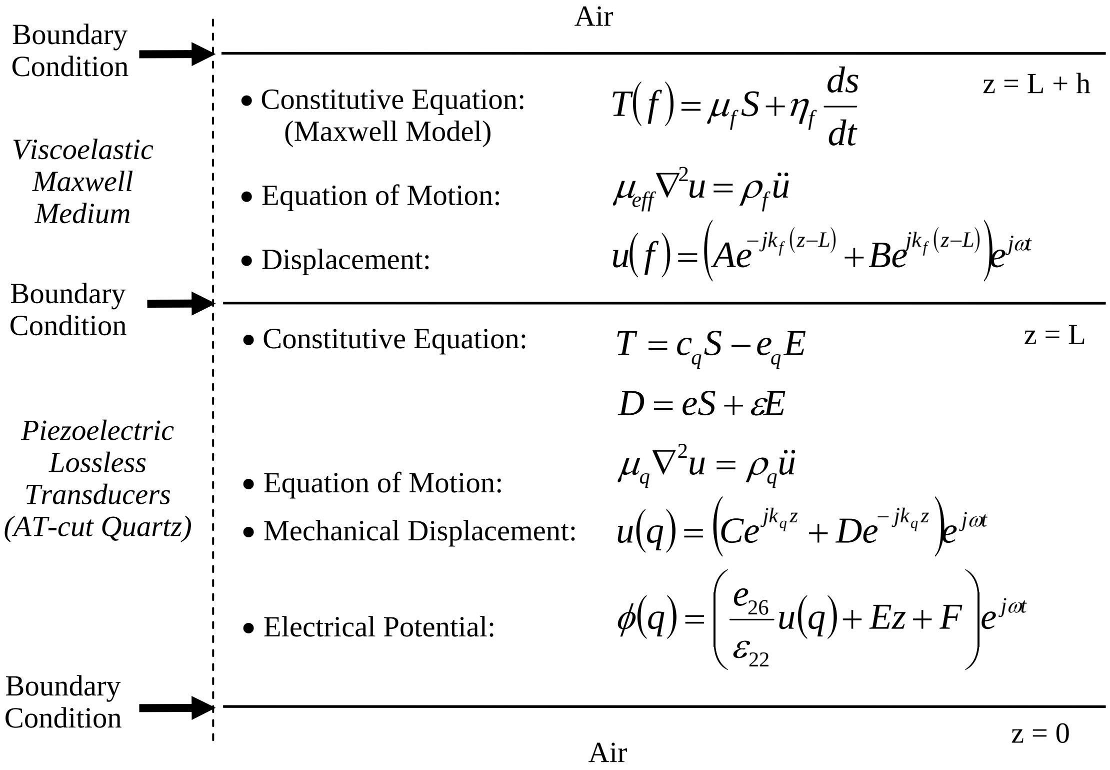

Figure 7. Two layered structure of the MTSM sensor with viscoelastic sample on the surface.

First, the constitutive equation of the VE film is,

$$T_f=\mu_f S+\eta_f\frac{dS}{dt}=\mu_f\left(\frac{du_f}{dz}\right)+\eta_f\frac{dv_f}{dz}$$

$$=\left(\mu_f+j\omega\eta_f\right)\frac{du_f}{dz} \quad \text{...}(1)$$

If we assume $\mu_{eff}=\mu_f+j\omega\eta_f$, then equation (1) becomes

$$T_f = \mu_{eff} \cdot \frac{du_f}{dz} \quad \ldots\ldots\ldots\ldots\ldots\ldots\ldots\ldots\ldots\ldots\ldots\ldots\ldots\ldots\ldots\ldots\ldots\ldots\ldots\ldots\ldots\ldots\text{(1a)}$$

where T_f, μ_f, S, η_f, u_f, v_f, and ω stand for shear stress in film, elastic stiffness, strain, viscosity, displacement, shear particle velocity, and angular frequency. With the boundary conditions (at $z = 0$, $z = L$, and $z = L + h$) at the interfaces between VE film and MTSM, one can obtain [Details available in the Appendix],

$$Z_f = \frac{T_f}{v_f} = j\left(\mu_{eff} \cdot \rho_f\right)^{1/2} \cdot \tan\left(k_f h\right) \quad \ldots\ldots\ldots\ldots\ldots\ldots\ldots\ldots\ldots\ldots\ldots\ldots\ldots\ldots\ldots\ldots\ldots\text{(2)}$$

$$Z_e = \frac{N\pi}{4K^2\omega_s C_0} \cdot Z_f = j\omega L_N + R_N \quad \ldots\ldots\ldots\ldots\ldots\ldots\ldots\ldots\ldots\ldots\ldots\ldots\ldots\ldots\ldots\text{(3)}$$

where

$$R_2 = \frac{N\pi}{4K^2\omega C_0} \cdot \frac{\mathrm{Re}[Z_f]}{\left(\rho_f \mu_f\right)^{1/2}} \quad \ldots\ldots\ldots\ldots\ldots\ldots\ldots\ldots\ldots\ldots\ldots\ldots\ldots\ldots\ldots\ldots\ldots\ldots\text{(3a)}$$

$$L_2 = \frac{N\pi}{4K^2\omega^2 C_0} \cdot \frac{\mathrm{Im}[Z_f]}{\left(\rho_f \mu_f\right)^{1/2}} \quad \ldots\ldots\ldots\ldots\ldots\ldots\ldots\ldots\ldots\ldots\ldots\ldots\ldots\ldots\ldots\ldots\ldots\text{(3b)}$$

$$v_f = \left(\frac{\mu_{eff}}{\rho_f}\right)^{1/2} = \left(\frac{\mu_f + j\omega\eta_f}{\rho_f}\right)^{1/2} \quad \ldots\ldots\ldots\ldots\ldots\ldots\ldots\ldots\ldots\ldots\ldots\ldots\ldots\ldots\ldots\text{(3c)}$$

Z_f, v_f, N, and ρ_f in equation (2) indicate that the mechanical impedance, surface shear particle velocity, harmonic number, and the bulk density of the VE film. Graphs (a) and

(b) in Figure 8 shows the lumped model of TSM and MTSM sensor at its near resonant frequency. Z_e, K^2, ω_s, and C_0 in equation (3) indicate the electrical motional impedance, electromechanical coupling factor for a MTSM, resonant angular frequency, and static capacitance of MTSM. R_2 and L_2 are the additional resistance components related to the damping and the resonant frequency of the VE film-loaded MTSM sensors in Figure 7 [41]. Therefore, attenuation (α) can be calculated from the typical Martin *et. al.*, approach.

$$\alpha = S_{21} = 20 \cdot \log_{10}\left(\left|\frac{100}{100 + Z_t}\right|\right) \quad \text{……………………………………………(3d)}$$

where $Z_t = \frac{Z_s Z_0}{Z_s + Z_0}$, $Z_s = R_N + j\omega L_N + \frac{1}{j\omega C_N} + Z_e$, and $Z_0 = \frac{1}{j\omega C_0}$.

Also, since multiharmonic operation is applied, the basic elements of the circuit have to be modified while C_0 is same as others [22]:

$$C_0 = \frac{\varepsilon_{22} A}{h_s}, \quad \text{…………………………………………….………(3e)}$$

$$C_N = \frac{8K^2 C_0}{(N\pi)^2}, \quad \text{…………………….…………………………………(3f)}$$

$$L_N = \frac{1}{\omega_s^2 C_N}, \quad \text{……………………………………………………..(3g)}$$

$$R_N = \frac{\eta_q}{\mu_q C_N} \qquad \dots\dots\dots\dots\dots\dots\dots\dots\dots\dots\dots\dots\dots\dots\dots\dots\dots\dots\dots\text{(3h)}$$

Where A and h_s are area of the electrode and the thickness; ε_{22}, μ_q, and η_q are dielectric permittivity, shear stiffness and effective viscosity of the MTSM sensor, respectively. Z_t indicates the total electrical impedance of the MTSM. S_{21} means the forward transmission parameter. The above equation can be rewritten as follows;

$$\alpha = S_{21} = 20 \cdot \log_{10}\left(\frac{100}{100 + \left| \frac{\left(R_N + j\omega L_N + \frac{1}{j\omega C_N} + \left(\frac{N\pi}{4K^2 \omega_s C_0} \cdot \left(j\left(\mu_{eff} \cdot \rho_f \right)^{1/2} \cdot \tan\left(k_f h \right) \right) \right) \right) \left(\frac{1}{j\omega C_0} \right)}{\left(R_N + j\omega L_N + \frac{1}{j\omega C_N} + \left(\frac{N\pi}{4K^2 \omega_s C_0} \cdot \left(j\left(\mu_{eff} \cdot \rho_f \right)^{1/2} \cdot \tan\left(k_f h \right) \right) \right) \right) + \left(\frac{1}{j\omega C_0} \right)} \right|} \right) \quad \ldots\ldots\ldots\ldots\ldots\ldots\ldots\ldots\ldots\ldots..(4)$$

Since,

$$k_f = \frac{\omega}{v_f} = \mathrm{Re}[k_f] + \mathrm{Im}[k_f] = k + j\beta \,,$$

while, $$k = \mathrm{Re}[k_f] = \omega \left(\frac{\rho_f^2}{\mu_f^2 + \left(\omega \eta_f \right)^2} \right)^{1/4} \cos\left(-\frac{1}{2} \tan^{-1}\left(\frac{\omega \eta_f}{\mu_f} \right) \right) \quad \ldots\ldots\ldots\ldots\ldots\ldots\ldots\ldots\ldots\ldots\ldots\ldots\ldots\ldots(4a)$$

$$\beta = \mathrm{Im}[k_f] = \omega \left(\frac{\rho_f^2}{\mu_f^2 + \left(\omega \eta_f \right)^2} \right)^{1/4} \sin\left(-\frac{1}{2} \tan^{-1}\left(\frac{\omega \eta_f}{\mu_f} \right) \right) \quad \ldots\ldots\ldots\ldots\ldots\ldots\ldots\ldots\ldots\ldots\ldots\ldots....(4b)$$

where, k is the real part and β is the imaginary part of the wave vector and v_f is the particle velocity in VE film. Also with the boundary conditions (at $z = 0$, $z = L$, and $z = L + h$) at the interfaces between VE film and MTSM, the equation (5) can be obtained. The relative change in resonant frequency ($\Delta f/f_{0N}$) is the real part of this equation (5),

$$\therefore \frac{\Delta f}{f_{0N}} = \mathrm{Re}\left[\frac{1}{N\pi}\cdot\tan^{-1}\left(\frac{-k_f\left(\mu_f + j\omega\eta_f\right)\tan\left(k_f h\right)}{\mu_q k_q}\right)\right] \quad \ldots\ldots\ldots\ldots\ldots\ldots\ldots\ldots..(5)$$

where f_{0N}, Δf, h, and k_q are the resonant frequency of MTSM in hertz, shift in the resonant frequency, thickness of the film, and the wave vector of the MTSM. Also Re[ ] refers to the real part of a complex number in the equation (5).

In the case with elastic thin films (when $\eta_f = 0$), the equation (5) becomes

$$\Delta f = -\frac{2 f_0^2 \rho_f h}{N\left(\mu_q \rho_q\right)^{1/2}} \quad \ldots\ldots\ldots\ldots\ldots\ldots\ldots\ldots\ldots\ldots\ldots\ldots\ldots\ldots\ldots\ldots\ldots\ldots..\ldots(5a)$$

which is same as Sauerbrey equation. For Newtonian liquid loading (when $\mu_f = 0$ and $h \rightarrow \infty$), the equation (5) now becomes

$$\Delta f = -\frac{f_0^{3/2}}{N}\left(\frac{\rho_f \eta_f}{\pi \rho_q \mu_q}\right)^{1/2} \qquad \text{……………………………………………………..(5b)}$$

which is same as Kanazawa equation [40].

Graphs (c), (d), (e), and (f) are the simulation of the MTSM sensor in each stage. Graph (c) indicates the MTSM sensor response of stage I (viscous medium) with the parameter of DI water as a function of frequency while the other graphs (d), (e), and (f) shows the MTSM sensor response to VE medium (soft rubber), VE medium (hard rubber), and thin rigid film, respectively. As the medium becomes more viscous and rigid (from stage I to stage III), the dynamic range of resonant behavior of the MTSM sensor decrease due to the VE loading on the surface of the MTSM sensor. However, at the final stage IV, the dynamic range of the MTSM sensor become greater than the previous stage because of the dominant contribution of the high elastic modulus of the medium.

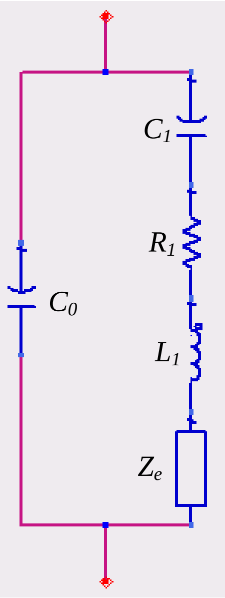

C_1
R_1
C_0
L_1
Z_e

(a)

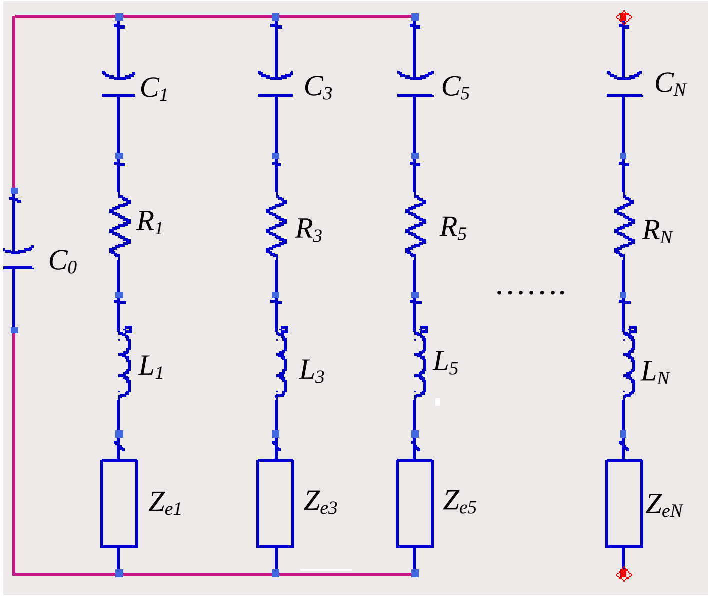

C_1
C_3
C_5
C_N
R_1
R_3
R_5
R_N
C_0
…….
L_1
L_3
L_5
L_N
Z_{e1}
Z_{e3}
Z_{e5}
Z_{eN}

(b)

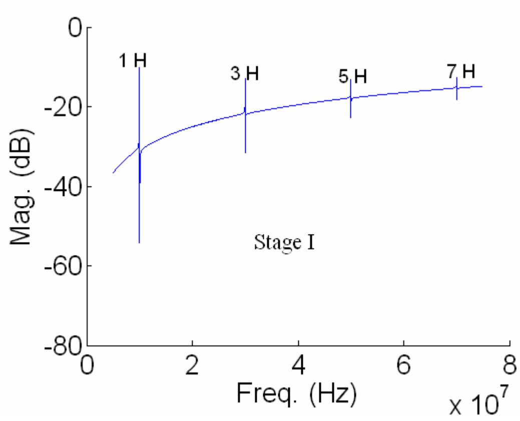

Mag. (dB)
0
-20
-40
-60
-80
1 H
3 H
5 H
7 H
Stage I
0
2
4
6
8
Freq. (Hz)
x 10^7

(c)

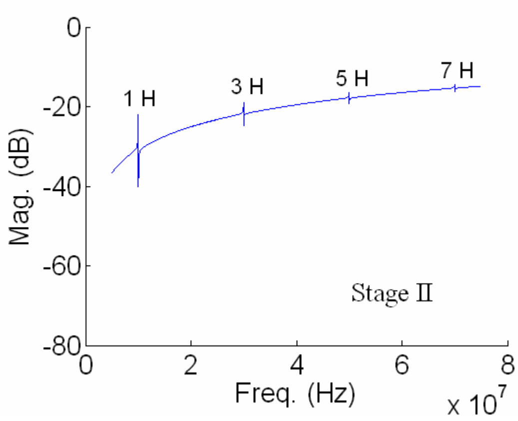

Mag. (dB)
0
-20
-40
-60
-80
1 H
3 H
5 H
7 H
Stage II
0
2
4
6
8
Freq. (Hz)
x 10^7

(d)

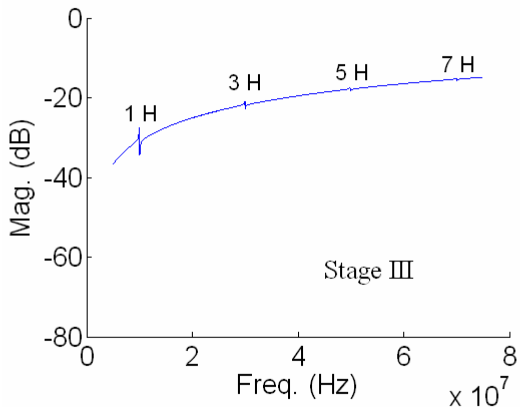

Mag. (dB)
0
-20
-40
-60
-80
1 H
3 H
5 H
7 H
Stage III
0
2
4
6
8
Freq. (Hz)
x 10^7

(e)

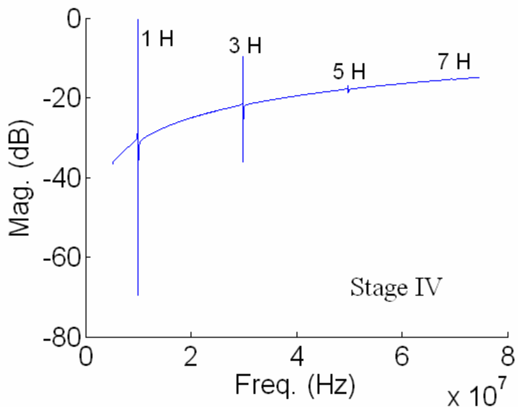

Mag. (dB)
0
-20
-40
-60
-80
1 H
3 H
5 H
7 H
Stage IV
0
2
4
6
8
Freq. (Hz)
x 10^7

(f)

Figure 8**.** Equivalent circuit models to describe the near resonant electrical characteristics of the MTSM resonator with VE film coatings. (a) The equivalent circuit of TSM sensor with a complex impedance element Z_e, and (b) The equivalent circuit of MTSM sensor with complex impedance elements. C_1, R_1, L_1, and Z_{e1} indicate 1st harmonic equivalent components while C_3, R_3, L_3, Z_{e3}, and C_5, R_5, L_5, Z_{e5} indicate 3rd and 5th harmonic equivalent components respectively. Graphs (c), (d), (e), and (f) are simulation of the equation (4) with the parameters for each stage as a function of frequency.

5.2 Definition of parameters characterizing MTSM sensors response

A TSM sensor was first demonstrated as an organic vapor sensors by King in 1964 [65] and later reviewed by other authors for measurement of airborne and dissolved species [66]. TSM sensors are operated by monitoring interfacial mass/density, viscosity, or elasticity changes taking place during chemical or biological processes and it can be monitored by observing the changes in resonant frequency ($\Delta f = f_r - f'_r$ in Figure 9) and attenuation ($\Delta\alpha = \alpha_r - \alpha'_r$ in Figure 9). Figure 9 shows the typical frequency response of a TSM sensor to viscoelastic loading on it.

The response of MTSM sensor is shown by the changes in the resonant frequency (Δf), attenuation ($\Delta\alpha$), and phase ($\Delta\phi$). Figure 10 and 11 show frequency responses and signatures of MTSM sensor to two different stages during the evaporation-induced deposition process of biological samples. Graph (a) in Figure 10 shows the changes in the frequency response of MTSM sensor caused by the increase in the viscosity of shear modulus of the medium. The increase of viscosity is represented by the decrease in the resonant frequency and increase in the attenuation (see graphs (a) and (c) in Figure 11). Graph (b) in Figure 10 shows the changes in the frequency response of MTSM sensor caused by the increase in the stiffness of shear modulus of the medium. Also the increase of stiffness affects the resonant frequency to be increased and the attenuation to be decreased (see graphs (b) and (d) in Figure 11). Based on the knowledge that the use of the higher harmonic resonant frequencies of the MTSM sensor means that the different penetration depth of acoustic shear waves from the surface of the MTSM sensor (see Figure 6), the measurand can be virtually sliced and its mechanical properties at nanometers range above the surface of the MTSM sensor can be acquired [67].

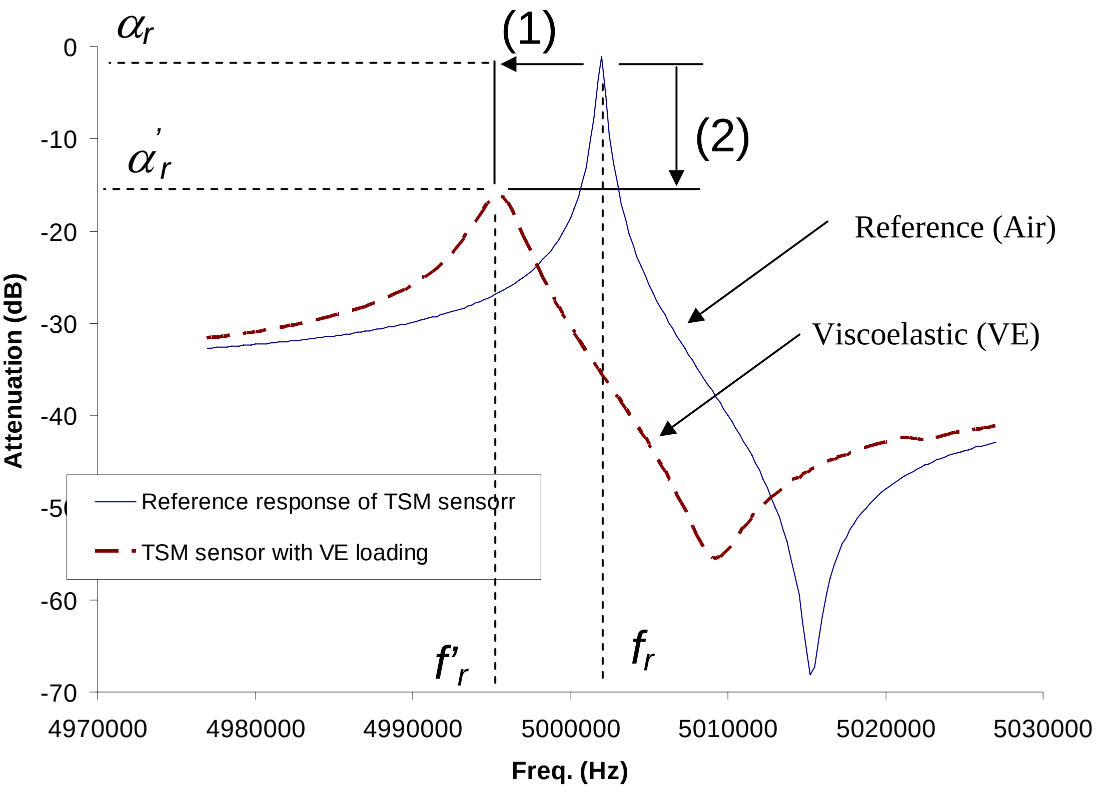

Figure 9. A typical frequency responses (S_{21}) of TSM sensor to viscoelastic loading.

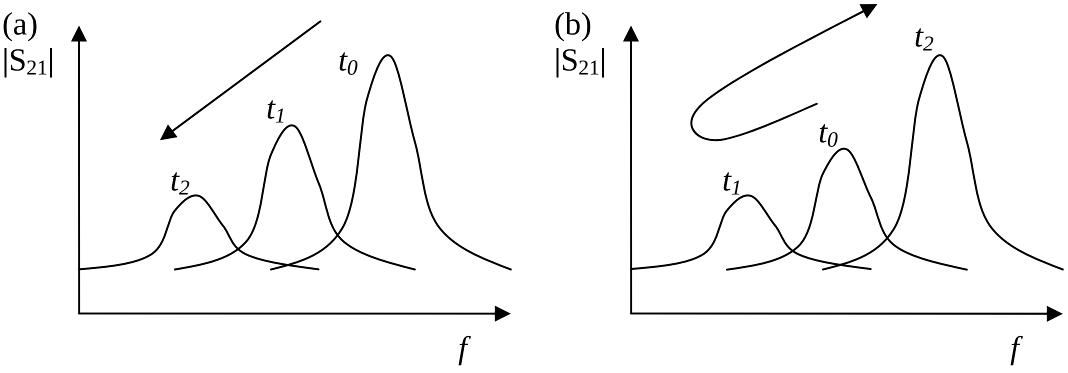

Figure 10. A frequency responses (S_{21}) of MTSM sensor to viscoelastic (VE) loading. Graph (a) represents the Stage II and (b) represents the stage III and IV in Figure 5.

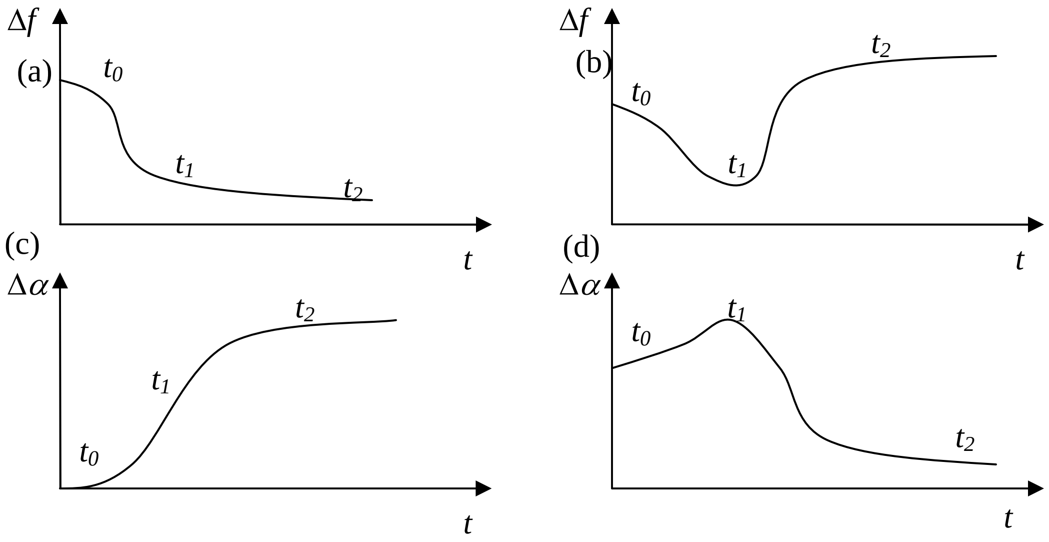

Figure 11. Two different signatures of MTSM sensor to VE medium. (a) and (c) are the relative Δf and α signatures of the case (a) in Figure 10, and (b) and (d) are the relative Δf and α signatures of the case (b) in Figure 10. ($t_0 < t_1 < t_2$)

5.3 Validation of theoretical approach: simulation and experiment of a MTSM for an evaporation process of a Newtonian liquid

As a first step, an evaporation process of a Newtonian liquid has been analyzed by the MTSM sensor technology. Equation (4) provides the attenuation at the resonant frequency of each harmonic and equation (5) shows the relative changes in the resonant frequency shift at each harmonic when the MTSM sensor is loaded with a layer of Newtonian liquid on one side of the sensor. A Newtonian liquid does not change its mechanical properties, such as density and viscosity, during the evaporation process. There is only a thickness change involved during the evaporation process. Therefore, the viscosity and density of the medium were set to be a constant for the simulation. The results of the simulation are showing in graphs of Figure 12, and Table 1 shows the information about the variables of the simulations in Figure 12. The gray arrows in graphs are indicating the direction of the evaporation process.

The depth of penetration of acoustic shear waves in the medium can be obtained from the reciprocal of the imaginary part (β) of wave number equation (4b),

$$\delta = \frac{1}{\mathrm{Im}\left[k_f\right]} = \frac{1}{\omega\left(\dfrac{\rho_f^2}{\mu_f^2 + \left(\omega\eta_f\right)^2}\right)^{1/4} \sin\left(-\dfrac{1}{2}\tan^{-1}\left(\dfrac{\omega\eta_f}{\mu_f}\right)\right)} \quad \text{............................(6)}$$

where, k_f, ρ_f, μ_f, η_f, and ω indicate the wave number, density, stiffness, viscosity of the medium, and resonant angular frequency. For the Newtonian liquid case, the above equation becomes simpler by setting the stiffness equal to zero ($\mu_f = 0$) [22].

$$\delta = \left(\frac{2\eta_f}{\omega\rho_f}\right)^{1/2} \quad \text{................Penetration depth of a Newtonian liquid.}$$

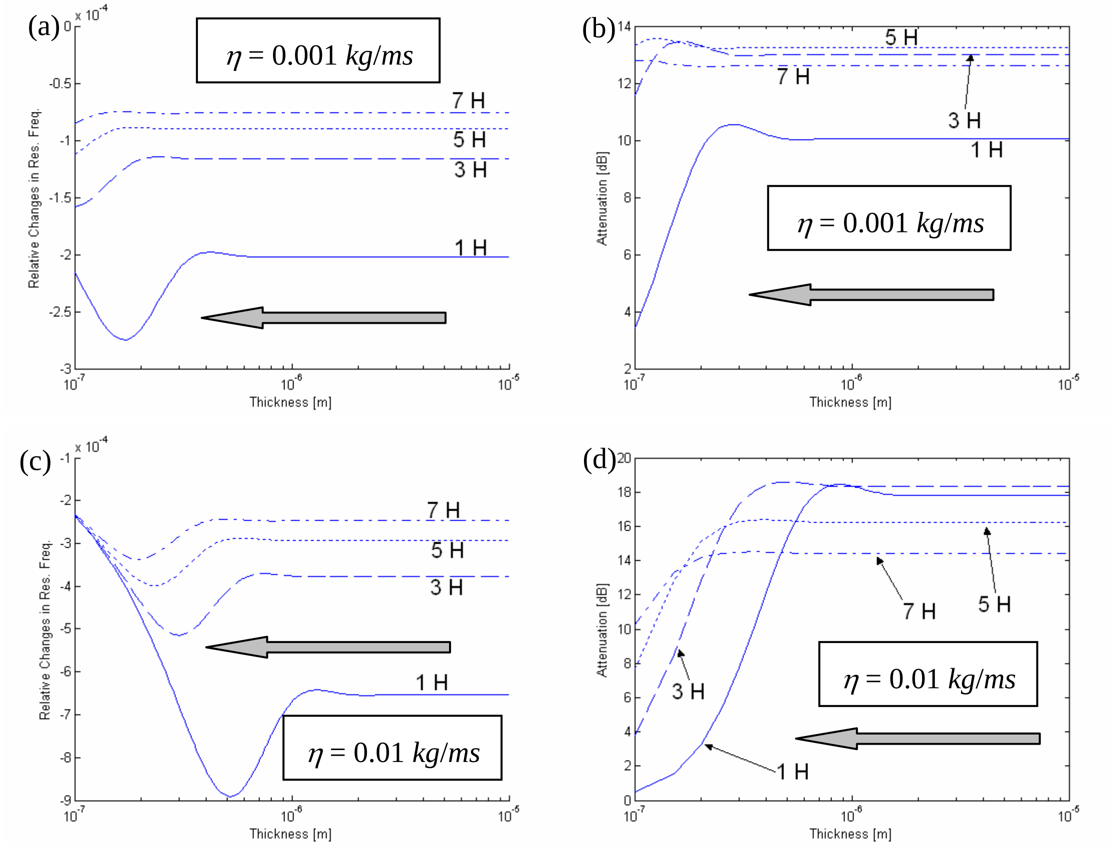

Figure 12. Simulations of an evaporation process of a Newtonian liquid with different viscosity. Gray arrow in each graph indicates the direction of a typical evaporation process. (a) and (b) are the relative Δf and α of MTSM with a water ($\eta = 10^{-3}$ *kg/ms*, $\mu = 0$, and $\rho = 1000$ *kg/m*^{3}) loading, and (c) and (d) are the relative Δf and α of MTSM with a liquid that has 10 time higher viscosity than water ($\eta = 10^{-2}$ *kg/ms*, $\mu = 0$, and $\rho = 1050$ *kg/m*^{3}).

Table 1 shows the penetration depth of acoustic shear waves when the MTSM is loaded with a Newtonian liquid. Since the penetration depth is proportional to the square root of the viscosity, the penetration depths of each harmonic of the liquid that has 10 times higher viscosity than water are always greater than the one in water. The penetration depth of acoustic shear waves at the fundamental frequency is greatest while the one of 7th harmonic frequency is smallest because the penetration depth is also reciprocally proportional to the square root of the frequency.

Table 1. Penetration depths (δ) of the harmonic acoustic shear waves of fundamental frequency at 10 *MHz* in a Newtonian liquid [22].

Harmonic No. (frequency)	Penetration depth (δ) in water	Penetration depth (δ) in liquid that has 10 times higher viscosity than water
1st H (~ 10 MHz)	≈ 180 *nm*	≈ 560 *nm*
3rd H (~ 30 MHz)	≈ 100 *nm*	≈ 320 *nm*
5th H (~ 50 MHz)	≈ 80 *nm*	≈ 250 *nm*
7th H (~ 70 MHz)	≈ 70 *nm*	≈ 210 *nm*

Both relative Δf and α shows stabilized responses regardless of the changes in the thickness (h) until it approaches to a couple of penetration depths (δ) in each harmonic in Figure 12. When $\delta < h < 2\delta$, there are oscillatory responses, and as the thickness becomes smaller than δ, a typical mass loading effect and Kanazawa viscous effect are shown in both relative Δf and α with different magnitudes at each harmonic. Obviously, in most of the cases, the dynamic range of the first harmonic response of both relative Δf and α are largest among other harmonics because of the sensitivity.

Graphs (c) and (d) in Figure 12 show the relative Δf and α of the MTSM sensor response with a liquid that has 10 times higher viscosity than the water (viscosity ~ 0.01 *kg/ms*). Due to the increase in the viscosity, the penetration depth is also increased and it influences the oscillatory responses of relative Δf and α to be appearing with larger magnitudes. In addition, the oscillatory responses start when the film is thicker than the case with lower viscosity, such as water case (viscosity ~ 0.001 *kg/ms*).

The comparison study between theoretical and experimental results are shown in chapter 6, section 6.2. In section 6.2., the simulation has been obtained based on the mechanical properties of deionized (DI) water. Also the MTSM measurement system has been set up to monitor the evaporation process of DI water. Both simulation and experimental results show similar behavior of MTSM sensor to the evaporation process of DI water except some discrepancy in the duration of stage III due to the physical difference of water layer. Detailed explanation of this discrepancy is provided in section 6.2.

5.4 Library of the signature of a MTSM sensor with a viscoelastic medium

In this section, the simulations of the relative changes in the resonant frequency in harmonics (relative Δf) and attenuation (α) using equation (4) and (5) are analyzed as a 'Library of the signature' of a MTSM sensor with variety of ambient loading conditions. The three mechanical properties (density, viscosity, and stiffness) and a geometrical property (thickness) are considered as main parameters that affect the overall response of the MTSM sensors. Individual stages of Figure 5 are considered as effect of changes in mechanical or geometrical parameters by generating either line graphs to study the effect from one parameter or surface mesh graphs to monitor the effect from two parameters. In addition, the different paths on the surface mesh graphs are investigated to identify the contribution of each parameter to the overall response of MTSM sensors.

5.4.1 Effect of changes in thickness on the MTSM response: stage I

In this section, the stage **I** of the evaporation-induced deposition process of biological films has been simulated by only varying the thickness. The starting condition of the sample in stage **I** is in liquid phase. Because of the low concentration of the solutes in a solution (1 *mg/ml*), the sample was treated as a Newtonian liquid. The stiffness was equal to zero to reveal the characteristic of a Newtonian liquid and density was also equal to 1000 kg/m^3 to represent the water like sample condition during the simulation of stage **I**. Due to the evaporation process of the solvent through the liquid surface the thickness of the sample changes. Therefore, only the thickness of the sample was varied from 1 *mm* down to 100 *nm* for the simulations. Graphs in Figure 13 show the simulation of stage **I** of the MTSM sensor of harmonic responses for liquid with different viscosity. Gray arrows in each graph show the direction of changes in the thickness decreasing during the evaporation process. Graphs (a) and (b) show the response of the MTSM sensor when the viscosity of the VE load is same as water at 0.001 *kg/ms*. These graphs show the very beginning status of the stage **I**. As the evaporation of the solvent is continuous, the concentration of the solute starts to increase and the increment of solute affects the viscosity of the solution to rise. Graphs (c) and (d), and (e) and (f) in Figure 13 show the response of MTSM sensor with the higher viscosity, 0.01 and 0.1 *kg/ms*. Table 2 summarizes each simulation in Figure 13 and Table 3 shows the penetration depth (δ) of acoustic shear waves in each simulation.

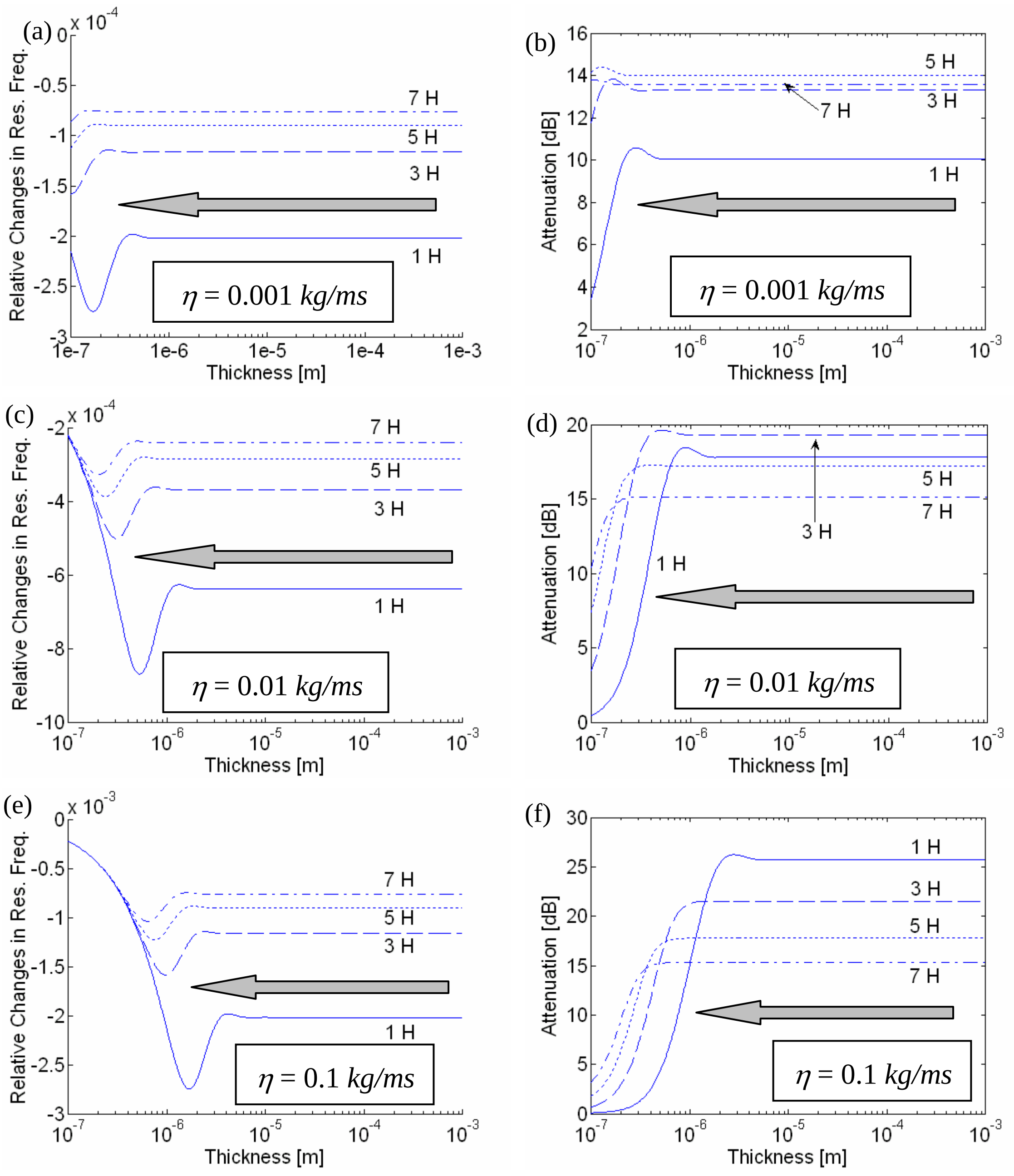

Figure 13. Effect of the changes in thickness to MTSM response: Stage **I** (relative changes in resonant frequency and absolute values of attenuation in dB). Gray arrow in each graph indicates the direction of the evaporation-induced deposition process.

All the graphs in Figure 13 show the same trend. First, it starts with stabilized response when the thickness is much larger than the penetration depth. Second, as the thickness of the VE film reaches close to couple of penetration depth, the response of MTSM sensor starts to oscillate in both relative changes in resonant frequency (relative Δf) and attenuation (α). Finally, when the thickness of the VE film becomes smaller than the penetration depth, it shows the both *Sauerbrey mass effect* and *Kanazawa viscous effect*: decrease in both relative Δf and α, as the thickness becomes smaller.

Table 2. Mechanical properties of VE films of each simulation in Figure 13.

(a) & (b)	Harmonic Relative Δf & Attenuation of Newtonian liquid	$\rho = 1000\ kg/m^3$, $\boldsymbol{\eta = 0.001\ kg/ms}$, $\mu = 0$, and h = variable
(c) & (d)	Harmonic Relative Δf & Attenuation of Newtonian liquid	$\rho = 1000\ kg/m^3$, $\boldsymbol{\eta = 0.01\ kg/ms}$, $\mu = 0$, and h = variable
(e) & (f)	Harmonic Relative Δf & Attenuation of Newtonian liquid	$\rho = 1000\ kg/m^3$, $\boldsymbol{\eta = 0.1\ kg/ms}$, $\mu = 0$, and h = variable

Table 3. Penetration depths, δ, of the acoustic shear waves of 10 *MHz* frequency in Newtonian liquid with various viscosities [22].

	δ, when η = 0.001 *kg/ms* (water)	δ, when η = 0.01 *kg/ms*	δ, when η = 0.1 *kg/ms* (Glycerol)
1 H	≈ 180 *nm*	≈ 560 *nm*	≈ 1.8 *μm*
3 H	≈ 100 *nm*	≈ 320 *nm*	≈ 1.0 *μm*
5 H	≈ 80 *nm*	≈ 250 *nm*	≈ 800 *nm*
7 H	≈ 70 *nm*	≈ 210 *nm*	≈ 670 *nm*

Since the penetration depth is proportional to the square root of the viscosity of the liquid (equation of penetration depth (δ) in page 33), the oscillatory response of more viscous case occurs when the thickness of it larger than the less viscous case. This phenomenon can be found in the simulation of both relative Δf and α. For the changes in the relative Δf (graphs (a), (c), and (e) in Figure13), as the harmonic increases the oscillatory response initiate at lower thickness due to the smaller penetration depth at the higher harmonics. Also the magnitude of oscillatory response of MTSM is decreasing as the harmonic is increasing indicating less sensitivity at higher harmonics. The mechanical properties of the medium can be analyzed by checking the ratio between the responses of each harmonic. The medium with non-uniform distribution of mechanical properties will show different ratio between the responses of each harmonic. In addition, when the thickness is much smaller than the penetration depth ($\delta << h$, when $h < 100$ *nm* in graphs (c) and when $h < 400$ *nm* in graph (e) of Figure 13), it is hard to differentiate the response of MTSM in each harmonics. This indicates that there is a limitation of using Δf analysis when the medium is much smaller than the penetration depth.

Since the penetration depth of more viscous medium is larger than less viscous medium, the oscillatory response of MTSM of more viscous medium occurs when the thickness are greater than less viscous medium and the magnitude of the oscillatory response of more viscous medium is larger than less viscous medium. The differences in the response of MTSM to different viscous medium can be implemented as the signature of medium with changes in the viscosity.

The changes in attenuation show similar response with the changes in the relative Δf. There is a stabilized response when the thickness is much larger than the penetration depth and the oscillatory response occurs when the thickness approaches a couple of penetration depth followed by the decrease of attenuation when the thickness is much smaller than the penetration depth revealing the both *Sauerbrey mass effect* and *Kanazawa viscous effect*. The magnitudes of more viscous medium are greater than less viscous medium indicating more acoustic energy being dissipated by more viscous medium.

5.4.2 Effect of changes in viscosity and thickness on the MTSM response: stage II

In this section, the effect of the changes in viscosity and thickness of VE medium to the response of MTSM is discussed. Due to the layer of sedimentary agglomerated solutes from the super-concentrated condition near the sensor surface during the stage **II**, the viscosity of the sample at the surface of the MTSM sensor changes dramatically during the stage **II** [68, 69]. Simulations of the response of the MTSM sensor to changes in viscosity and thickness of VE thin film are shown in Figure 14. The thickness (h) was varied from 10 μm to 100 nm to show the sensitive response of MTSM near the penetration depth. The viscosity (η) of the film was varied from 0.001 kg/ms to 0.1 kg/ms to cover the condition of the medium from water like liquid to soft rubber in the stage **II.** The elastic stiffness (μ) of the film was assumed to be 10^5 N/m^2 that is higher than the stage I but still not enough to be a gel phase. The density (ρ) was fixed at 1000 kg/m^3 again due to the small range of the variation in density between a water like liquid and a crystallized polymer sample [55]. Table 4 shows the mechanical values of each variable during the simulations. Initially the VE medium shows the water like VE characteristic with viscosity varying between 10^{-3} to 10^{-2} kg/ms and low stiffness (10^5 N/m^2). This stiffness classifies the condition of the medium as a VE medium and also affects the increase in the penetration depth in the medium than the pure Newtonian case due to the energy stored by the stiffness of the medium (Figure 15). The viscosity of the medium has been increased up to 10^{-1} kg/ms to simulate the soft rubbery condition of the medium.

Table 4. Mechanical properties of the variables in the simulation of stage **II**.

	η (kg/ms)	h (m)	ρ (kg/m^3)	μ (N/m^2)
Liquid like (initial stage)	10^{-3}~10^{-2}	10^{-5}~10^{-7}	1000	10^5
Soft rubber (final stage)	10^{-2}~10^{-1}	10^{-5}~10^{-7}	1000	10^5

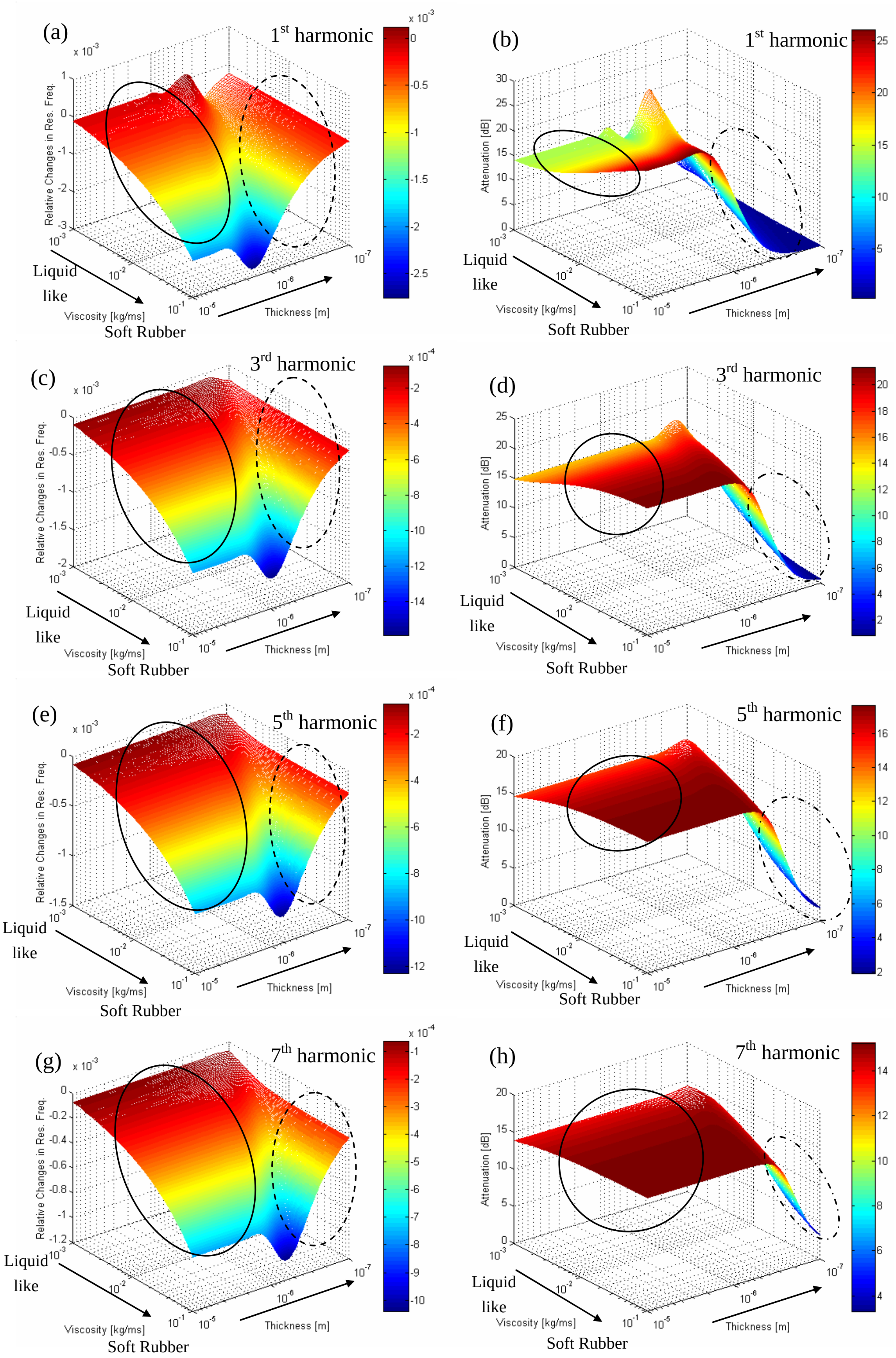
(a)
1st harmonic
x 10-3
Relative Changes in Res. Freq.
1
0
-1
-2
-3
x 10-3
0
-0.5
-1
-1.5
-2
-2.5
Liquid like
Viscosity [kg/ms]
10-3
10-2
10-1
Soft Rubber
10-5
10-6
10-7
Thickness [m]
(b)
1st harmonic
Attenuation [dB]
30
25
20
15
10
5
0
Liquid like
Viscosity [kg/ms]
Soft Rubber
Thickness [m]
(c)
3rd harmonic
x 10-3
0
-0.5
-1
-1.5
-2
x 10-4
-2
-4
-6
-8
-10
-12
-14
(d)
3rd harmonic
25
20
18
16
14
12
10
8
6
4
2
(e)
5th harmonic
x 10-3
0
-0.5
-1
-1.5
x 10-4
-2
-4
-6
-8
-10
-12
(f)
5th harmonic
16
14
12
10
8
6
4
2
(g)
7th harmonic
x 10-3
0
-0.2
-0.4
-0.6
-0.8
-1
-1.2
x 10-4
-1
-2
-3
-4
-5
-6
-7
-8
-9
-10
(h)
7th harmonic
20
15
10
5
0
14
12
10
8
6
4

Figure 14. Effect of the changes in viscosity and thickness to the MTSM response (relative changes in the resonant frequency and absolute values of the attenuation in dB). Arrows in each graph indicate the direction of the evaporation-induced deposition process. (Solid line circle: stabilized response of MTSM through the thickness changes, and dotted line circle: *Sauerbrey Mass effect* region).

In Figure 14 one can notice that the changes in the thickness of the VE medium does not affect the relative changes of Δf and α until the thickness is smaller than a few penetration depths in each harmonic (solid line circled area in the graphs in Figure 14). In other words, the response of the MTSM sensor (changes in relative Δf and α) reaches its stabilized response. In this region there is no effect from the changes in the thickness to the response of MTSM. However, as the medium thickness reaches close to a few penetration depths, the responses of MTSM in both relative Δf and α start to show oscillations due to the reflections of the shear acoustic waves at the top of the VE medium. Lucklum *et. al.* also reported this phenomenon as a oscillatory response [57]. As the medium becomes more viscous ($10^{-2} \leq \eta \leq 10^{-1}$ *kg/ms*), the penetration depth is also increasing and the oscillations become less oscillatory and eventually disappear at high viscosity (~ 0.1 *kg/ms*). In addition, as the thickness becomes close to the penetration depth it goes to its maximum and then gradually decreases by showing *Sauerbrey Mass effect* and *Kanazawa viscous effect* (as thickness becomes smaller than the depth of penetration the response also decreases due to less mass loadings: dashed line circles) in both relative Δ*f* and α.

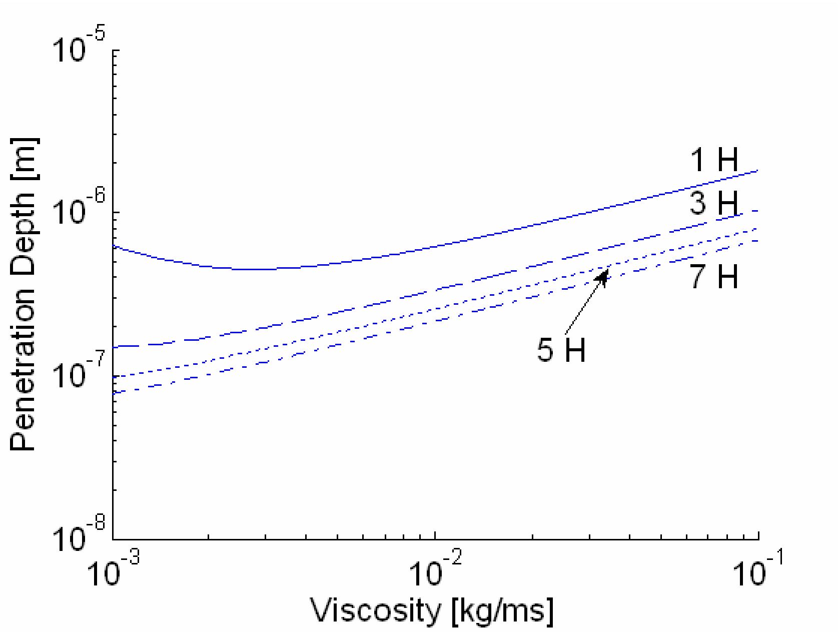

Figure 15. Penetration depth of acoustic shear waves of MTSM as a function of viscosity in harmonics. (ρ = 1000 kg/m^3 and $\mu = 10^5$ N/m^2)

As the harmonic increases the dynamic range of the relative Δ*f* and α are decreased and the region of stabilized MTSM response is getting bigger at higher harmonics due to the smaller penetration depth at higher harmonics. The arrows in each axis indicate the direction of the evaporation-induced deposition process with an increase in viscosity and a decrease in thickness. Figure 15 shows the penetration depths of acoustic shear waves as a function of viscosity in each harmonic. Due to the contribution from the stiffness of the medium, both the relative Δf and α of stage II show stronger oscillatory response of MTSM than stage I with no stiffness.

5.4.3 Effect of changes in stiffness and thickness on the MTSM response: stage III

During the stage **III** of the evaporation-induced deposition process, the stiffness of the VE medium starts to play a significant role in the mechanical properties. The medium is rather gel-type hard rubbery condition due to the relatively high viscosity, stiffness, and higher concentration of solutes than stage **II**. All three variables (viscosity, stiffness, and thickness) are changing during this stage, but the stiffness is the leading element to characterize the hardening or polymerization of the VE medium condition [49]. Therefore, stiffness and thickness are varying while density and viscosity are remaining unchanged for the simulations in this section.

For the contribution of thickness and stiffness, the thickness was varied from 10 μm to 100 *nm*, and the stiffness of the medium was varied from 10^6 to 10^8 N/m^2 to simulate the response of MTSM between hard rubbery to solid like conditions of a layer. The viscosity of the film is assumed to be 0.1 *kg/ms* to reveal the hard rubber gel-type condition of the film and the density was fixed at 1000 kg/m^3 [49]. Figure 16 shows the simulations of the response of MTSM to the changes in thickness and elastic stiffness of VE films and Table 5 list the information about the each element of the simulation in Figure 16.

Table 5. Mechanical properties of the variables in the simulations in Figure 16.

	η (kg/ms)	h (m)	ρ (kg/m^3)	μ (N/m^2)
Hard rubber (initial step)	0.1	10^{-5}~10^{-7}	1000	10^6~10^7
Solid like (final step)	0.1	10^{-5}~10^{-7}	1000	10^7~10^8

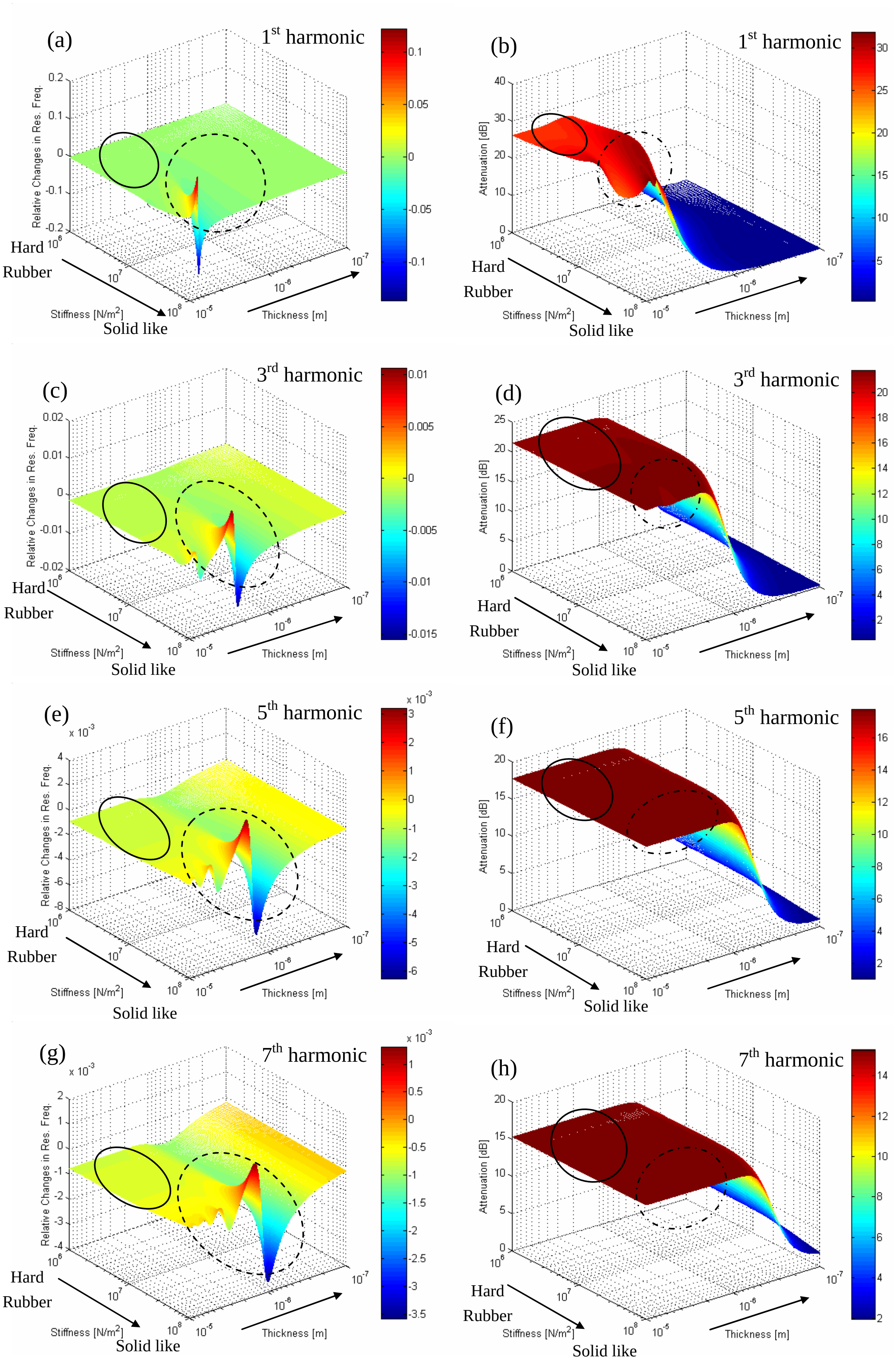
(a)
1st harmonic
Relative Changes in Res. Freq.
0.2
0.1
0
-0.1
-0.2
0.1
0.05
0
-0.05
-0.1
Hard
Rubber
Stiffness [N/m2]
Solid like
Thickness [m]
(b)
1st harmonic
Attenuation [dB]
40
30
20
10
0
30
25
20
15
10
5
Hard
Rubber
Stiffness [N/m2]
Solid like
Thickness [m]
(c)
3rd harmonic
Relative Changes in Res. Freq.
0.02
0.01
0
-0.01
-0.02
0.01
0.005
0
-0.005
-0.01
-0.015
Hard
Rubber
Stiffness [N/m2]
Solid like
Thickness [m]
(d)
3rd harmonic
Attenuation [dB]
25
20
15
10
5
0
20
18
16
14
12
10
8
6
4
2
Hard
Rubber
Stiffness [N/m2]
Solid like
Thickness [m]
(e)
5th harmonic
x 10-3
Relative Changes in Res. Freq.
4
2
0
-2
-4
-6
-8
x 10-3
3
2
1
0
-1
-2
-3
-4
-5
-6
Hard
Rubber
Stiffness [N/m2]
Solid like
Thickness [m]
(f)
5th harmonic
Attenuation [dB]
20
15
10
5
0
16
14
12
10
8
6
4
2
Hard
Rubber
Stiffness [N/m2]
Solid like
Thickness [m]
(g)
7th harmonic
x 10-3
Relative Changes in Res. Freq.
2
1
0
-1
-2
-3
-4
x 10-3
1
0.5
0
-0.5
-1
-1.5
-2
-2.5
-3
-3.5
Hard
Rubber
Stiffness [N/m2]
Solid like
Thickness [m]
(h)
7th harmonic
Attenuation [dB]
20
15
10
5
0
14
12
10
8
6
4
2
Hard
Rubber
Stiffness [N/m2]
Solid like
Thickness [m]
10^6
10^7
10^8
10^-5
10^-6
10^-7

Figure 16. Effect of the changes in stiffness and thickness to MTSM response (relative changes in resonant frequency and absolute values of attenuation in dB). Arrows in each graph indicate the direction of the evaporation-induced deposition process.

When the medium is in a hard rubber condition (solid line circles), it seems that the thickness is no longer affecting the response of MTSM in both relative Δf and α until it is below a couple of penetration depths because relative Δf and α have already reached their stabilized responses. This is similar with thickness and viscosity simulations in previous section 5.4.2. Figure 17 shows the penetration depth as a function of stiffness in harmonics. Stiffness contributes the acoustic energy storage in the medium, so the penetration depth increases as stiffness increases. For the first and third harmonics, the penetration depth has been increased in the order of two as the stiffness increases by the order of two. When the thickness is approaching a couple of penetration depths (dashed line circles), the responses of relative Δf start to show oscillations. As the medium becomes more rigid (increase in stiffness), the magnitudes of the oscillations increase dramatically. These oscillations indicate that the rigid VE medium also resonates at a certain thickness and this additional resonant system influences the overall response of

MTSM, even with an unusually higher resonant frequency than a bare MTSM situation. This phenomenon is also detectable during experiments with real biological samples.

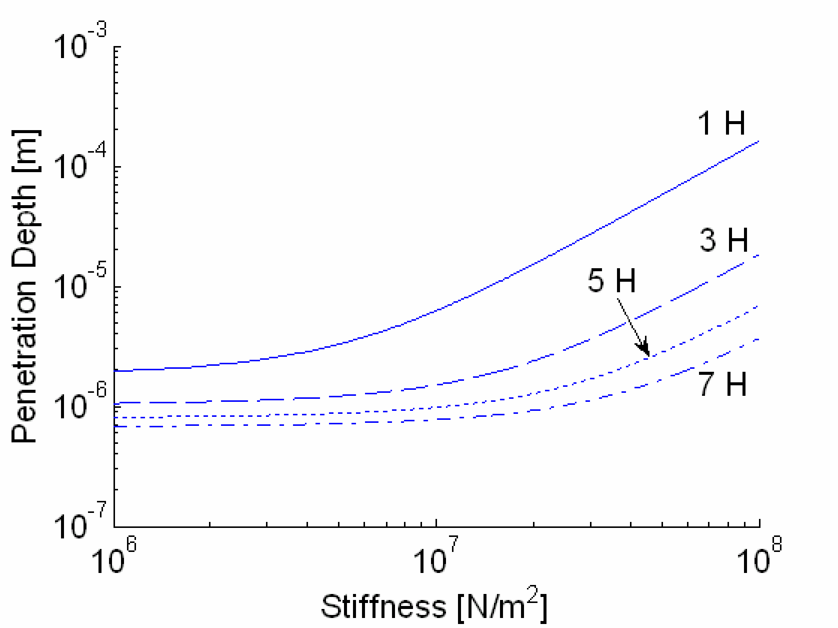

Figure 17. Penetration depth of acoustic shear waves of MTSM as a function of stiffness in harmonics. (ρ = 1000 *kg/m*^{3} and η = 0.1 *kg/ms*)

The attenuation (α) of the MTSM at dashed line circle regions show a less sensitive response than relative Δf graph. When the relative Δf oscillates, the α shows no noticeable changes. At 1st harmonic there are noticeable oscillations, whereas at 3rd harmonic the oscillations are less noticeable and not noticeable at 5th and 7th harmonics. As the thickness of the film becomes smaller than a penetration depth, *Sauerbrey Mass* *effect* and *Kanazawa viscous effect* are evident in both relative Δf and α similar with previous viscosity simulations.

Generally, larger dynamic range of oscillatory response of MTSM in stage **III** was detected when the medium is in rigid condition than stage **II**. This indicates the contribution of the stiffness to the overall response of MTSM. However, stiffness seems not playing significant role for the attenuation changes. Rather thickness is important than the stiffness to analyze the changes in the attenuation.

5.4.4 Effect of changes in viscosity and stiffness on the MTSM response: stage IV

The main factor during the last stage of the evaporation-induced deposition process of biological samples is not thickness but rather shear modulus. The thickness of the medium has been shrunk enough by the evaporation of the solvent during the stage **II** and **III**. The scale of the changes in the thickness in the stage **II** and **III** are remarkably greater than the one in the stage **IV**. During the stage **II** and **III**, the thickness changes at least two to three orders of magnitude (from *mm* to μm), but it only varies in a same order of magnitude during stage **IV**. The materials become more rigid by increasing stiffness and slightly decreasing viscosity to reveal the gradual hardening progress of the materials while there are relatively small changes in the thickness and density. This also can be depicted in drawing (d) in Figure 5. Therefore, different with sections 5.4.1, 5.4.2, and 5.4.3, thickness has been fixed while viscosity and stiffness are varied to simulate the effect of the shear modulus ($G = \mu + j\omega\eta$) to the response of MTSM, where G, μ, j, ω, and η indicate shear modulus, stiffness, $\sqrt{-1}$, resonant angular frequency and viscosity of the VE medium. Graphs in Figure 18 show the simulations with different thicknesses (10^{-5} *m* for (a) and (b), 10^{-6} *m* for (c) and (d), and 10^{-7} *m* for (e) and (f)) at first harmonic responses only. Table 6 and 7 show the information about the variables of the simulations in Figure 18.

When the VE film is relatively thick (h ~ 10 μm, graphs (a) and (b) in Figure 18), it seems that the stiffness has more affect on the response of MTSM than the viscosity since the stiffness is directly connected to the storage of the acoustic energy that is traveling through the medium. The oscillations in graph (a) are not clearly shown except one and this is due to the scale of the ordinate. When the thickness of VE film is approximately 1 μm (graphs (c) and (d) in Figure 18), the oscillatory response of both relative Δf and α are only shown when the film is in a rather hard rubbery condition. As the film becomes more rigid, both relative Δf and α are showing *Sauerbrey mass loading effect* with a certain frequency shift and decreasing in the attenuation. The VE medium is rather behaving as a rigid thin film due to the high stiffness (10^7 ~ 10^8 N/m^2) in this stage. Similar analysis of mass loading effect can be invoked to the graphs (e) and (f) in Figure 18 ($h \approx 100$ nm). The relatively small scale of the ordinate in both relative Δf and α are caused by the small thickness of the VE film during the simulation. Figure 19 shows the penetration depth of 1st harmonic acoustic shear waves of MTSM as a function of stiffness with different viscosity. As a result, for the cases with a fixed thickness, stiffness plays a more important role than viscosity to the overall response of the MTSM sensor.

Table 6. Mechanical properties of the variables in the simulation in Figure 18.

	η (kg/ms)	h (m)	ρ (kg/m^3)	μ (N/m^2)
Hard rubber	0.001~0.01	10^{-5}, 10^{-6}, 10^{-7}	1000	10^6~10^7
Solid like	0.01~0.1	10^{-5}, 10^{-6}, 10^{-7}	1000	10^7~10^8

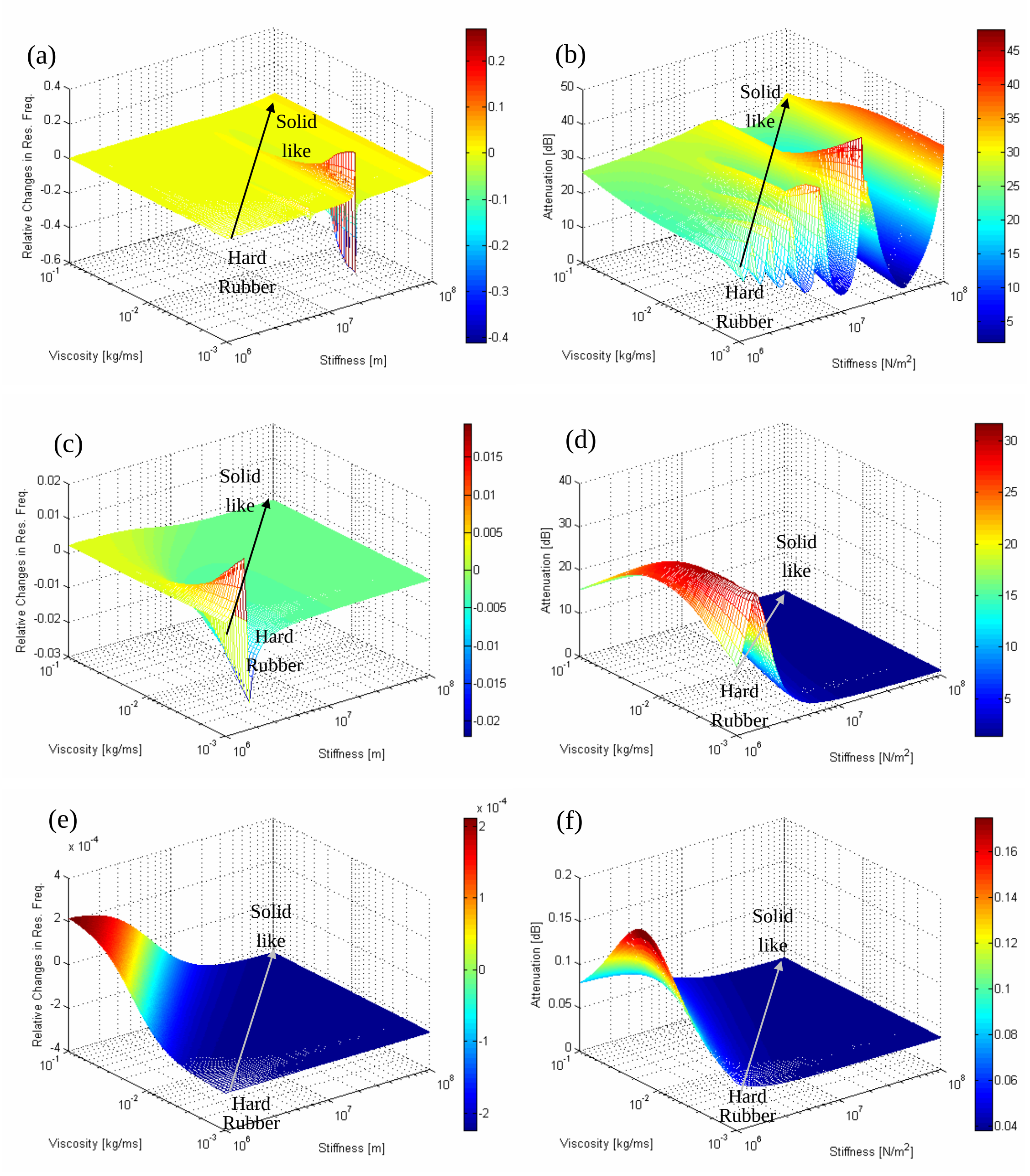

Figure 18. Effect of the changes in the film viscosity and stiffness to MTSM response (relative changes in resonant frequency and absolute values of attenuation in dB). Arrow in each graph indicates the direction of the evaporation-induced deposition process.

Table 7. Summary of the graphs in Figure 18

(a)	1st harmonic: Relative Δf $\boldsymbol{h = 10^{-5}\ m}$	(b)	1st harmonic: Attenuation, α, $\boldsymbol{h = 10^{-5}\ m}$
(c)	1st harmonic: Relative Δf $\boldsymbol{h = 10^{-6}\ m}$	(d)	1st harmonic: Attenuation, α, $\boldsymbol{h = 10^{-6}\ m}$
(e)	1st harmonic: Relative Δf $\boldsymbol{h = 10^{-7}\ m}$	(f)	1st harmonic: Attenuation, α, $\boldsymbol{h = 10^{-7}\ m}$

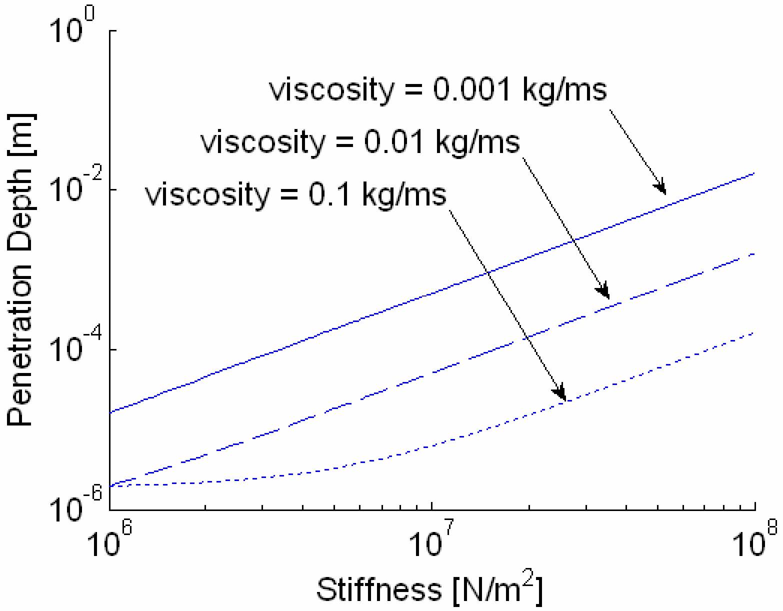

Figure 19. Penetration depth of 1st harmonic acoustic shear waves of MTSM as a function of stiffness with different viscosity. ($\rho = 1000\ kg/m^3$)

5.4.5 Effect of changes in density on the MTSM response

Usually, the variation range of density between a liquid like phase to a solid like material is smaller than the range of viscosity (0.001 ~ 1 *kg/ms*) and elastic stiffness (10^3 ~ 10^9 N/m^2), which varies significantly (at least a couple of orders of magnitude). The density of water is 1000 kg/m^3 while the density of a typical polymer is approximately 800 ~ 1500 kg/m^3 [70]. This explains why the density of previous cases (sections 5.4.1, 5.4.2, 5.4.3, and 5.4.4) of parametric studies was kept at 1000 kg/m^3.

The density was only varied from 500 to 2000 kg/m^3 for the simulation to be in the realistic range. The results showed either a typical *Sauerbrey Mass effect* (decrease or increase in densities mean lighter or heavier the medium becomes) or the *Kanazawa viscous effect* (increase in the product of density and viscosity of the liquid means increase in the mechanical load on the surface of the MTSM sensor, respectively). Graphs in Figure 20 show the effect of density in the response of the MTSM sensor and Table 8 explains the details in the simulations. In the case with graphs (a), (b), (c), and (d), the thicknesses of the VE films are always much larger than the penetration depths of the VE films (see Figure 21 for the penetration depth). Therefore, the MTSM sensor treats the VE film as a load with an infinite thickness film and the *Kanazawa viscous* *effect* [40] is showing in the graphs. As the density of the VE film increase, the relative changes in Δf and α are also increased.

As an acoustic signature, the attenuation of the higher harmonic responses, such as 5th and 7th harmonics, seems not sensitive to the changes in the density of the medium, and the attenuation of the lower harmonics, such as 1st and 3rd harmonics, shows the density effect (as density increases attenuation also increases due to the *Kanazawa viscous effect*). For the case with (e) and (f), the thickness of the VE film is always much smaller than the penetration depth of the VE film, except the 7th harmonic. At 1st, 3rd, and 5th harmonics, the graphs show the typical *Sauerbrey Mass effect.* At the 7th harmonic, as the density increases, the penetration depth of the MTSM sensor becomes close to the thickness of the film and this causes the oscillatory behavior of the MTSM sensor.

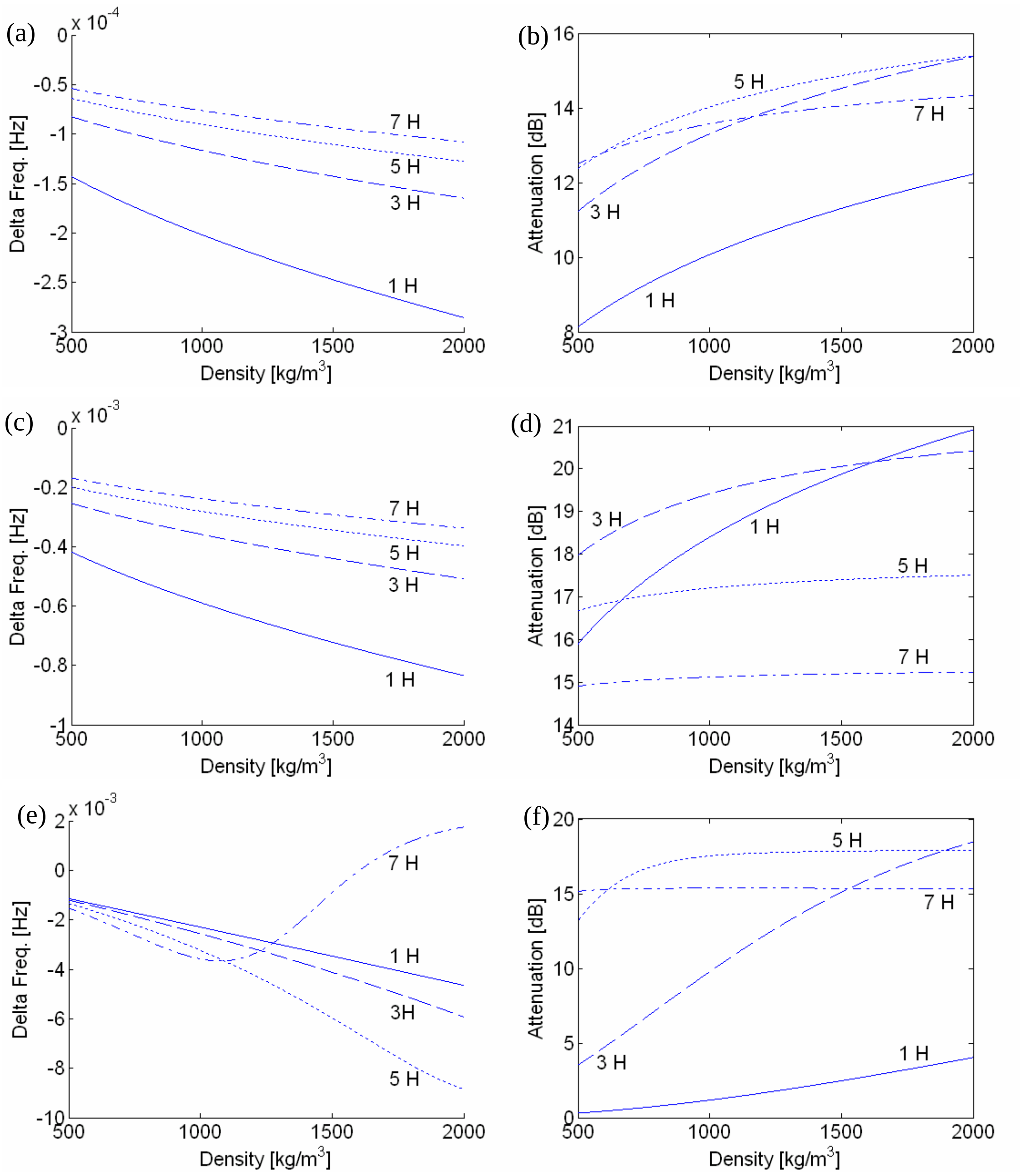

Figure 20. Effect of the changes in the film density to MTSM response (relative changes in resonant frequency and absolute values of attenuation in dB).

Table 8. Mechanical properties of the variables in the simulation in Figure 20.

Graphs	η (kg/ms)	h (m)	ρ (kg/m^3)	μ (N/m^2)
(a) and (b)	0.001	10^{-4}	500 ~ 2000	0
(c) and (d)	0.01	10^{-5}	500 ~ 2000	10^5
(e) and (f)	0.1	10^{-6}	500 ~ 2000	10^8

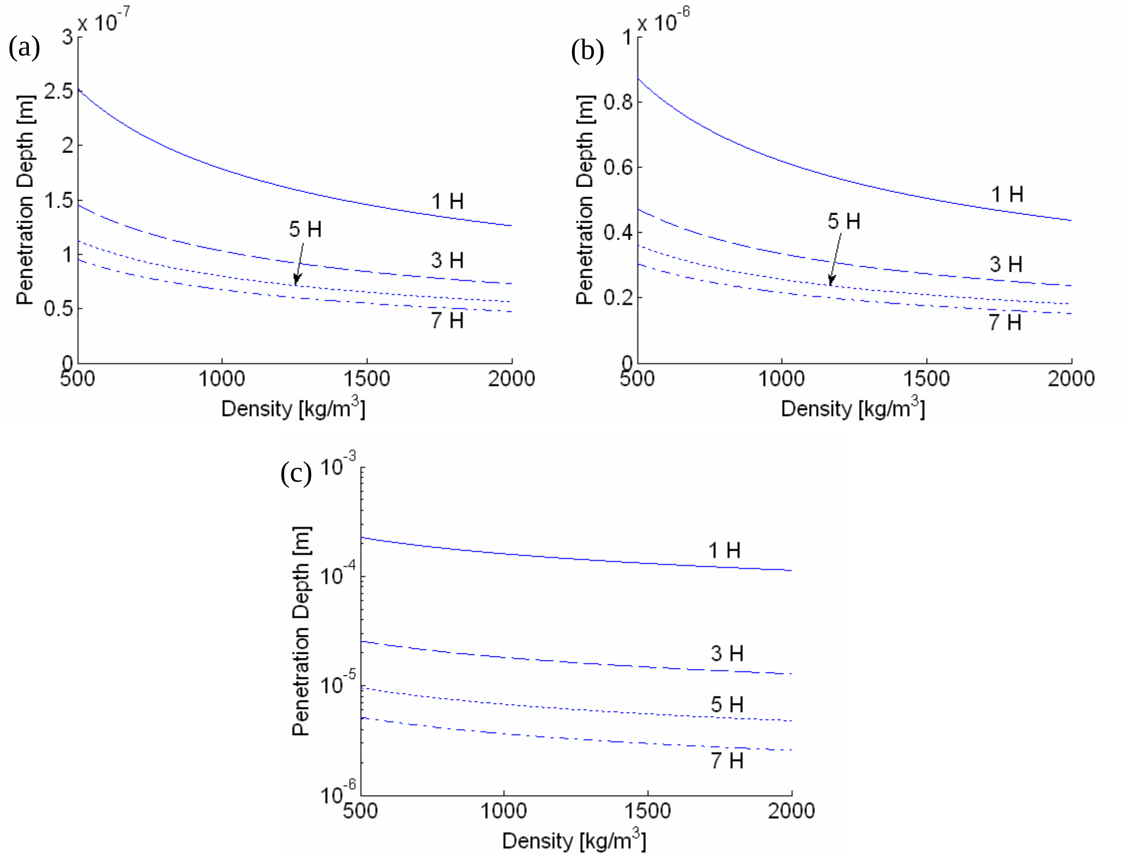

Figure 21. Penetration depth of acoustic shear waves of MTSM as a function of density for different harmonics. (a) penetration depth of the graphs (a) and (b), (b) penetration depth of the graphs (c) and (d), and (c) penetration depth of the graphs (e) and (f) in Figure 20.

5.4.6 Applications of the concept of signatures of a MTSM for analysis of the deposition process

In this section specific cases are discussed with the use of MTSM sensor technology based on the results of previous simulations, and the acoustic signatures of the response of MTSM sensor are also discussed. Previous surface mesh graphs are sliced and line graphs are prepared to study the case with more specific conditions of the VE loading on the MTSM sensor.

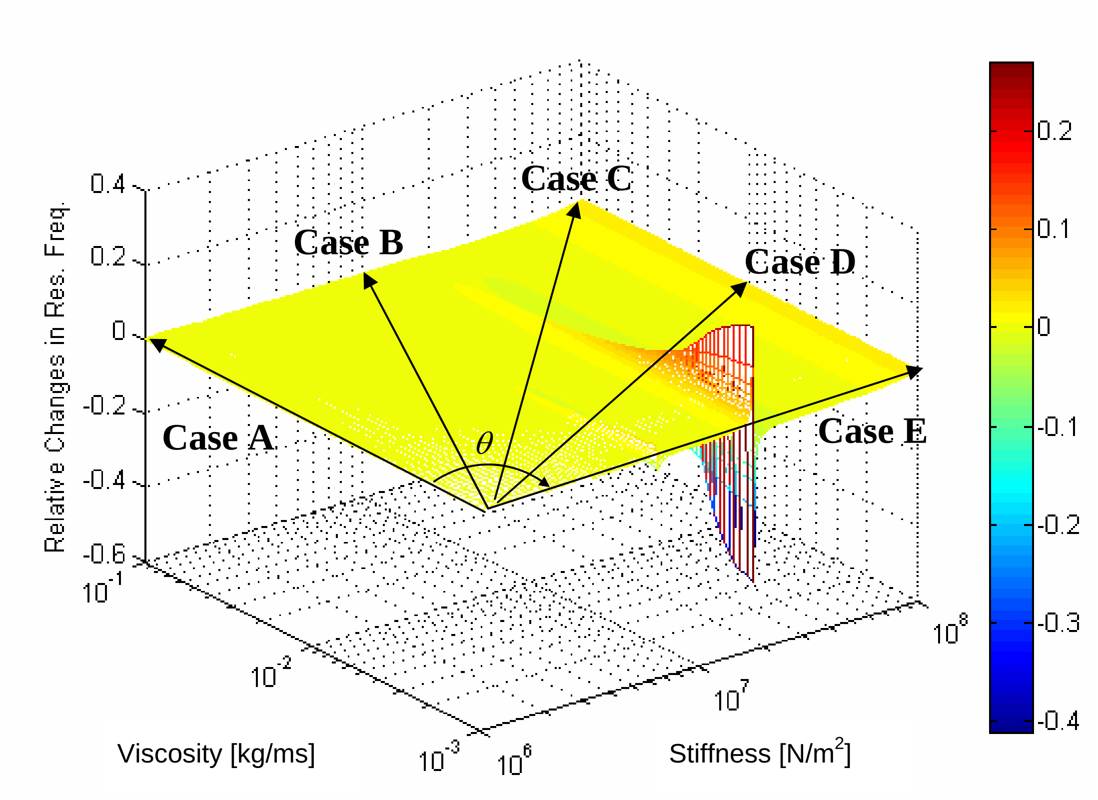

Figure 22. Surface mesh graph with five different hypothetical paths on the surface.

The surface mesh graph with shear modulus (viscosity and stiffness) as variables and five different hypothetical paths (case A to E) on the mesh are showing in Figure 22. Depending on the direction or path of the slice, the resulting line graph indicates the different signature. Each path on the mesh is categorized by the angle (θ) from the viscosity axis.

The path of 'Case A' in Figure 22 indicates the signature of a medium that has constant thickness (10 μm) and stiffness (10^6 N/m^2), and varying viscosity (0.001 ~ 0.1 *kg/ms*). The sliced line graph of 'Case A' is shown in Figure 23. The results show a signature of the viscosity driven process because only viscosity is varying during the process. Along the path, there are increments of damping of the acoustic energy due to the increase in the viscosity of the medium.

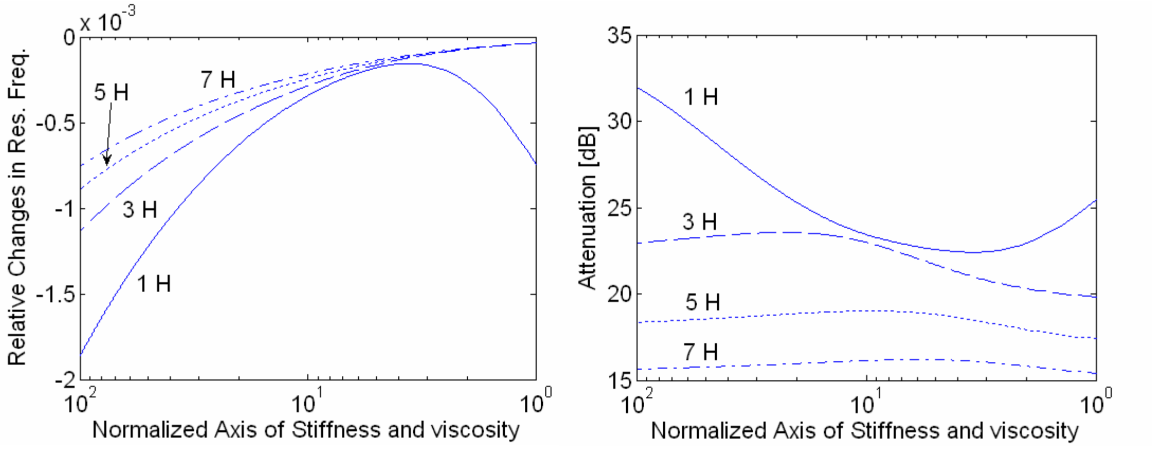

Figure 23. Case A ($\theta \approx 0°$): A signature of the viscosity (η) driven process

The relative Δf and α graphs of all the harmonics show a similar trend except 1st harmonic. Because of the penetration depth of 1st harmonic commensurate with the thickness, 1st harmonic response shows oscillatory response when the viscosity is between 10 and 1 on the arbitrary x-axis on the graphs in Figure 23. Penetration depths of higher harmonics, such as 3rd, 5th, and 7th are smaller than the thickness of the film in this case.

The path of ‘Case B’ in Figure 22 is the signature of the process that has more contribution from viscosity than stiffness. In this path, viscosity is changing two orders of the magnitude (from 0.001 to 0.1 kg/ms) while stiffness is changing only 10 times (from 10^6 to 10^7 N/m^2). In other words, this path can be analyzed as a Case A path with an additional contribution from the stiffness. Figure 24 shows the line graph of the path ‘Case B’ on the mesh with higher harmonics, too. There are more effects from damping than storing of the acoustic energy in to the medium due to the more contributions from the viscosity than the stiffness factor.

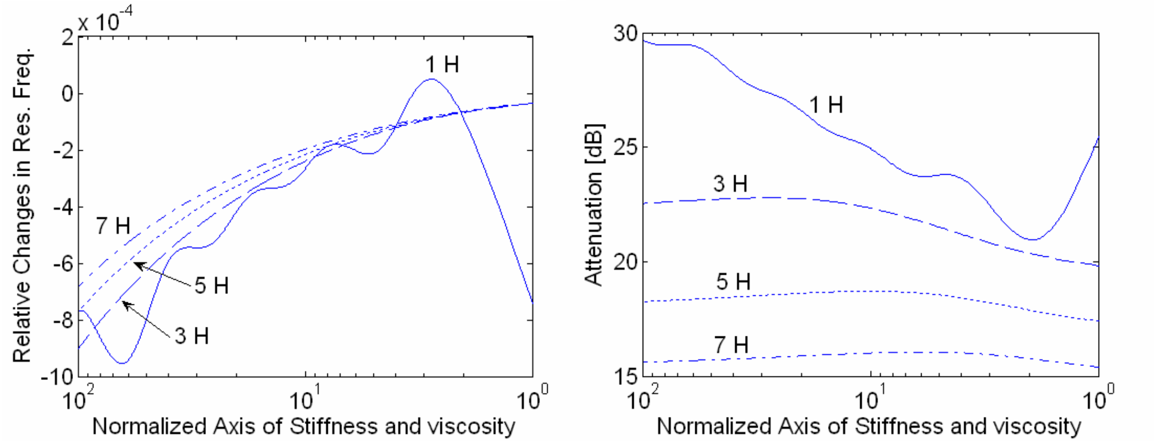

Figure 24. Case B ($\theta \approx 27°$): A signature of the viscosity (η) > stiffness (μ) driven process

Involvement of stiffness in this Case B increases the penetration depths of all the harmonic responses than the Case A. The penetration depth of 1st harmonic is always greater than the thickness of the medium through the normalized axis of stiffness and viscosity, but still the penetration depths of higher harmonics are smaller than the thickness. Therefore, only 1st harmonic response shows the oscillatory behavior that is stronger than the Case A in Figure 23.

The path of ‘Case C’ in Figure 22 indicates the signature that involves viscosity and stiffness with similar impacts in the process. Both viscosity and stiffness are changing two orders of magnitude during the process. The viscosity is changing from 0.001 to 0.1 *kg/ms* same as previous Case A and B and stiffness is changing from 10^6 to 10^8 N/m^2.

Therefore, the contribution from the stiffness is stronger than the Case B and the result of the stronger impact from the stiffness is shown by the larger magnitude of oscillatory response of MTSM sensor in Figure 25.

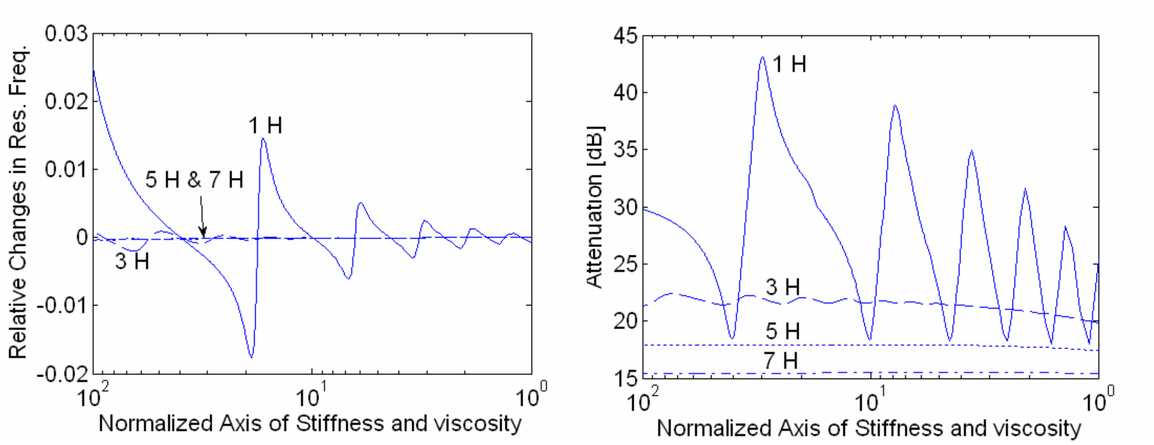

Figure 25. Case C ($\theta \approx 45°$): A signature of the viscosity = stiffness driven process

In this case, the penetration depths of each harmonic are increased than the Case B because of the increased stiffness. Besides the fact that the larger magnitude of the oscillatory response of 1st harmonic response than the Case B, as a first time, 3rd harmonic response starts to show the oscillatory response like 1st harmonic which indicating the penetration depth of 3rd harmonic is also similar with the thickness of the medium. As the medium becomes more rigid condition, the magnitudes of the oscillatory response in both relative Δf and α are also increased because of the increasing stored acoustic energy in the medium.

The path of 'Case D' in Figure 22 reveals the signature that has more impact from the stiffness than from the viscosity during the process. The viscosity is only changing 10 time (from 0.001 to 0.01 *kg/ms*) while the stiffness is changing two orders of magnitude (from 10^6 to 10^8 N/m^2). There are more effects from storing than damping of the acoustic energy in the medium because of more involvement from the stiffness than the viscosity.

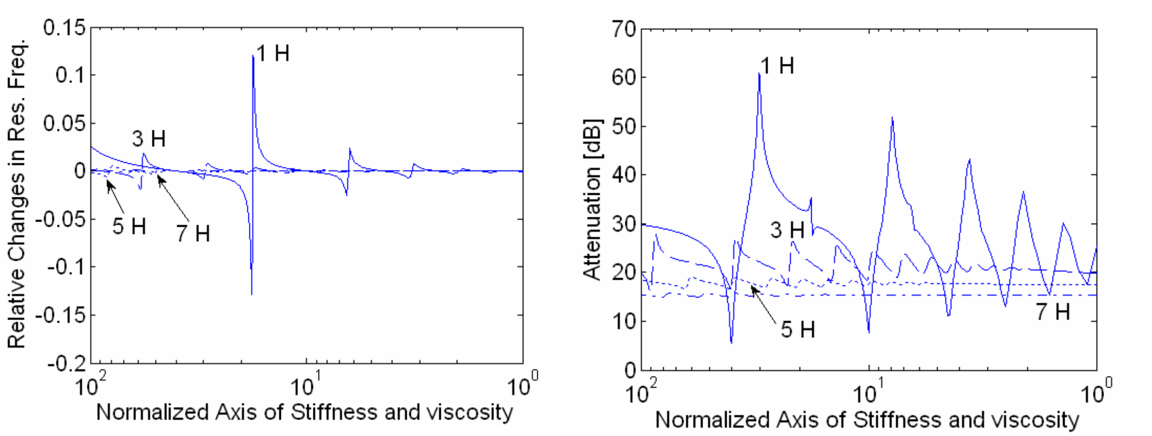

Figure 26. Case D ($\theta \approx 72°$): A signature of the viscosity < stiffness driven process

The oscillatory responses of MTSM sensor are showing in 1^{st}, 3^{rd}, and 5^{th} harmonics in Figure 26, because the penetration depths of 1^{st}, 3^{rd}, and 5^{th} harmonic are smaller than the thickness of the medium. Due to more effect from the stiffness than the viscosity, the magnitudes of the oscillatory response of MTSM sensor are greater than previous cases A, B, and C.

Finally, the path of ‘Case E’ in Figure 22 is the signature that has only stiffness contribution during the process. The viscosity is constant at 0.001 *kg/ms* while the stiffness is changing from 10^6 to 10^8 N/m^2. Therefore, the all the contributions during the process are caused by the increase in the stiffness only.

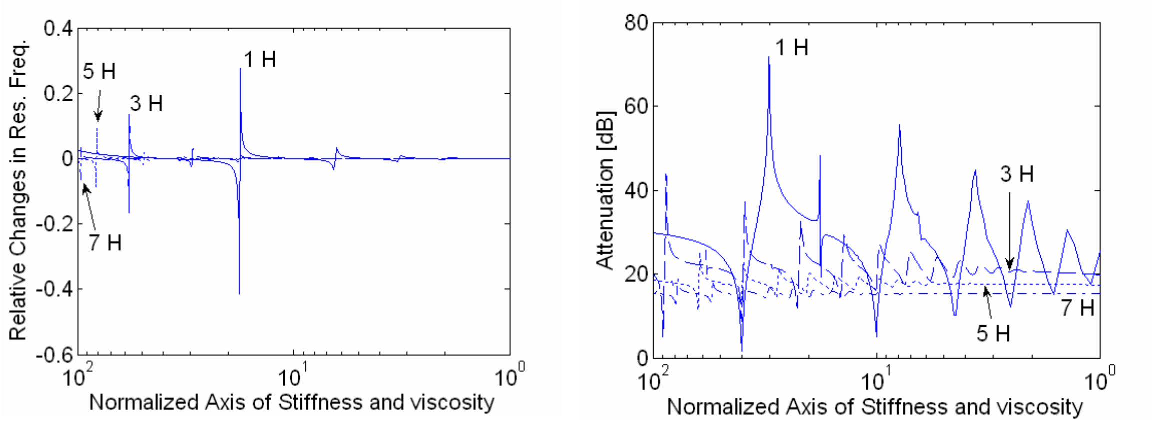

Figure 27. Case E ($\theta \approx 90°$): A signature of the stiffness driven process

In this case, the oscillatory responses of a MTSM sensor are showing in all the harmonics because the penetration depths of all the harmonics are greater than the thickness of the medium. Since the contribution only comes from the stiffness, the magnitude of the oscillatory response of a MTSM sensor in this case shows maximum values in both the relative Δf and α graphs.

5.5 Simulation of a MTSM for an evaporation-induced deposition process of collagen and albumin

This section describes the simulation of an evaporation-induced deposition process of collagen and albumin as a case study. Section 5.5.1 provides the method of the simulations. Section 5.5.2 and 5.5.3 describe the modeling of the collagen and albumin, respectively.

5.5.1 Methodology

The changes in the attenuation, α, (equation 4) and relative Δf (equation 5) of MTSM sensor to the evaporation-induced deposition process of collagen and albumin samples has been simulated using MatLab software. The model requires four variables, such as density (ρ), elastic stiffness (μ), viscosity (η), and thickness (h) to simulate the relative Δf and α of the MTSM sensor. The thicknesses of collagen and albumin were obtained by indirect method of measuring the mass of solution of collagen and albumin samples during the evaporation process. The same MTSM sensor holder with collagen or albumin sample was placed inside of the microbalance. The side windows of the microbalance were closed while the top window was maintained to be opened during the entire measurement. The changes in the mass of collagen or albumin solution during the evaporation process were recorded every 30 seconds. Then, the mass changes were converted to the changes in the thickness by assuming the fixed density of the sample at 1000 kg/m^3 due to the low concentration of the solution (1 *mg/ml*). The viscosity and stiffness of the samples under high frequency (> 10 *MHz*) were taken from the previous work and literatures [63, 71]. Figure 28 shows the resulting thickness changes of collagen and albumin during the evaporation-induced deposition process. Then this thickness graphs were converted to mass fraction of free solution ($MF_{free\text{-}solution}$) curves based on the following equations.

$$MF_{free-solution} = \frac{M_{\infty}}{M_{\infty} + M_{free-solution}} \quad \ldots\ldots\ldots\ldots\ldots\ldots\ldots\ldots\ldots\ldots\ldots\ldots\ldots.(7)$$

where M_∞ and $M_{free\text{-}solution}$ indicate final stabilized mass of the collagen sample from the microbalance measurement and mass of the sample during the process. Figure 29 shows the mass fraction of free solution curves of collagen and albumin.

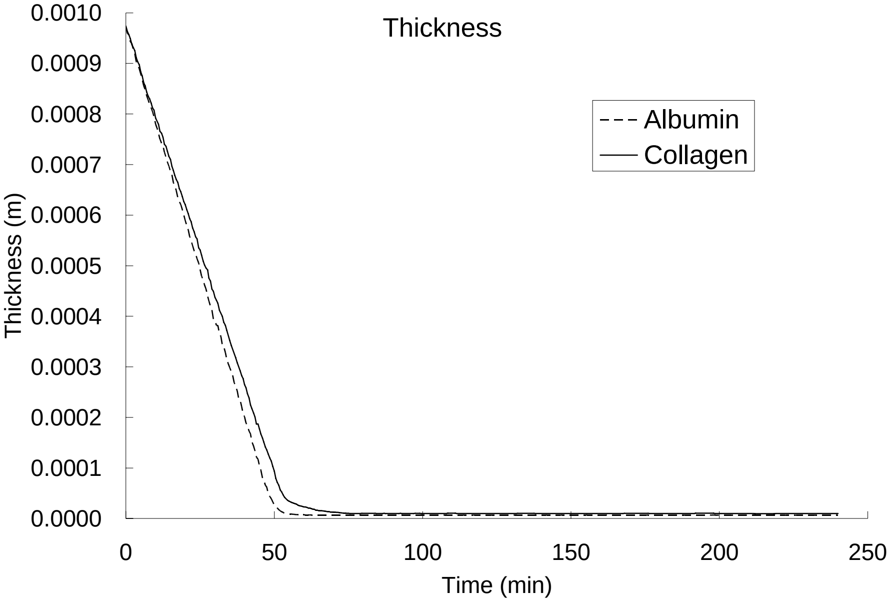

Figure 28. Changes in the thickness of collagen and albumin during the evaporation process

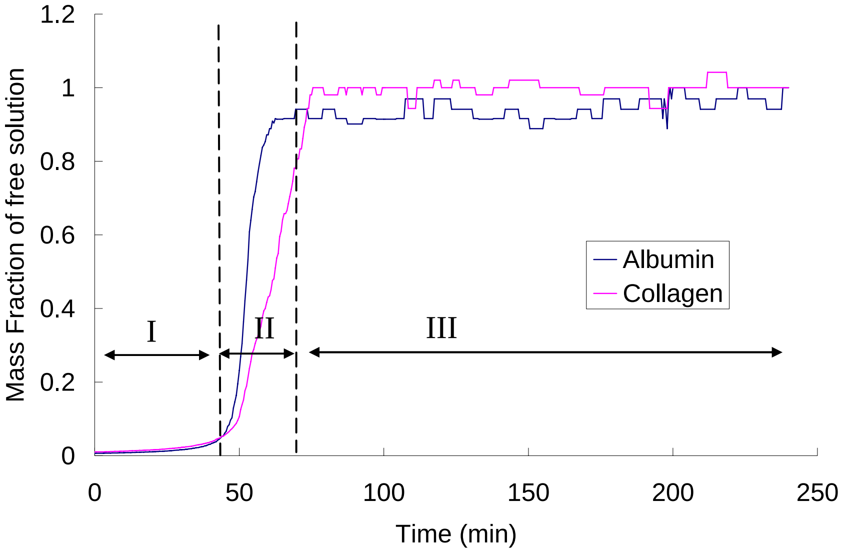

Figure 29. Mass fraction of free solution curves of collagen and albumin samples during the entire evaporation-induced deposition process

Basically the mass fraction of free solution graphs can be divided into three regions, such as region I, II, and III. First, the region I can be described by approximately constant rate of mass fraction of free solution curve. In this region, the sample is in a solution with a dilute solute due to the low concentration (1 *mg/ml*). Next, the region III can be identified by its stable responses. In this region, there is no change in the mass fraction of free solution and this means that most of the solvent is already evaporated and left only agglomerated solute. Finally, the region between region I and III is the region II and it can be described with its falling rate of increase in the mass fraction of free solution. The different slope between collagen and albumin is caused by the different ambient conditions, such as air flow on the top window of the microbalance, temperature, humidity, etc.

5.5.2 Modeling collagen

Collagen is a fibrous protein found mostly in skin, bone, and other connective tissues of animals. Due to a unique triple helix configuration of three polypeptide subunits known as α-chains, it usually is in a form of fibrous shape called fibrils (see Figure 30). An individual fiber varies in a diameter from less than 1 μm to approximately 12 μm. It is composed of fibrils, and the fibers are usually arranged in bundles. Therefore, they form more compact and aligned thin rigid film at the end of the evaporation-induced deposition process [12, 72].

The viscoelastic mechanical properties of collagen during the evaporation process are mainly depend on the concentration of the collagen solutes and the condition of the fibrous collagen protein. There are some reports about the elastic modulus of collagen cartilage from the superficial zone with approximately 7.0 *GPa* parallel and 2.21 *GPa* perpendicular to the cleavage line pattern [73] and in vivo viscoelastic mechanical properties of the carotid artery by analyzing the elastin and collagen [74].

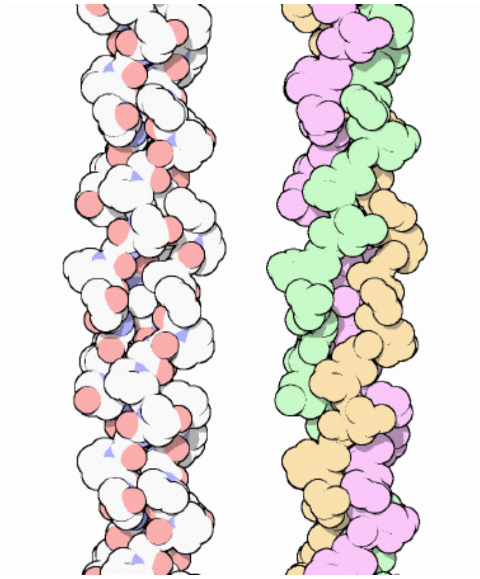

Figure 30. α-chains of collagen [75].

Figure 31 show the hypothetical changes in the viscosity and the stiffness of collagen sample for the simulation of the evaporation-induced deposition process. Four regions (**I**, **II**, **III**, and **IV**) in Figure 31 are categorized by the analysis of a typical evaporation process of biological sample in Figure 5, the mass fraction of free solution graph in Figure 29, and experimental results of MTSM sensor with collagen sample in Figure 39 and 40.

The initial viscosity and stiffness were set at the value of water (0.001 *kg/ms* and 0 *N/m*^{2}) to represent the water like condition and maintained at similar value to indicate the stage **I**. This stage **I** in Figure 31 also corresponds to region **I** in Figure 29. At the end of the stage **I (**about 40 minutes), the viscosity starts to increase suddenly because of the increase in the concentration of the collagen solute [68]. The stiffness is maintained at the liquid like value to describe the phase transition of the medium from water like to a higher viscous soft rubber condition. The stiffness of the sample starts to increase (up to 10^7 *N/m*^{2}) at the middle of the stage **II** while the viscosity is already high (0.1 ~ 1 *kg/ms*) [73, 74]. This stage **II** corresponds to region **II** in Figure 29. During the stage **III**, the stiffness of the sample keeps increase (up to 10^9 *N/m*^{2}) and the viscosity decrease slightly (from ~ 1 to 0.7 *kg/ms*) to describe the hardening and fibrillation processes of the collagen sample [37, 50, 63, 76]. The viscosity and stiffness are generally fixed at the end of the stage **III** and stayed during the stage **IV** to reveal the final stabilization process of the evaporation-induced deposition process of collage sample. These stages **III** and **IV** correspond to region **III** in Figure 29.

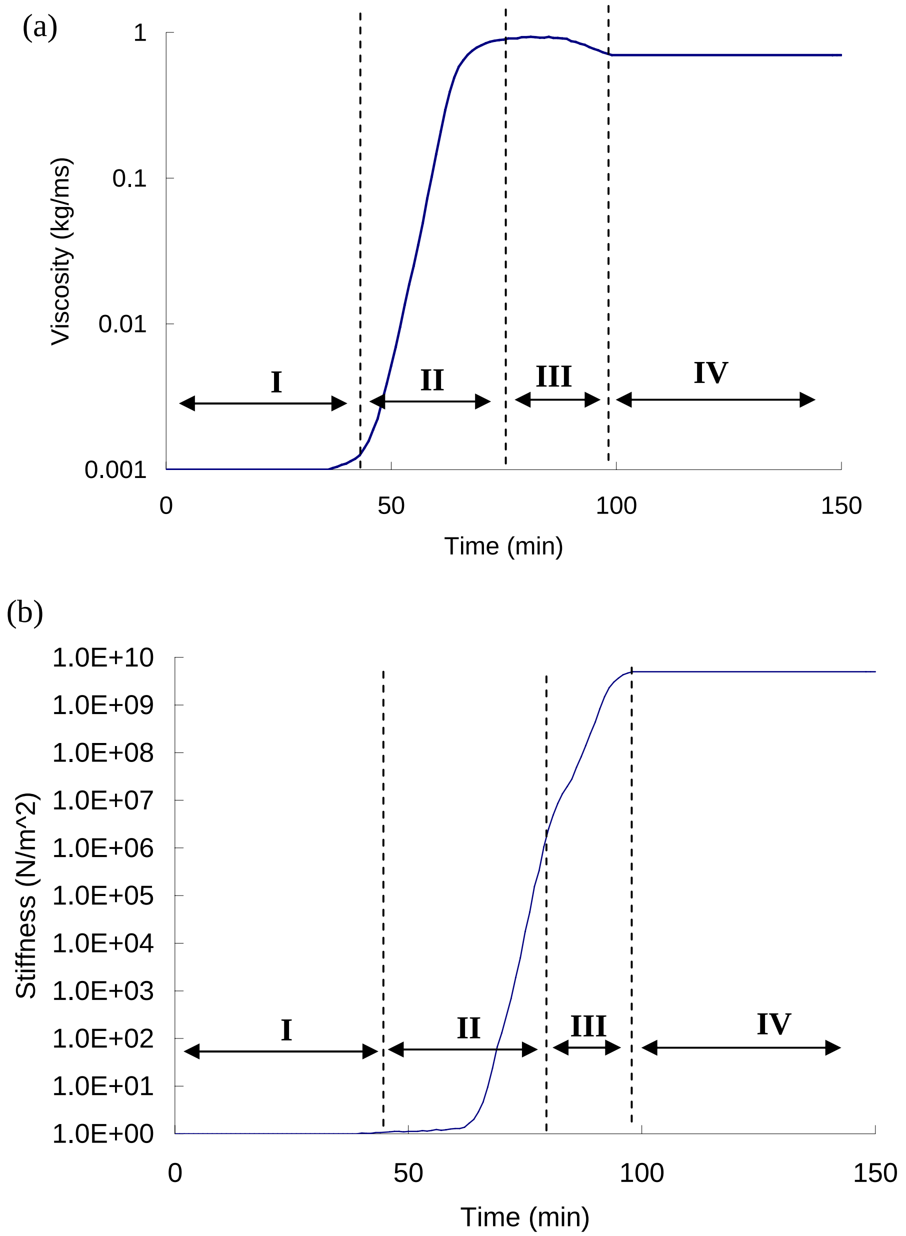

Figure 31. Hypothetical changes in the (a) viscosity and (b) stiffness of collagen sample during the simulation of the evaporation-induced deposition process.

Figure 32 shows the results of the simulation that represents the evaporation-induced deposition process of collagen sample. Both graphs specify clear indication of each stage. Because of the relatively high thickness of the film than the penetration depth of the acoustic waves, both relative Δf and α show stabilized response of a MTSM sensor in the stage **I**. In Figure 31, the viscosity of the film starts to increase earlier than the stiffness. Slight increases in the viscosity result more effect on the α than the relative Δf and this can be seen from graphs in Figure 32 at the end of stage **I**.

During the stage **II**, both the viscosity and stiffness increase. Since the viscosity keeps increasing while the stiffness just starts to increase at the first part of the stage **II**, it seems that the viscosity is a dominant factor for the response of the MTSM sensor in the first part of the stage **II**. This can be explained by the sudden decrease in the relative Δf causing by the viscous loading effect. During the second part of the stage **II**, the stiffness starts to play important role even the film is still in a soft rubbery condition. After the stiffness of the film reaches certain value (about $10^5 \sim 10^6$ N/m^2), the response of the MTSM sensor shows a different behavior because of the contribution from the stiffness of the film. In the relative Δf graph (a) in Figure 32, this can be seem by decrease in the changes in the resonant frequency. Also in graph (b), the slope of the decreasing attenuation (α) becomes smaller due to the increase in the stiffness of the film.

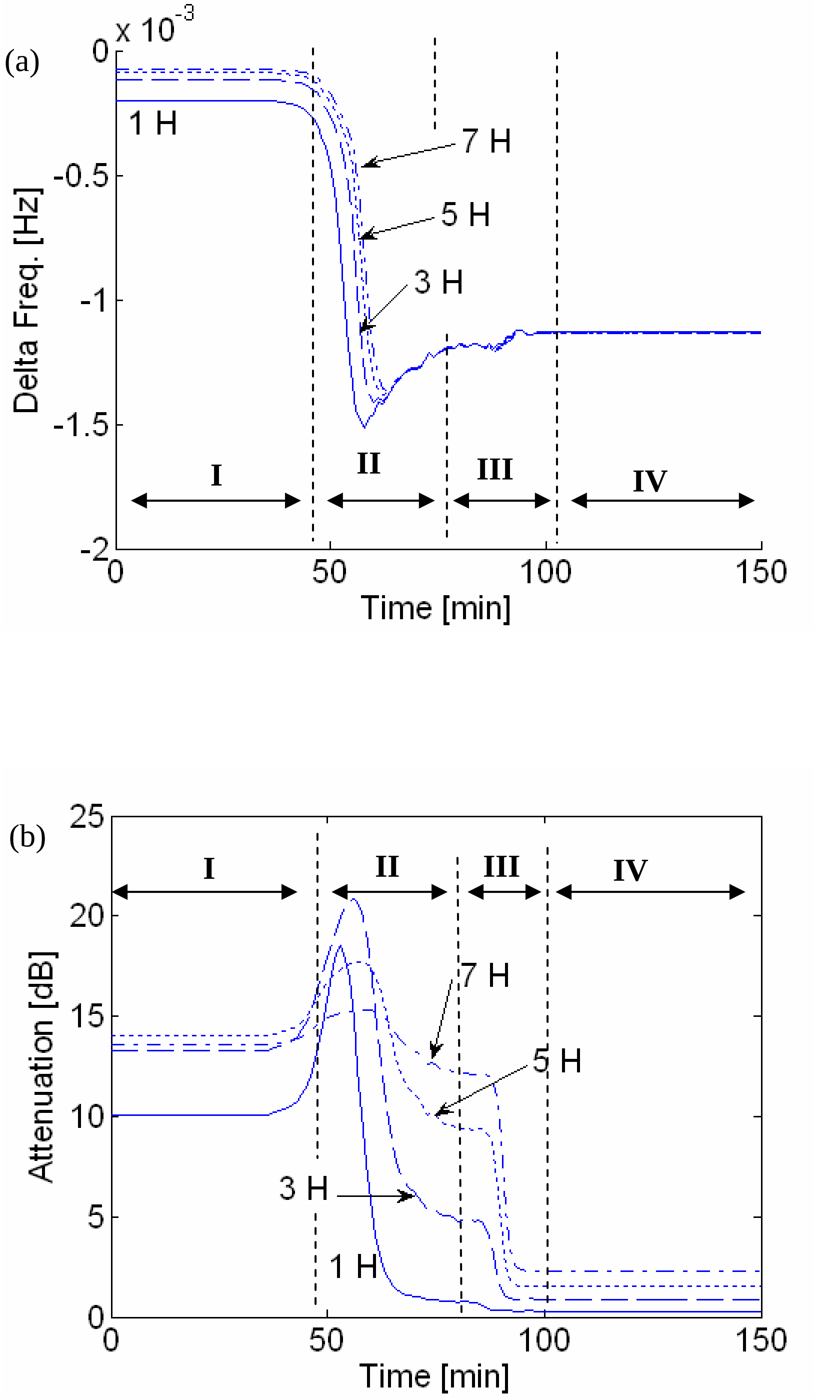

Figure 32. Simulation of the evaporation-induced deposition process of collagen sample. (a) Relative changes in the resonant frequency and (b) attenuation of each harmonic.

During the stage **III**, the viscosity starts to decrease after it reaches its maximum at about 1 *kg/ms* and the stiffness seems to reach its maximum. This decrease in the viscosity causes the decrease in the relative Δf at the beginning part of the stage **III**. The high value of the stiffness (~ 10^8 N/m^2) affects the sudden decrease in the attenuation graph at the end of the stage **III**. Obviously, stabilized viscosity and stiffness result also stable response of the MTSM sensor during the final stage **IV**.

5.5.3 Modeling albumin

Albumin is a type of simple protein that is soluble in pure water and widely distributed throughout the tissues and fluids of plants and animals. It is precipitable from solution by strong acids and coagulable by heat in acid or neutral solution. It can be easily found in egg whites, blood, lymph, and other tissues and fluids [77]. Albumin has a cylindrical shape with approximately 14 × 4 *nm* dimensions and Figure 33 shows a simulated picture of albumin. There are some reports about the viscoelastic mechanical properties of bovine serum albumin [78, 79].

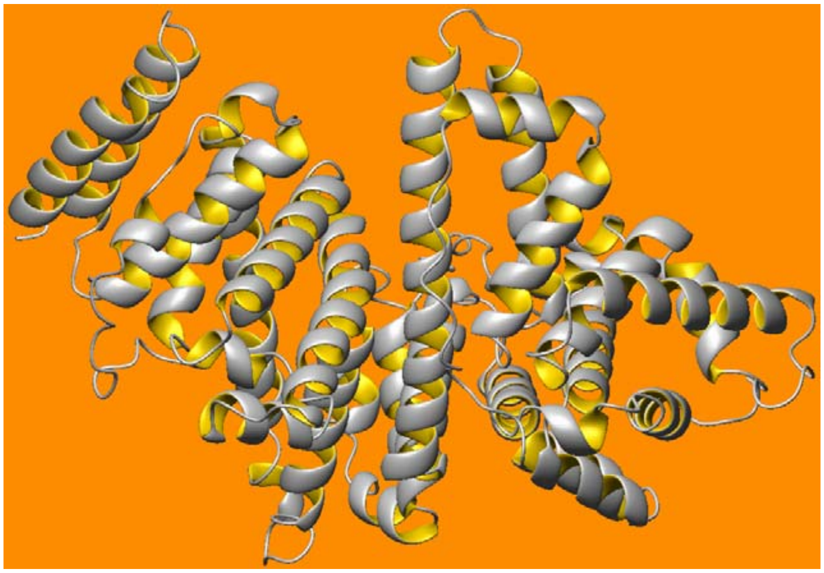

Figure 33. An image of albumin [80].

When albumin starts to coagulate, it becomes rather amorphous cluster while collagen forms a polycrystalline structure. Again, four regions (**I**, **II**, **III**, and **IV**) in Figure 34 are categorized based on the mass fraction of free solution graph in Figure 29 and experimental results of MTSM sensor with albumin sample in Figure 39 and 40. The viscosity of albumin simulation is similar with the one of collagen. It starts with water like value (0.001 *kg/ms*) at stage **I**. The viscosity of albumin is increased up to its maximum value (~ 1 *kg/ms*) during the stage **II**, and slightly decreased (~ 0.5 *kg/ms*) to

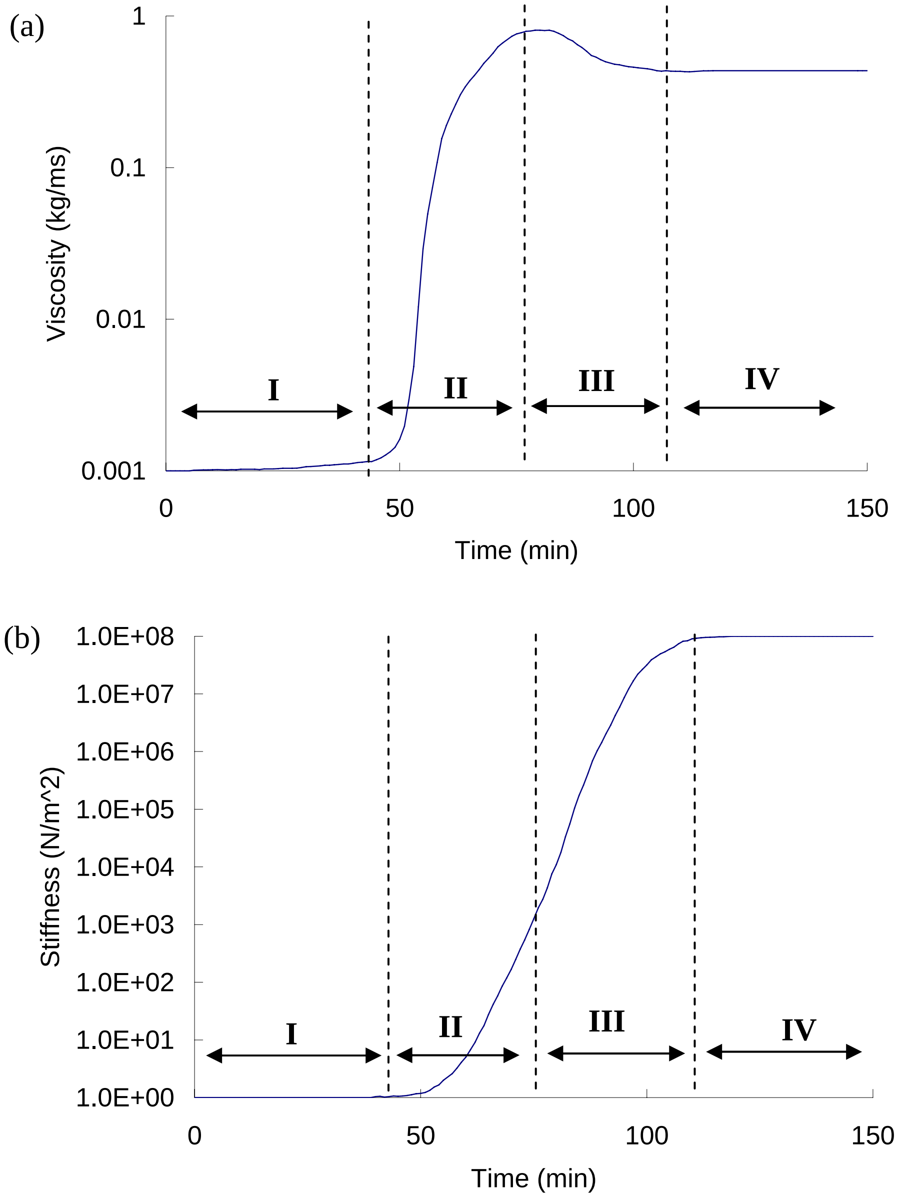

Figure 34. Changes in the (a) viscosity and (b) stiffness of albumin sample during the simulation of the evaporation-induced deposition process.

reveal the hardening process during the stage **III** [37, 50, 78]. The value of the stiffness of albumin is set to be similar with collagen at the stages **I** and **II**, but, at the stage **III**, it is set to be lower (~ 10^8 N/m^2) than collagen (~ 10^9 N/m^2) to indicate the softer characteristic of an albumin film than collagen film. Finally, the viscosity and stiffness of the stage **IV** is expressed by the stable values of both viscosity and stiffness, same as the collagen simulation. Figure 34 shows the actual values of viscosity and stiffness that are used for the evaporation-induced deposition process of albumin sample.

The signature of whole evaporation-induced deposition process of albumin sample has been simulated using four variables (thickness, density, viscosity, and stiffness) and shown in Figure 35. The thickness of the albumin was obtained by in-direct method of monitoring the mass changes of albumin sample, same as collagen, and the density of albumin was fixed at the value of water (1000 kg/m^3).

The stage **I** is same as collagen case by showing stable response of the MTSM sensor since the parameters for the simulation are similar. In stage **II**, the magnitudes of the relative Δf and α of albumin are larger than collagen due to the faster increment of the viscosity of albumin than collagen. However, at the higher harmonics, such as 5th and 7th, the attenuation shows stable response while 1st and 3rd shows a typical decreasing response due to the effect from the high stiffness. Stage **III** and **IV** are similar with collagen case. Because of the decrease in the viscosity, the relative Δf and α also decrease, and finally show the stabilized response of the MTSM sensor.

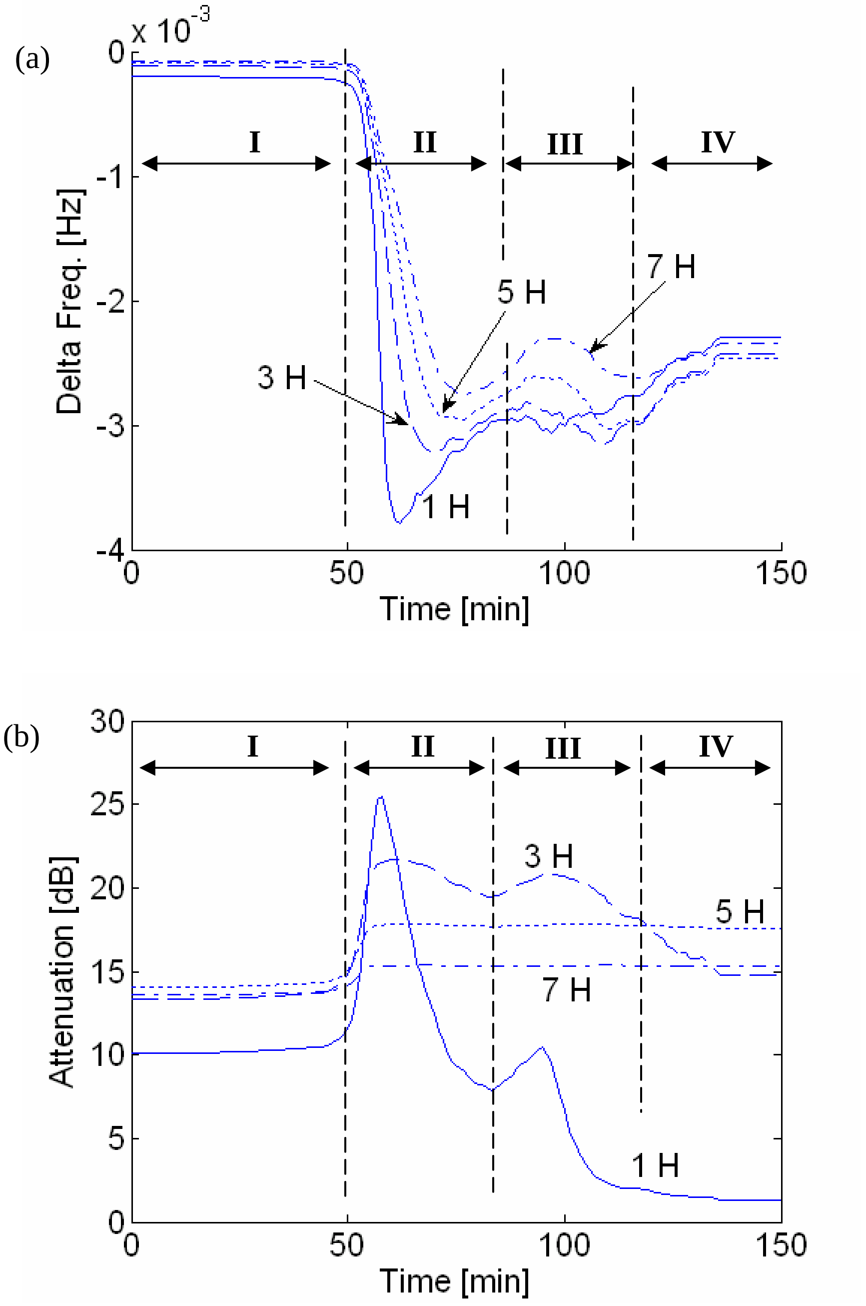

Figure 35. Simulation of the evaporation-induced deposition process of albumin sample.

(a) Relative changes in the resonant frequency of each harmonic and (b) attenuation.

6 EXPERIMENTAL ANALYSIS OF MTSM

In this chapter, first, the development of a MTSM measurement system is described. Next, for the calibration purpose, the signature of an evaporation process of a Newtonian liquid (Deionized water) has been analyzed using the MTSM measurement system. Finally, after the calibration of the MTSM system, the signature of an evaporation process of biological samples (collagen and albumin) has been characterized by using the MTSM measurement system. In addition, the biological samples were analyzed using optical, AFM, and SEM devices.

6.1 Development of a MTSM measurement system

The MTSM measurement system is simple to operate compared with the existing biological sample measurement techniques described in earlier chapters. There is neither fluid flow nor any moving parts, and it requires only a small amount (approximately 100 ~ 50 μl) of target biological sample. The key element of the MTSM measurement system is an interchangeable piezoelectric sensor in a form of a disk on which a thin biological film is formed. The sensor surface consists of gold that is biocompatible and amenable to surface treatments, such as gelatin, poly-L-lysine, thiol functionalized molecules, or fibronectin coating, commonly used in standard anchorage-dependent biological culture procedures. Figure 36 shows the HP-4395A Network Analyzer (NA) based measurement system that has been used for this experimental study. During the experiments, only one side of the TSM sensor was loaded with the target samples. The sensor was connected to the NA to generate a shear oscillation at each harmonic and to measure the S_{21} frequency response of the MTSM sensor. The MTSM sensor with 10 *MHz* fundamental resonant frequency was used in this experiment and the MTSM sensor was excited at 1^{st}, 3^{rd}, 5^{th}, and 7^{th} harmonics (approximately 10 MHz, 30 MHz, 50 MHz, and 70 MHz) using the Network Analyzer (NA). All the measurements were performed in an air flow controlled chemical hood. The ambient temperature was consistently kept at room temperature (approximately 25 °C ± 3°C) with humidity approximately 40 ~ 50 %.

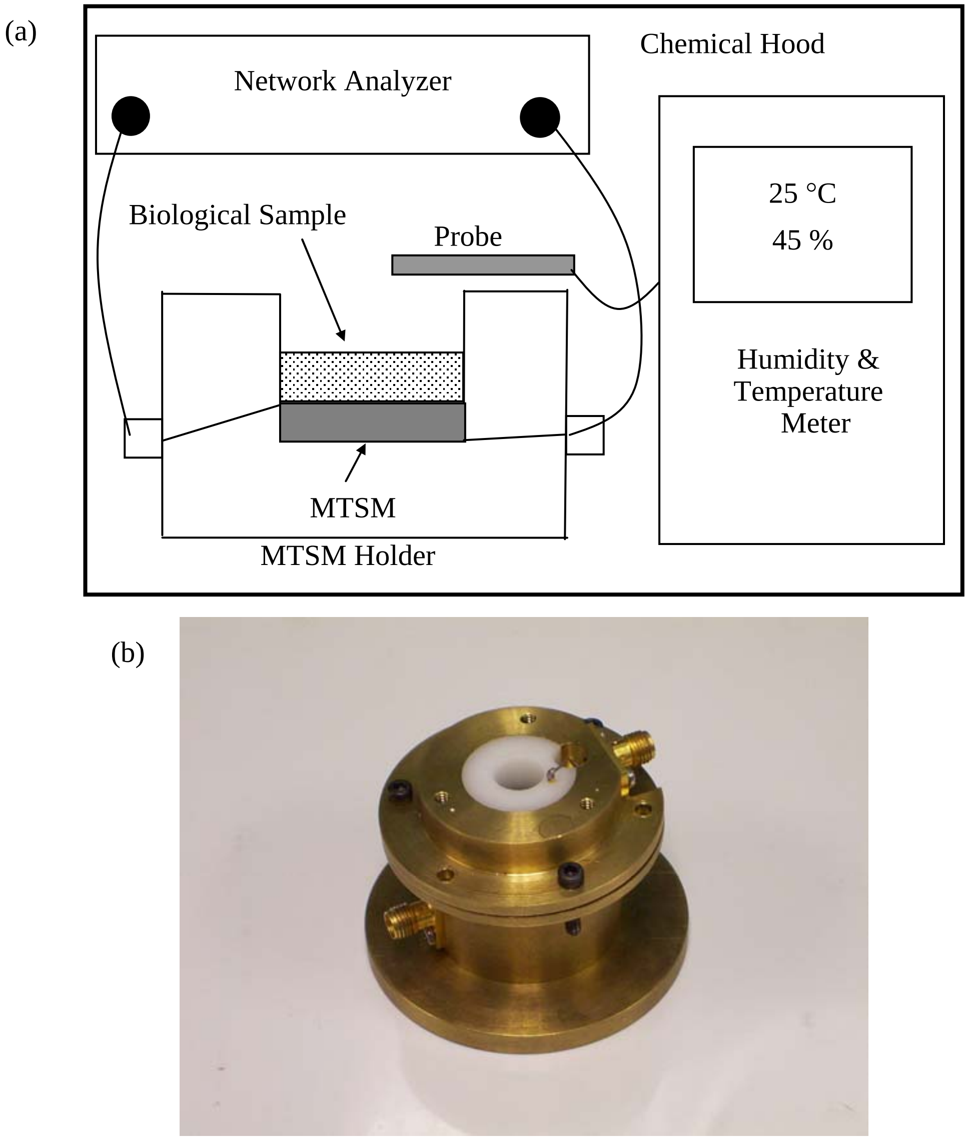

Figure 36. (a) MTSM measurement system with a humidity & temperature meter in chemical hood and (b) image of a MTSM holder.

6.2 Validation of a MTSM measurement system using an evaporation process of a Newtonian liquid

As a validation process of the MTSM measurement system, the model was simulated to represent an evaporation process of deionized (DI) water, and the experimental results of an evaporation process of DI water using the MTSM measurement system were compared. During the process, only thickness changes due to the thermal surface evaporation process of water molecules while other properties, such as density and viscosity, are unchanged. Graphs (a) and (b) in Figure 37 show the experimental results of the relative Δf and α of MTSM for the evaporation process of DI water and graphs (c) and (d) are the results of the simulation using equation (4) and (5). Both simulation and experiment show no stage **II** in this Newtonian case because stiffness is zero, and the viscosity and density are constants. This means that the overall response of MTSM sensor is governed by the changes in the thickness only. Stage **I** indicates the stabilized response of MTSM to water loading due to the relatively greater thickness of a water layer than the penetration depth of acoustic waves. The following stage **III** shows *Sauerbrey mass effect* when the thickness of a water layer becomes smaller than a

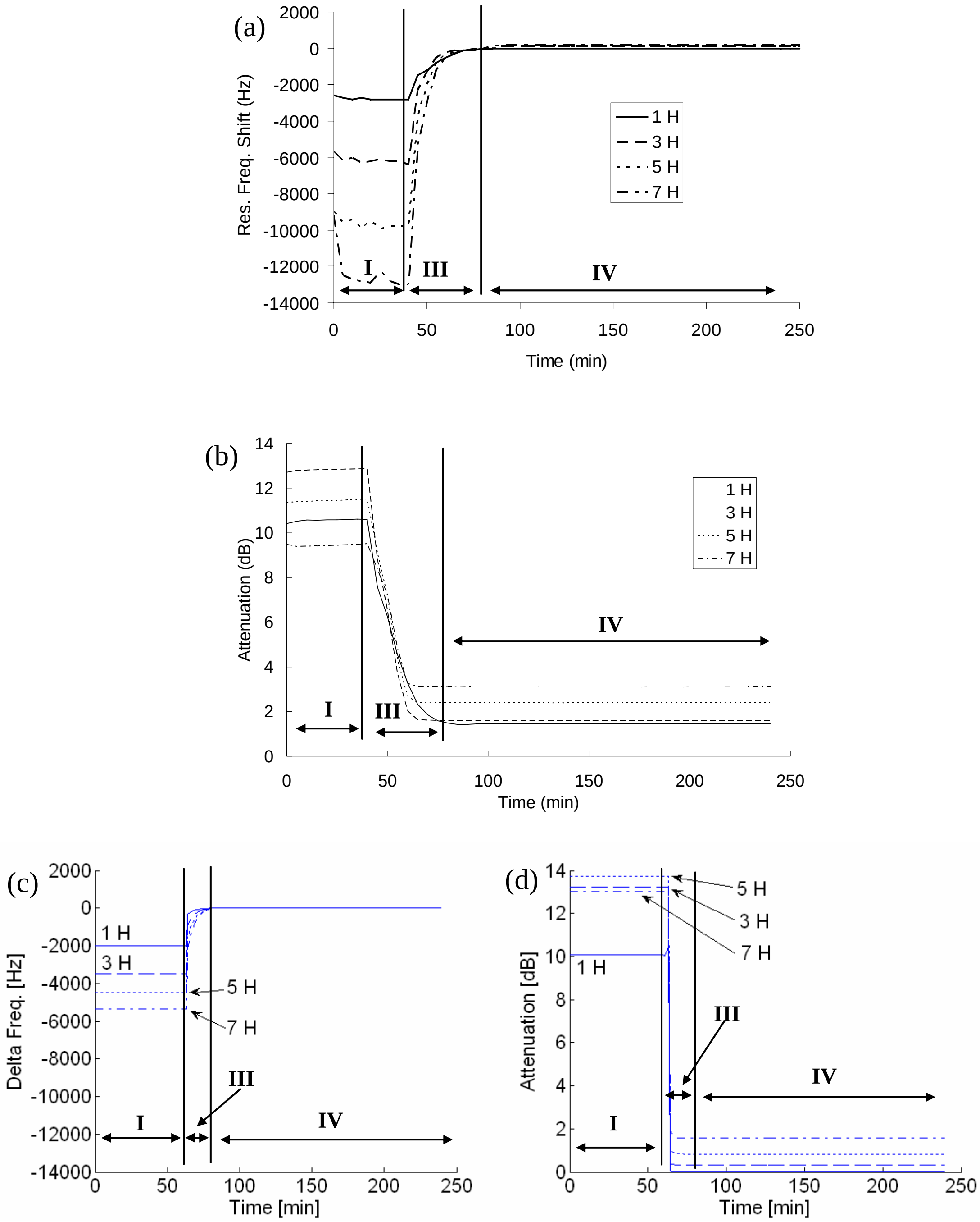

Figure 37. Validation of the system for an evaporation process of Newtonian liquid using mechanical properties of water. (a) and (b) Experimental results, and (c) and (d) simulation of the process.

penetration depth. The sudden decrease in the resonant frequency of MTSM reveals the sudden mass changes of a water layer caused by the evaporation of water.

There is a discrepancy in the magnitude of the relative Δf in graphs (a) and (c). The magnitudes of the experimental results are greater than the one of the simulation results. The first harmonic response of MTSM sensor to water loading with a semi-infinite thickness is approximately 2.1 *KHz* and the simulation also shows similar response for the first harmonic. However, as harmonic increases, the discrepancies between the experimental results and the simulation are increased. The experimental result of the seventh harmonic response (≈ 13 *kHz*) reaches up to 2 times of the simulation result (≈ 5.5 *kHz*). The discrepancies between experimental result and simulation are caused by the well-ordered water molecules on the surface of gold electrodes of MTSM sensor [41]. The mechanical properties, such as density and viscosity, of the well-ordered molecules of liquid are higher than those of bulk values. One may notice that the discrepancies are also increasing as the harmonics increase. Under water loads, the penetration depth of seventh harmonic acoustic shear waves is approximately 70 *nm* while one of first harmonic is about 180 *nm*. This clearly shows the difference in the mechanical properties of interfacial and bulk medium of Newtonian liquid.

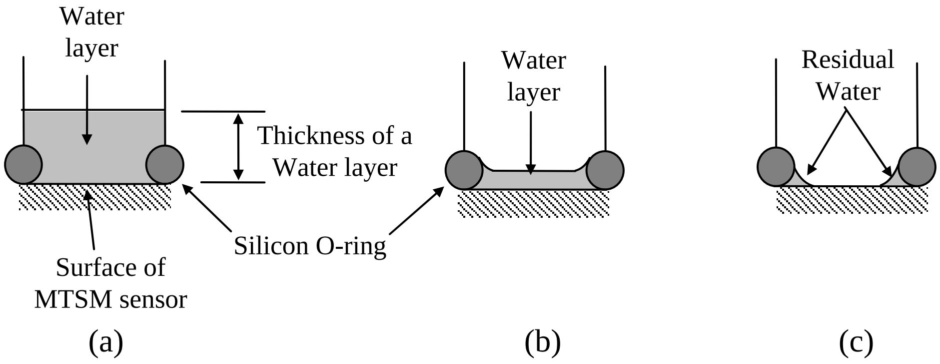

Figure 38. Changes in the shape of a water layer in the MTSM measurement system during an evaporation process. (a) Initial condition of a water layer inside of the MTSM measurement system, (b) When the thickness is less than the height of the O-ring, and (c) Final stage of a water that deforms to a ring type shape.

There is a different duration of stage III between the experiment and the simulation. The duration of the stage III of the experiments is approximately 40 minutes while one of the simulations is about 20 minutes. Basically this difference is caused by the different analysis and assumptions of the film thickness when the thickness is relatively small during the stage **III**. The simulation assumes the thickness of the water layer will be gradually decreasing and covering the whole area of the sensor during the entire evaporation process. However, the DI water layer on the MTSM sensor is not behaving like assumptions. Instead of the gradual decrease in the thickness of the water layer, the shape of the water layer changes from disk shape to ring shape by sudden collapsing of center area of the water layer and leaving open surface of MTSM sensor. Figure 38 depicts this ring phenomenon [81].

First, a water layer has a shape of disk with uniform thickness through the entire MTSM sensor surface (picture (a) in Figure 38). Then, the thickness of a water layer at the edge is higher than the center region because of the surface tension that interacting between water and the surface of the O-ring (picture (b) in Figure 38). Finally, as the thickness of the center region of the water layer become thinner, the ring phenomenon happens and leaves the center region of the MTSM sensor exposed to air (picture (c) in Figure 38). Because of this ring phenomenon, the air exposed surface area of residual water has been reduced from when water layer has a disk shape. This makes the evaporation rate of water to lower and the experimental results show this phenomenon by the longer duration of stage **III** than the simulation.

6.3 Experiment with biological samples (collagen and albumin)

Generally, collagen sample is prepared in liquid like phase and finally ends up with a thin rigid (polycrystalline) film under an evaporation-induced deposition process. Albumin is also prepared in liquid like phase and ends up with a thin amorphous (less rigid than collagen) film on the gold surface of the MTSM sensor. Therefore, it is important to know the kinetics of deposition process of biological sample as a function of time. The concentration of 50 μl of 1 *mg/ml* of acid soluble collagen and albumin samples, and a MTSM sensor with 10 *MHz* fundamental resonant frequency was used in the experiment. The kinetics and signatures of the evaporation-induced deposition process were monitored using the MTSM sensor measurement system (Figure 36).

6.3.1 Experimental results

For an evaporation-induced deposition process of the biological samples, collagen and albumin were chosen. Collagens are a family of highly characteristic fibrous proteins found in all multicellular animals. A typical collagen molecule has a long, stiff, triple-stranded helical structure, in which three collagen polypeptide chains, α chains, are wound around one another in a ropelike super-helix [10-13]. Albumins are the main protein in human blood and the key to the regulation of blood's osmotic pressure. Chemically, albumin is well known as a class of simple, water-soluble, and heat coagulable protein. Also, they can be found in many animal and plant tissues, especially egg white, blood plasma, serum, muscles, and milk [11, 12, 14, 15].

Graphs in Figure 39 and 40 show results of the changes in the relative resonant frequency (Δf) of the MTSM sensor during the evaporation-induced deposition process of collagen and albumin solution as a function of time. All graphs clearly show that there are four consecutive stages of the MTSM sensor response during the evaporation-induced deposition process of each sample. Loaded collagen or albumin samples are in a liquid phase with about 7.5 *mm* diameter and 1 *mm* in height on the MTSM sensor surface as an initial condition. The first stage (**I**) is indicated by either small or almost no changes in the relative Δf and α (between 0 ~ 50 minutes). The simulations also indicate the first stage by showing the stabilized response of MTSM through the thickness changes in the graphs of Figure 32 and 35. During the first stage (**I**), solvent evaporates through the open top surface; hence, the change in the thickness of the liquid medium is the main parameter that affects the response of the MTSM sensor. Meanwhile, the second stage is rather complex than the first stage.

The first part of the second stage (**II-1**) is indicated by sudden slight (about 1 ~ 2 dB) increase in attenuation and last short period of time (less than 5 minutes). The relative Δf of albumin sample shows oscillatory responses at higher (5^{th} and 7^{th}) harmonic and this can be analyzed as a point where the thickness of the film approaches a couple of penetration depths. The phase of the sample starts to transform from a Newtonian viscous liquid to viscoelastic (VE) condition during this stage because of the increase in the concentration of the solute. The mass fraction of free solution graphs in Figure 29 also indicate this region by sudden increase of mass fraction curve. Simulations also show this oscillatory response of MTSM sensor in both relative Δf and α depending on the material properties, and can be seen from graphs in Figure13, 14, 16 and 18.

The second part of the second stage (**II-2**) is shown by a sudden decrease in the relative Δf and α. It seems that the most of the liquid solvent is evaporated and only left with a gel type, soft rubber condition, viscoelastic thin film on the MTSM sensor surface. The changes in the shear modulus (increase in viscosity and stiffness) are the major driven factors causing the response of MTSM in this stage. Simulations show similar behavior in graphs in Figure 13 and 14, with decrease in relative Δf and α when the material property becomes more viscous and rigid.

The third stage (**III**) is indicated by small increase in relative Δf and decrease in the slope of α. During this stage, the main driven factors are again shear modulus with the slower rate of changes than the stage **II**. There is a slight decrease in the viscosity to reveal the hardening or gasifying process of the VE film material [63, 71]. Finally, the last stage (**IV**) is shown by a stabilized phase in both relative Δf and α.

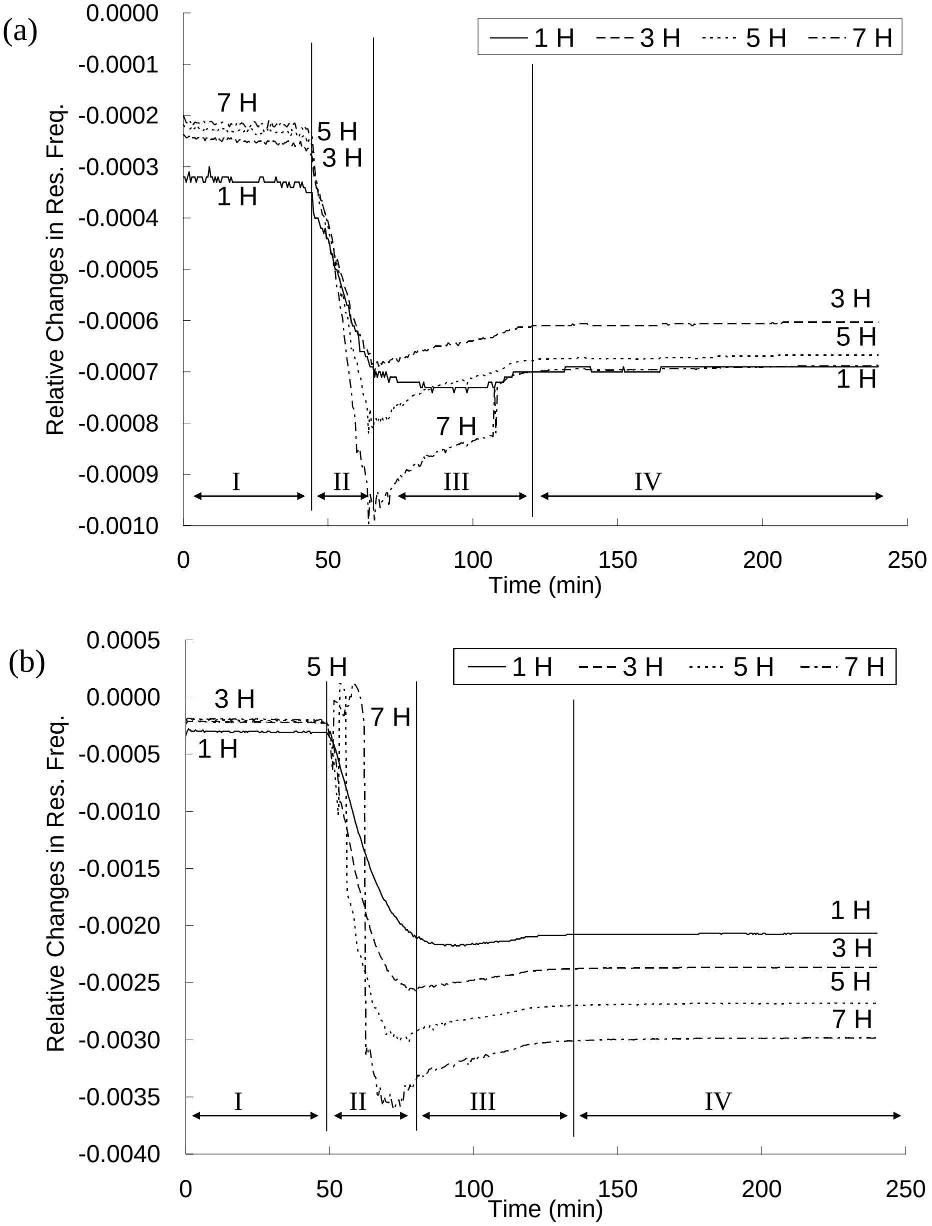

Figure 39. Relative changes (relative Δ*f*) in the harmonic resonant frequencies of the MTSM sensor with (a) collagen and (b) albumin samples as a function of time.

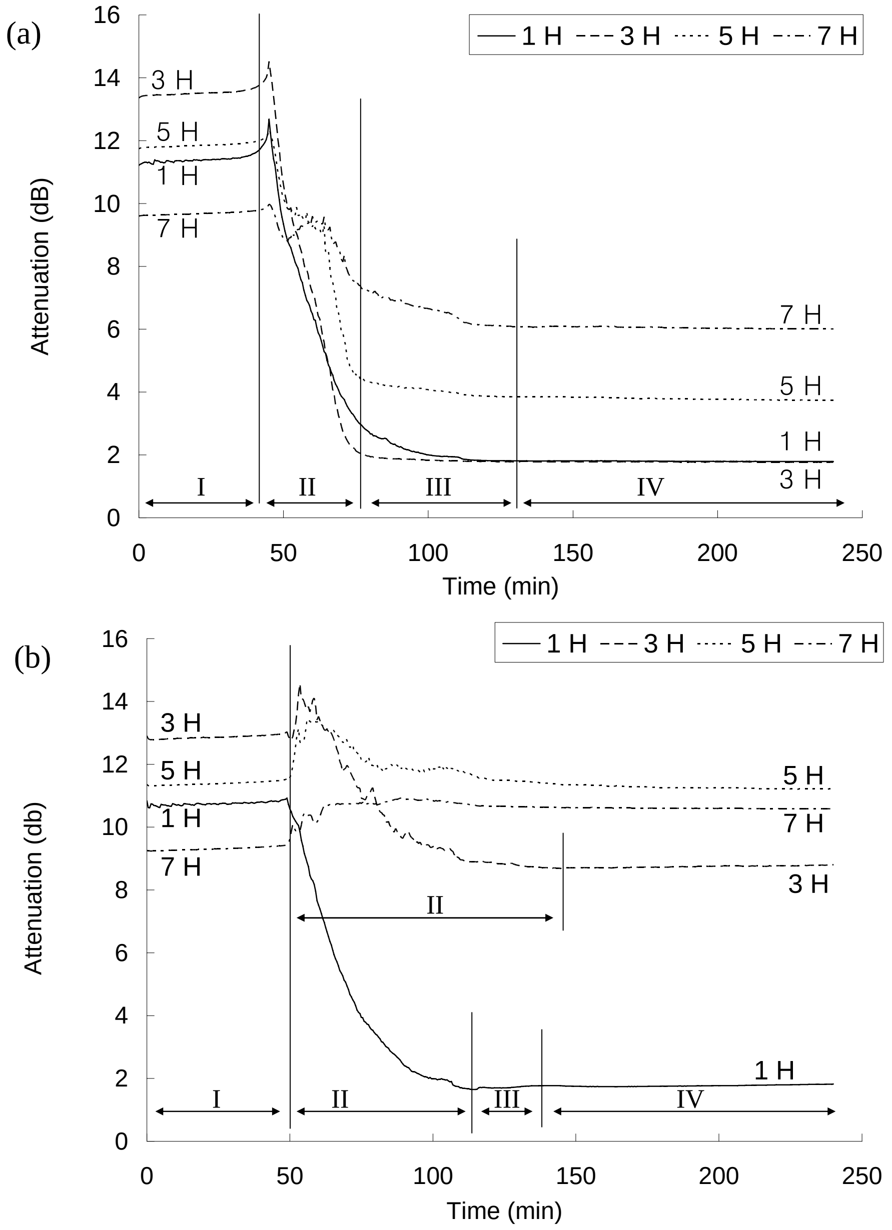

Figure 40. Attenuation (α) changes in the harmonic resonant frequencies of the MTSM with (a) collagen and (b) albumin samples as a function of time.

The different VE characteristics (or acoustic signatures) of each sample can be perceived by the comparison of the response of collagen and albumin cases (graphs in Figure 39 and 40). The characteristic of the relative Δf of each harmonic looks similar in both collagen and albumin, except the stage **II** of albumin case that shows oscillatory response (or *negative frequency shift*) [57] at higher (5th and 7th) harmonics. As the thickness of the albumin decreases and approaches to a couple of penetration depths (δ), the oscillatory response is initiated at higher harmonics (5th and 7th) due to the smaller penetration depth than one of the lower harmonics (1st and 3rd). The 1st and 3rd harmonics show a typical viscous loading effect with increase in the relative Δf and α as the viscosity increases. Simulation graphs (a), (c), (e), and (g) in Figure 14 show this typical viscous loading effect. In terms of the dynamic range of the relative Δf, albumin shows almost three to four times larger response than collagen. This reveals the strong viscous loading effect in albumin based on the hypothesis that the density of both sample are similar. The simulations in Figure 34 and 35 also show this bigger response of MTSM to albumin by giving faster and earlier increases in the viscosity of albumin than collagen.

Attenuation graphs in Figure 40 show more clear dissimilar characteristic between collagen and albumin samples. In collagen case, the attenuation of each harmonic at the stage **IV** becomes less than the initial values which means that the film behaves more rigidly. In other words, the stiffness of the collagen sample increases as a function of time through the whole thickness, but in albumin case, the attenuation of only 1st and 3rd harmonic responses decreased while one of 5th and 7th increased through the time. This indicates that the albumin film has a rather anisotropic amorphous mechanical characteristic through the film thickness and this can be detected by the different harmonic response of MTSM. Again, attenuation graphs in Figure 40 indicate that the collagen film is stiffer than the albumin film through the film thickness, because attenuations of each harmonic response of collagen are generally lower than the one of albumin case, except 1st harmonic. The attenuation response of collagen and albumin also indicate that the shear modulus of the outer most film is greater than the inner medium due to the higher concentration of solute at the outer surface during the evaporation process [68]. The duration of stage **II** of collagen is shorter than albumin in both relative Δf and α, and this indicates the solidification or crystallization process of collagen film initiates faster than albumin. Finally, from the results in Figure 40, one may infer that the major contribution of the response of MTSM sensor to collagen comes from the changes in the thickness and stiffness of the film while one of albumin comes from the changes in the thickness and viscosity during the deposition process.

For stage **III** and **IV**, generally, the experiments and the simulation show similar response of MTSM sensor to both collagen and albumin samples. The stage **III** of experiments can be explained by slight decrease in the viscosity and final maximum value of stiffness of both collagen and albumin [50]. The simulation results also show same result with similar changes in the viscosity and stiffness of the film and can be found in Figure 31, 32, 34, and 35.

In summary, the simulation shows similar response with the experimental results. Especially, the VE loading signatures of MTSM sensors are detected in both the simulations and the experiments with distinct stages. Meanwhile, there is a clear difference between the simulation and the experiments of the relative Δf at the stage **II**, **III**, and **IV**. In the simulation, the magnitude of 1st harmonic relative Δf at the stage **II** is biggest, 3rd harmonic is smaller than the 1st harmonic, 5th harmonic is smaller than the 3rd harmonic, and 7th harmonic is smallest. However, it is opposite in the experiments; the magnitude of 7th harmonic relative Δf at the stage **II** is greatest, 5th harmonic is smaller than 7th harmonic, 3rd is smaller than 5th, and finally 1st harmonic is smallest. For the simulation, the VE film is treated as a material that has uniform distribution of the mechanical properties. The mechanical properties of the VE film are fixed through the film thickness for the simulation. However, since the experiments show different response, first, this means that the mechanical properties of the films are not uniform through the film thickness. Second, the viscoelastic loading on the lower most part of the film is bigger than the upper most part of the film. This can be explained by the sedimentation of the coagulated or aggregated clusters of the collagen and albumin on the MTSM sensor surface. The MTSM sensor shows this phenomenon by indicating the bigger response at the higher harmonics than the lower harmonics. This clearly indicates the anisotropic, non-uniform distribution of mechanical properties of the biological VE thin films during the evaporation-induced deposition process.

6.3.2 Optical, AFM, and SEM analysis of collagen and albumin

Collagen and albumin samples were imaged by three method, such as optical, scanning electron microscopy (SEM), and atomic force microscopy (AFM) after the experiment. Tapping mode was used for imaging, and the diameter of the tip of AFM was 10 *nm*. Since there are difficulties of imaging the samples at the initial liquid status or during the evaporation process, only final thin films of both collagen and albumin samples were imaged using above three methods and are shown in Figure 41 and 42.

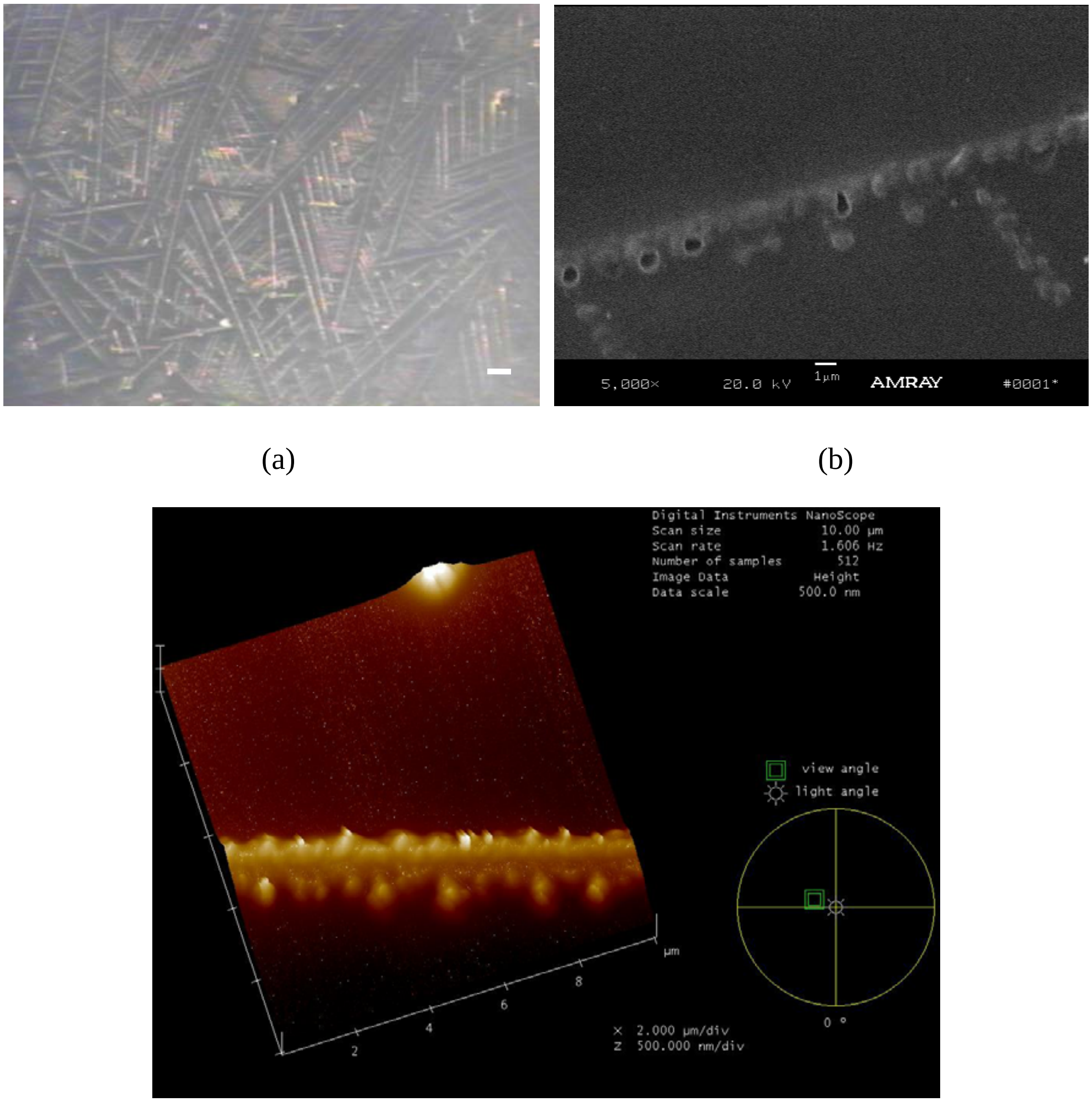

(a) (b)

(c)

Figure 41. Images of crystallized collagen sample after 4 hours of deposition process: (a) optical (marker indicates 100 μm), (b) SEM, and (c) AFM images.

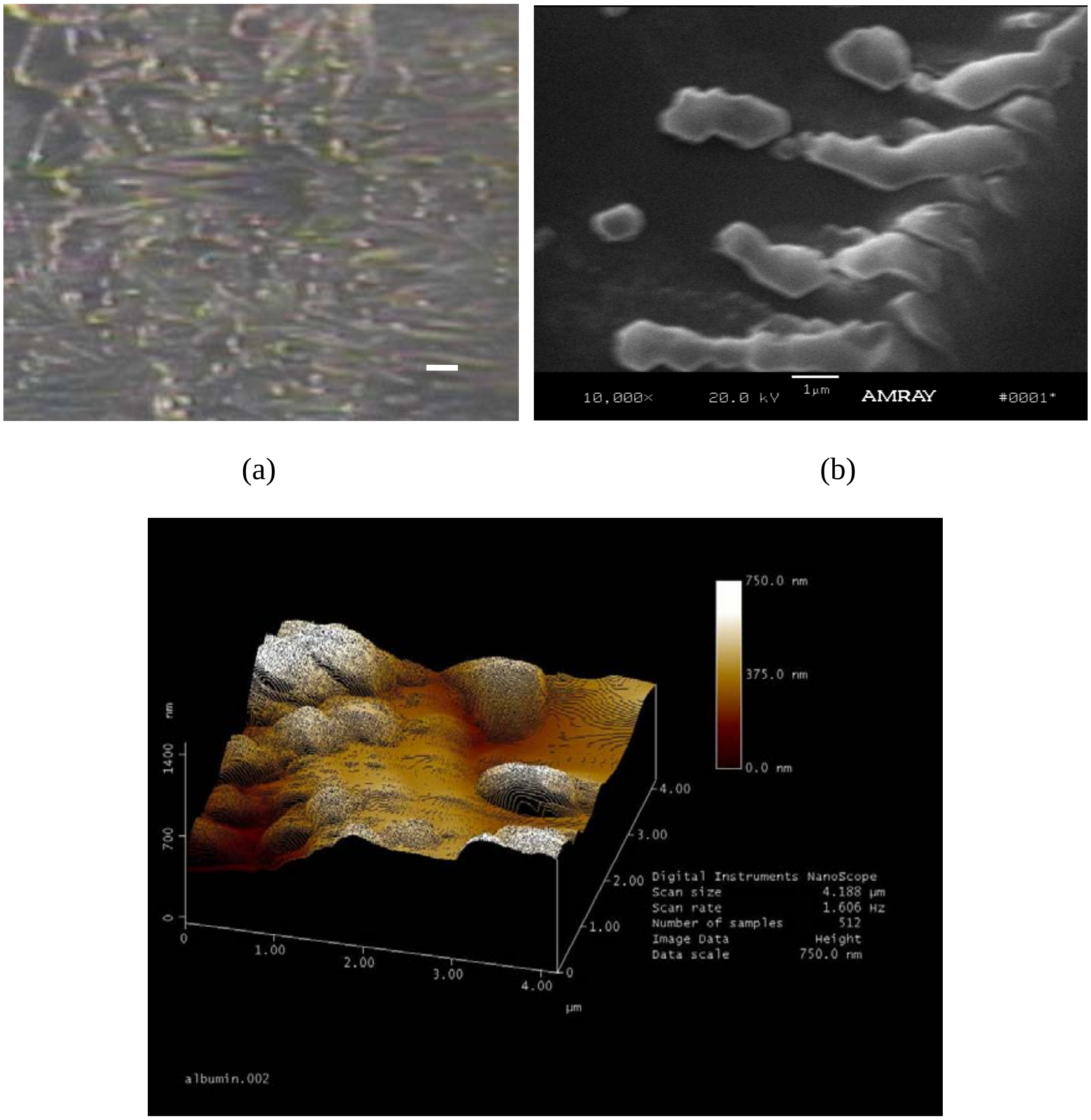

(a) (b)

(c)

Figure 42. Images of crystallized albumin sample after 4 hours of deposition process: (a) optical (marker indicates 50 μm), (b) SEM, and (c) AFM images.

The condition of the surface of collagen thin film is filled with thin rode types of crystalline structures of collagen fibrils while one of albumin thin film is filled with coagulated amorphous structures of albumin. The uneven and bumpy level of the surface of albumin thin film is larger than the one of collagen thin film, and this can be found from the images of SEM and AFM in Figure 41 and 42.

7 SUMMARY AND CONCLUSIONS

It has been successfully studied and demonstrated a MTSM technology as a sensitive tool to analyze the interactions with a viscous, viscoelastic, or elastic layer. After Sauerbrey derived the equation that provides the linear relationship between the mass on the TSM sensor and the resonant frequency shift, there have been many progresses. Among many achievements, Kanazawa equation, showing the relationship between the resonant frequency shift and the product of density and viscosity of Newtonian liquid, has been believed as an important contribution. Since late 1980's, many scientists have shown the interest of utilization of TSM sensor technology to the viscoelastic materials as a next step. Due to the shear sensitivity of TSM sensors, there has been much research about studying biological interfaces and polymerization process because of the material's complex physical viscoelastic characteristics, and still progressing [82, 83].

7.1 Summary

A model of a MTSM sensor with a viscoelastic medium has been studied and simulated at multiharmonic frequencies from the fundamental up to the 7th harmonic.

Modeling of the system is established based on an existing continuum electromechanical model of an AT-cut TSM sensor, and this has been described in section 5.1. Effect and importance of three mechanical (viscosity, elastic stiffness, and density) and a geometrical (thickness) properties of VE medium to the overall responses (relative Δf and α) of MTSM sensors were simulated and analyzed, and these effects can be found in sections 5.4. All the variables (viscosity, elastic stiffness, density, and thickness) were varied in reasonable ranges based on the literatures for the simulations. The thickness varied from 1 *mm* to 100 *nm* while viscosity, elastic stiffness, and density were fixed at 0.001 *kg/ms*, 0 N/m^2, and 1000 kg/m^3 to simulate a Newtonian liquid like behavior of VE medium (stage **I** in Figure 5). The viscosity and thickness were varied between 0.001 to 0.1 *kg/ms* and 10^{-5} to 10^{-7} *m* while elastic stiffness and density were fixed at 10^5 N/m^2 and 1000 kg/m^3 to simulate the transition of the VE medium from a liquid like to a soft rubber conditions (stage **II** in Figure 5). For a hard rubber and a solid like behaviors of VE medium (stage **III** and **IV** in Figure 5), the elastic stiffness and thickness were varied between 10^6 to 10^8 $\mathrm{N/m^2}$ and 10^{-5} to 10^{-7} *m*, respectively, while viscosity and density were fixed at 0.1 *kg/ms* and 1000 kg/m^3. Due to the smaller range of variations of density of VE medium, the density was fixed for the entire simulations.

For the signature study of VE medium, the response of MTSM sensor to shear modulus has been carefully analyzed by taking different hypothetical paths on the mesh graph, and it can be found in section 5.4.6. Different path means that the different contribution of shear modulus during the process, and Figure 22 shows the concept of the different path.

For the verification process of the model system of MTSM sensor with a VE medium, a prototype of MTSM measurement system has been developed to monitor and analyze the evaporation-induced deposition process of biological samples (collagen and albumin). Chapter 6 describes the experimental analysis of the system. Whole evaporation-induced deposition process of collagen and albumin samples were monitored by use of MTSM measurement system.

7.2 Conclusions

First, this study provides the beneficial features of the multiharmonic frequency responses of a MTSM sensor. Most of the research in TSM sensor technology had been involving only the changes in the fundamental frequency of the TSM sensor. Due to the manufacturing limitations on TSM sensors, the operating fundamental frequency range hardly reaches more than 1 *GHz* and typically varies between 3 *MHz* up to 1 *GHz* [84].

Higher fundamental frequency means that the thinner the thickness of the sensor. For example, the thickness of 10 *MHz* and 25 *MHz* TSM sensors are approximately 167 μm and 67 μm. As a practical point of view, a TSM sensor with a fundamental frequency higher than 100 *MHz* is difficult to fabricate as a physical sensor because of the fragileness. However, this can be overcome by implementing the multiharmonic resonant frequency concept. With 10 *MHz* TSM sensors, it is easy to achieve up to 50 *MHz* by exciting the TSM sensor in its fifth harmonic mode. A TSM sensor with 375 *MHz* resonant frequency can be obtained by exciting a 75 *MHz* fundamental resonant frequency TSM sensor in its fifth harmonic mode. Therefore, the nano range superficial medium can be easily analyzed by this multiharmonic resonant frequency concept, and the utilization of multiharmonic concept provides a "*virtually slicing*" technology that examines the medium at the different distances from the sensor surface based on the harmonic frequencies. From the experimental results of collagen and albumin case studies, the responses from the different harmonic frequency clearly show the different characteristics of mechanical properties, especially shear modulus, of the sample. Both collagen and albumin film show more rigid characteristic at lower harmonic while indicating smaller shear modulus at the higher harmonics, such as 5th and 7th harmonics.

Second, importance of depth of penetration of the acoustic shear waves in the medium has been emphasized by studying the relationship between the thickness of the medium and the depth of penetration. Every simulation result showed a similar trend of the relative Δf and α responses of MTSM as the thickness decreases; stabilization → oscillations → *Sauerbrey Mass Effect*. When the thickness of the VE medium is much greater than the penetration depth of the acoustic shear waves, both Δf and α show saturations with no changes through the thickness. As the thickness of the VE medium reaches a couple of penetration depth, all the cases show the oscillations in both relative Δf and α. Finally, when the thickness of VE medium becomes much smaller than a penetration depth, regardless of the mechanical properties, all the cases show *Sauerbrey Mass Effect*. Therefore, the relationship between the thickness (h) of the VE medium and the penetration depth (δ) is critical to analyze the response of MTSM sensor. Since the penetration depth of acoustic waves in the VE medium is also a function of mechanical properties of VE medium, it is helpful to know the condition of the VE medium; whether it is close to a Newtonian viscous liquid or close to a solid elastic material. For example, if the sample is in a Newtonian viscous liquid like phase with the thickness larger than 10 μm (when $h >> \delta$), then the relative Δf and α responses of MTSM will be stabilized all the time and they are function of only mechanical properties (density, viscosity, and stiffness) of the VE medium. For the cases when the thickness of VE medium becomes a couple of penetration depth or smaller (when $h \approx \delta$), then the Δf and α responses of MTSM will be complicated due to the combinational contributions of mechanical and geometrical factors. When the VE medium reacts as an additional resonance system due to the mechanical properties, the negative frequency shift will occur and unusual oscillatory response of MTSM sensor will be detected. Obviously, when the thickness of VE medium is much smaller than the penetration depth (when $h << \delta$), MTSM sensor shows a typical *Sauerbrey Mass Effect*.

Third, acoustic signature of the MTSM sensor response in terms of the effect of each mechanical properties of the medium has been analyzed. In addition, the library of acoustic signatures has been established. The effect of each mechanical properties of the medium has been studied by the simulation approach. As already mentioned above, the most important parameter is the relationship between the thickness of the film and the penetration depth of acoustic shear waves in the film through the entire process. The viscous characteristic of the film affects more to the overall response of MTSM sensor when the film is in rather viscous conditions. In other words, slight changes in the viscosity provide more effect than the similar changes in the stiffness characteristic of the film. However, as the film becomes more rigid condition, the effect from the elastic stiffness shows more impact than the effect from the viscosity changes. Since the density is directly connected to the physical mass of the film, the effect of the changes in density is simply showing the typical mass behavior of the MTSM sensor response.

Fourth, the evaporation-induced deposition process of collagen and albumin solution has been examined using the MTSM measurement system, and the experimental results and the simulations also have been compared. Basically, the experimental results were similar with the simulations for the whole process by showing the more rigidity of collagen film with smaller changes in the relative Δf and attenuation of collagen than those of albumin. Due to the higher viscous loadings of albumin sample, the changes in the stage II of albumin is greater than the one of collagen. The simulation with two different hypothetic changes of each variable of collagen and albumin also shows good agreement with the experimental result. In addition, since there is a clear difference of the magnitudes of the relative Δf of each harmonics between the simulation and the experiment at the stage **II**, **III**, and **IV**, the study shows the clear evidence of anisotropic, non-homogeneous distributions of mechanical properties through the film thickness using MTSM sensors.

7.3 Future work

Among many future works, the author would like to emphasis three major future works.

First, there are only two case studies, such as collagen and albumin, which represent the different characteristics of VE medium in this thesis. However, more samples that represent different VE characteristics should be investigated with the model. The characterization of the well-known polymers with controllable and programmable mechanical properties using MTSM measurement technology can be best candidate for the more profound approach.

Second, the acoustic signatures of the VE medium that varies its mechanical properties from viscous to rigid conditions have been analyzed. However, in-depth and focused study of the response of MTSM sensor to smaller range of mechanical variation, such as only in stage **II** or **III**, should be considered.

Third, exact values of mechanical properties of non-homogeneous, anisotropic collagen and albumin samples were not able to be defined due to the complexity of the non-linear simultaneous equations of the model. This can be identified by the aid of dedicated computer software.

8 REFERENCES

[1] J. Rickert, A. Brecht and W. Gopel, "Quartz crystal microbalances for quantitative biosensing and characterizing protein multilayers," Biosens.Bioelectron., vol. 12, pp. 567-575, 1997.

[2] J. Rickert, T. Weiss, W. Kraas, G. Jung and W. Göpel, "A new affinity biosensor: self-assembled thiols as selective monolayer coatings of quartz crystal microbalances," Biosensors & Bioelectronics, vol. 11, pp. 591-598, 1996.

[3] H. Muramatsu, E. Tamiya, M. Suzuki and I. Karube, "Viscosity monitoring with a piezoelectric quartz crystal and its application to determination of endotoxin by gelation of limulus amebocyte lysate," Analytica Chimica Acta, vol. 215, pp. 91-98, 1988.

[4] H. Muramatsu, J.M. Dicks, E. Tamiya and I. Karube, "Piezoelectric crystal biosensor modified with protein A for determination of immunoglobulins," Anal.Chem., vol. 59, pp. 2760-2763, Dec 1. 1987.

[5] O. Wolff, E. Seydel and D. Johannsmann, "Viscoelastic properties of thin films studied with quartz crystal resonators," Faraday Discussions of the Chemical Society, vol. 107, pp. 91-104, 1997.

[6] B.A. Cavic, F.L. Chu, L.M. Furtado, S. Ghafouri, G.L. Hayward, D.P. Mack, M.E. McGovern, H. Su and M. Thompson, "Acoustic waves and the real-time study of biochemical macromolecules at the liquid/solid interface," Faraday Discuss., vol. (107), pp. 159-176, 1997.

[7] R. Zhou, A. Menon and F. Josse, "A chemical sensor with improved selectivity using a modified-electrode QCR," IEEE International Frequency Control Symposium, pp. 56-63, 1997.

[8] R.J. Heaton, A.W. Peterson and R.M. Geogiadis, "Electrostatic surface plasmon resonance: Direct electric field-induced hybridization and denaturation in monolayer nucleic acid films and label-free discrimination of base mismatches," PNAS, vol. 98, pp. 3701-3704, 2001.

[9] N.L. Thompson, T.P. Burghardt and D. Axelrod, "Measuring surface dynamics of biomolecules by total internal reflection fluorescence with photobleaching recovery or correlation spectroscopy," Biophysical Journal, vol. 33, pp. 435-454, 1981.

[10] D.J. Prockop and A. Fertala, "The collagen fibril: the almost crystalline structure," J.Struct.Biol., vol. 122, pp. 111-118, 1998.

[11] H. Lodish, M.P. Scott, P. Matsudaira, J. Darnell, L. Zipursky, C.A. Kaiser, A. Berk and M. Krieger, Molecular cell bioloby, W. H. Freeman, 2000, .

[12] B. Albert, D. Bray, J. Lewis, M. Raff, K. Roberts and J.D. Watson, Molecular Biology of the Cell, Garland, 1983, .

[13] E. Adachi, O. Katsumata, S. Yamashina, D.J. Prockop and A. Fertala, "Collagen II containing a Cys substitution for Arg-alpha1-519. Analysis by atomic force microscopy demonstrates that mutated monomers alter the topography of the surface of collagen II fibrils," Matrix Biol., vol. 18, pp. 189-196, Apr. 1999.

[14] U. Kragh-Hansen, D. Donaldson and P.H. Jensen, "The glycan structure of albumin Redhill, a glycosylated variant of human serum albumin," Biochim.Biophys.Acta, vol. 1550, pp. 20-26, Nov 26. 2001.

[15] M.C. Martins, C. Fonseca, M.A. Barbosa and B.D. Ratner, "Albumin adsorption on alkanethiols self-assembled monolayers on gold electrodes studied by chronopotentiometry," Biomaterials, vol. 24, pp. 3697-3706, Sep. 2003.

[16] A. Menon, R. Zhou and F. Josse, "Coated-Quartz crystal resonator (QCR) sensors for on-line detection of organic contaminants in water," IEEE Trans. on UFFC, vol. 45, pp. 1416, 1998.

[17] P. Wittung-Stafshede, M. Rodahl, B. Kasemo, P. Nielsen and B. Norden, "Detection of point mutations in DNA by PNA-based quartz-crystal biosensor," Colloids and Surfaces A: Physicochemical and Engineering Aspects, vol. 174, pp. 269, 2000.

[18] F.J. Alenghat, B. Fabry, K.Y. Tsai, W.H. Goldmann and D.E. Ingber, "Analysis of cell mechanics in single vinculin-deficient cells using a magnetic tweezer," Biochemical and Biophysical Research Communications, vol. 277, pp. 93-99, 2000.

[19] M. Muratsugu, F. Ohta, Y. Miya, T. Hosokawa, S. Kurosawa, N. Kamo and H. Ikeda, "Quartz crystal microbalance for the detection of microgram quantities of human serum albumin: relationship between the frequency change and the mass of protein adsorbed," Anal. Chem., vol. 65, pp. 2933-2937, Oct 15. 1993.

[20] H. Su, P. Williams and M. Thompson, "Platinum anticancer drug binding to DNA detected by thickness-shear-mode acoustic wave sensor," Anal.Chem., vol. 67, pp. 1010-1013, Mar 1. 1995.

[21] D.A. Buttry and M.D. Ward, "Measurement of interfacial processes at electrode surfaces with the electrochemical quartz crystal microbalance," Chemical Reviews, vol. 92, pp. 1355-1379, 1992.

[22] B.S. Ballantine, R.M. White, S.J. Martine, A.J. Ricco, E.T. Zellers, G.C. Frye and H. Wohltjen, "Acoustic wave sensors - Theory, design, and physico-chemical applications," Academic Press, 1997, pp. Ch 3.

[23] G.L. Cote, R.M. Lec and M.V. Pishko, "Emerging biomedical sensing technologies and their applications," IEEE Sensor Journal, vol. 3, pp. 251-266, 2003.

[24] R.M. Lec, "Piezoelectric biosensors: recent advances and applications," Proceedings of the 2001 IEEE International Frequency Control Symposium and PDA Exhibition, pp. 419 - 429, 2001.

[25] NanoBiosensor Research Laboratory, School of Biomedical Engineering Science and Health Systems, Drexel University, "Internal research report," 2005.

[26] S. Kolliopoulou, D. Tsoukalas, P. Dimitrakis, P. Normand, S. Paul, C. Pearson, A. Molloy and M.C. Petty, "Field effect devices with metal nanoparticles integrated by Langmuir-Blodgett technique for non-volatile memory applications," Journal of Physics: Conference Series, vol. 10, pp. 57-60, 2005.

[27] A. Balamurugan, S. Kannan and S. Rajeswari, "Bioactive Sol-Gel hydroxyapatite surface for biomedical applications - in vitro study," Trends Biomater. Artif. Organs., vol. 16, pp. 18-20, 2002.

[28] M. Hecq and J. Leleux, "Spectrometry of X-ray induced emission in sputtering deposition: a new technique for in situ thin-film chemical analysis," Anal. Chem., vol. 59, pp. 440-443, 1987.

[29] A. Gotoh and F. Ikasaki, "Applicability of evaporation technique for the preparation of dispersed nano-sized ultrafine particles at atmospheric pressure," Journal of Materials Science Letters, vol. 15, pp. 881-882, 2004.

[30] A. Timoumi, H. Bouzouita, M. Kanzari and B. Rezig, "Temperature effect on the growth of In_2S_3 by thermal evaporation technique," Eur. Phys. J. Appl. Phys., vol. 33, pp. 77-81, 2006.

[31] W. Han and S.M. Lindsay, "Probing molecular ordering at a liquid-solid interface with a magnetically oscillated atomic force microscope," Applied Physics Letters, vol. 72, pp. 1656-1658, 1998.

[32] E. Ostuni, L. Yan and G.M. Whitesides, "The interaction of proteins and cells with self-assembled monolayers of alkanethiolates on gold and silver," Colloids and Surfaces B: Biointerfaces, vol. 15, pp. 3-30, 1999.

[33] A. Ikai, R. Afrin, A. Itoh, H.C. Thogersen, Y. Hayashi and T. Osada, "Force measurements for membrane protein manipulation," Colloids and Surfaces B: Biointerfaces, vol. 23, pp. 165-171, 2002.

[34] K. Ito, K. Hashimoto and Y. Ishimori, "Quantitative analysis for solid-phase hybridization reaction and binding reaction of DNA binder to hybrids using a quartz crystal microbalance," Analytica Chimica Acta, vol. 327, pp. 29-35, 1996.

[35] F. Josse, Z.A. Shana, D.E. Radtke and D.T. Haworth, "Analysis of piezoelectric bulk-acoustic-wave resonators as detectors in viscous conductive liquids," IEEE Transactions on Ultrasonics, Ferroelectrics, and Frequency Control, vol. 37, pp. 359-368, 1990.

[36] E. Benes, M. Groschl, F. Seifert and A. Pohl, "Comparison between BAW and SAW sensor principles," IEEE Transactions on Ultrasonics, Ferroelectrics, and Frequency Control, vol. 45, pp. 1314-1330, 1998.

[37] S.J. Martin and G.C. Frye, "Polymer film characterization using quartz resonators," IEEE Ultrasonics Symposium, pp. 393-398, 1991.

[38] H.L. Bandey, R.A. Hillman, M.J. Brown and S.J. Martin, "Viscoelastic characterization of electroactive polymer films at the electrode solution interface," Faraday Discussions of the Chemical Society, vol. 107, pp. 105-121, 1997.

[39] C.E. Reed, K.K. Kanazawa and J.H. Kaufman, "Physical description of a viscoelastically loaded AT-cut quartz resonator," Journal of Applied Physics, vol. 68, pp. 1993, 1990.

[40] K.K. Kanazawa and J.G. Gorden, "Frequency of a quartz microbalance in contact with liquid," Anal. Chem., vol. 57, pp. 1770, 1985.

[41] S.J. Martin, G.C. Frye, A.J. Ricco and S.D. Senturia, "Effect of surface roughness on the response of thickness-shear mode resonators in liquid," Anal. Chem., vol. 65, pp. 2910-2922, 1993.

[42] R.W. Cernosek, S.J. Martin, R.A. Hillman and H.L. Bandey, "Comparison of lumped-element and transmission-line models for thickness-shear-mode quartz resonator sensors," IEEE Transactions on Ultrasonics, Ferroelectrics, and Frequency Control, vol. 45, pp. 1399-1407, 1998.

[43] B. Zimmermann, R. Lucklum, P. Hauptmann, J. Rabe and S. Buttgenbach, "Electrical characterization of high-frequency thickness-shear-mode resonators by impedance analysis," Sensors and Actuators B: Chemical, vol. 76, pp. 47-57, 2001.

[44] C. Behling, R. Lucklum and P. Hauptmann, "Direct method for shear moduli calculation from quartz crystal resonator measurements," Proceedings of the 1998 IEEE International Frequency Control Symposium., pp. 823 - 830, 1998.

[45] R. Lucklum, C. Behling and P. Hauptmann, "Gravimetric and non-gravimetric chemical quartz crystal resonators," Sensors and Actuators B: Chemical, vol. 65, pp. 277-283, 2000.

[46] M.I. Ivanchenko, H. Kobayashi, E.A. Kulik and N.B. Dobrova, "Studies on polymer solutions, gels and grafted layers using the quartz crystal microbalance technique," Analytica Chimica Acta, vol. 314, pp. 23-31, 1995.

[47] E. Nwankwo and C.J. Durning, "Impedance analysis of thickness-shear mode quartz crystal resonators in contact with linear viscoelastic media," Review of Scientific Instruments, vol. 69, pp. 2375-2384, 1998.

[48] A. Domack and D. Johannsmann, "Plastification during sorption of polymeric thin films: A quartz resonator study," Journal of Applied Physics, vol. 80, pp. 2599-2604, 1996.

[49] R. Lucklum and P. Hauptmann, "The quartz crystal microbalance: mass sensitivity, viscoelasticity and acoustic amplification," Sensors and Actuators B: Chemical, vol. 70, pp. 30-36, 2000.

[50] R. Lucklum and P. Hauptmann, "Determination of polymer shear modulus with quartz crystal resonators," Faraday Discuss, vol. 107, pp. 123, 1997.

[51] F. Ferrante, A.L. Kipling and M. Thompson, "Molecular slip at the solid-liquid interface of an acoustic-wave sensor," Jouranl of Applied Physics, vol. 76, pp. 3448, 1994.

[52] van den Doel, L.R., I.T. Young and L.J. van Vliet, "Monitoring the evaporation process of liquid samples in sub-nanoliter vials," ASCI'99, Proc. 5th Annual Conference of the Advanced School for Computing and Imaging, pp. 58-64, 1999.

[53] Q. Liao, L. Chen, X. Qu and X. Jin, "Brownian Dynamics Simulation of Film Formation of Mixed Polymer Latex in the Water Evaporation Stage," J.Colloid Interface Sci., vol. 227, pp. 84-94, Jul 1. 2000.

[54] J.L. Baldwin and B.A. Dempsey, "Effects of Brownian motion and structured water on aggregation of charged particles," Colloids and Surfaces A: Physicochemical and Engineering Aspects, vol. 177, pp. 111-122, 2001.

[55] B.R. Munson, D.F. Young and T.H. Okiishi, Fundamentals of fluid mechanics, New York: John Wiley, 1998, pp. 877.

[56] C.Y. Tai and C. Cheng, "Effect of CO_2 on Expansion and Supersaturation of Saturated Solutions," AIChE Journal, vol. 44, pp. 989-992, 1998.

[57] R. Lucklum and P. Hauptmann, "The D*f*-D*R* QCM technique: an approach to an advanced sensor signal interpretation," Electrochimica Acta, vol. 45, pp. 3907, 2000.

[58] J.M. Garcia-Ruiz, M.L. Novella and F. Otalora, "Supersaturation patterns in counter-diffusion crystallisation methods followed by Mach-Zehnder interferometry," Journal of Crystal Growth, vol. 196, pp. 703-710, 1999.

[59] M. Negahban, "Thermodynamic modeling of the thermomechanical effects of polymer crystallization: a general theoretical structure," International Journal of Engineering Science, vol. 35, pp. 277-298, 1997.

[60] C. Behling, R. Lucklum and P. Hauptmann, "The non-gravimetric quartz crystal resonator response and its application for determination of polymer shear modulus," Measurement Science and Technology, vol. 9, pp. 1886-1893, 1998.

[61] H. Su and M. Thompson, "Kinetics of interfacial nucleic acid hybridization studied by acoustic network analysis," Biosensors & Bioelectronics, vol. 10, pp. 329-340, 1995.

[62] R. Lucklum, C. Behling, R.W. Cernosek and S.J. Martin, "Determination of complex shear modulus with thickness shear mode resonators," J. Phys. D: Appl. Phys., vol. 30, pp. 346, 1997.

[63] R. Lucklum, C. Behling and P. Hauptmann, "Role of mass accumulation and viscoelastic film properties for the response of acoustic-wave-based chemical sensors," Anal. Chem., vol. 71, pp. 2488-2496, 1999.

[64] A. Hernandez-Jimenez, J. Hernandez-Santiago, A. Macias-Garcıa and J. Sanchez-Gonzalez, "Relaxation modulus in PMMA and PTFE fitting by fractional Maxwell model," Polymer Testing, vol. 21, pp. 325-331, 2002.

[65] W.H. King, "Piezoelectric sorption detector," Anal. Chem., pp. 1735-1739, 1964.

[66] M.D. Ward and D.A. Buttry, "In Situ Interfacial Mass Detection with Piezoelectric Transducers:" Science, vol. 249, pp. 1000-1007, 1990.

[67] A.P.M. Glassford, "Response of a quartz crystal microbalance to a liquid deposit," J. Vac. Sci. Technol., vol. 15, pp. 1836, 1978.

[68] M. Quintas, T.R.S. Brandao, C.L.M. Silva and R.L. Cunha, "Rheology of supersaturated sucrose solutions," Journal of Food Engineering, vol. 77, pp. 844-852, 2006.

[69] G. Liu and N.A. Amro, "Positioning protein molecules on surfaces: A nanoengineering approach to supramolecular chemistry," PNAS, vol. 99, pp. 5165-5170, 2002.

[70] A. Rave, Principles of Polymer chemistry, Springer, 2000, pp. 640.

[71] H.L. Bandey, R.W. Cernosek, Lee III, W. E. and L.E. Ondrovic, "Blood rheological characterization using the thickness-shear mode resonator," Biosensors & Bioelectronics, vol. 19, pp. 1657-1665, 2004.

[72] Y.H. An and K.L. Martin, Handbook of histology methods for bone and cartilage, Human Press, 2003, pp. Ch. 4.

[73] F.H. Silver, G. Bradica and A. Tria, "Elastic energy storage in human articular cartilage: estimation of the elastic modulus for type II collagen and changes associated with osteoarthritis," Matrix Biology, vol. 21, pp. 129-37, 2002.

[74] P. Lacolley, C. Labat, A. Pujol, C. Delcayre, A. Benetos and M. Safar, "Increased carotid wall elastic modulus and fibronectin in aldosterone-salt-treated rats: effects of eplerenone," Circulation, vol. 106, pp. 2848-53, 2002.

[75]http://www.rcsb.org/pdb/static.do?p=education_discussion/molecule_of_the_month/ pdb4_1.html, .

[76] R. Stoop, P. Buma, van der Kraan, P.M., A.P. Hollander, R.C. Billinghurst, T.H. Meijers, A.R. Poole and van den Berg, W.B., "Type II collagen degradation in articular cartilage fibrillation after anterior cruciate ligament transaction in rats," Osteoarthritis Cartilage, vol. 9, pp. 308-15, 2001.

[77] A. Despopoulos and S. Silbernagl, Color Atlas of Physiology, New York: Thieme, 1981, .

[78] G.J. Brownsey, T.R. Noel, R. Parker and S.G. Ring, "The Glass Transition Behavior of the Globular Protein Bovine Serum Albumin," Biophysical Journal, vol. 85, pp. 3943-3950, 2003.

[79] S. Mukta, H. Jeungphill and Z. Giovanni, "Plastic deformation of protein monolayers," Biophysical Journal, vol. 83, pp. 2211-2218, 2002.

[80] http://160.114.99.91/astrojan/protein/pictures/albumin.gif, .

[81] R.D. Deegan, O. Bakajin, T.F. Dupont, G. Huber, S.R. Nagel and T.A. Witten, "Capillary flow as the cause of ring stains from dried liquid drops," Nature, vol. 389, pp. 827-829, 1997.

[82] G.C. Komplin, F. Schleifer and W.J. Pietro, "A high-stability quartz crystal microbalance electrode for simultaneous solution-phase electrochemistry/microgravitometry," Rev. Sci. Instrum., vol. 64, pp. 1530-1535, 1993.

[83] S.J. Kwoun, R.M. Lec, B. Han and F.K. Ko, "A novel polymer nanofiber interface for chemical sensor applications," IEEE International Frequency Control Symposium, pp. 52-57, 2000.

[84] R. Behrends and U. Kaatze, "A high frequency shear wave impedance spectrometer for low viscosity liquids," Measurement Science and Technology, vol. 12, pp. 519-524, 2001.

9 APPENDIX

The continuum electromechanical model of a MTSM sensor under different ambient conditions is derived in this section. First, unperturbed MTSM sensor is considered. Then Sauerbrey case, MTSM sensor with rigid medium, is derived followed by Kanazawa case, MTSM with a semi-infinite Newtonian liquid. Finally, viscoelastic (VE) case is derived.

9.1 Unloaded MTSM sensor

In Figure 38, u_0^+ indicates wave traveling positive direction (upper direction) and u_0^- indicates wave traveling negative direction (downward direction) in TSM sensor.

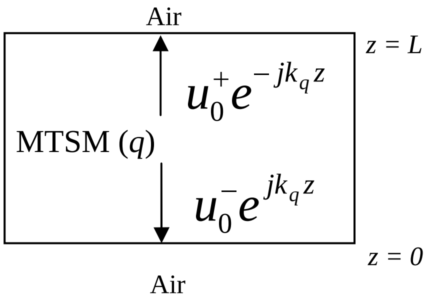

Figure 43. Depiction model of a MTSM sensor with acoustic shear waves traveling upward (+) and downward (-) direction.

General equation of displacement in MTSM sensor, u_q is

$$u_q = (u_0^+ e^{-jk_q z} + u_0^- e^{jk_q z})e^{j\omega t} \qquad \text{……………………………………………….(A1)}$$

General equation of stress in MTSM sensor, T_q is

$$T_q = \mu_q \frac{\partial u_q}{\partial z} \qquad \text{……………………………………………………………….(A2)}$$

<u>• Boundary Condition (BC) at z = *0*:</u>

Since $T_{air} = 0$, $T_q + T_{air} = 0$.

Then $T_q = 0$ at z = *0*.

From the equations (A1) and (A2),

$$T_q = \mu_q \frac{\partial}{\partial z}\left((u_0^+ e^{-jk_q z} + u_0^- e^{jk_q z})e^{j\omega t}\right) = 0$$

$$T_q = -j\mu_q k_q u_0^+ e^{-jk_q z} + j\mu_q k_q u_0^- e^{jk_q z} = 0 \qquad \text{…………………………….…….(A3)}$$

At z = 0 equation (A3) becomes

$u_0^+ = u_0^-$. Let $u_0^+ = u_0^- = u_0$.

Then equation (A1) becomes

$$u_q = u_0\left(e^{-jk_q z} + e^{jk_q z}\right)e^{j\omega t} = 2u_0 \cos(k_q z)e^{j\omega t} \qquad \text{……………………….…….(A4)}$$

Now $T_q = 0$ at z = *L*. Then,

$$-2\mu_q k_q u_0 \sin(k_q L) = 0 \Rightarrow \sin(k_q L) = 0$$

$k_q L = n\pi$, for 1st harmonic, $k_q L = \pi$.

Since $k_q = \frac{\omega_0}{v_q}$, $\frac{\omega_0}{v_q} L = n\pi$.

$$\therefore v_q = \frac{\omega_0 L}{n\pi} \qquad \ldots\ldots\ldots\ldots\ldots\ldots\ldots\ldots\ldots\ldots\ldots\ldots\ldots\ldots\ldots\ldots\ldots\ldots\ldots\text{(A5)}$$

• Attenuation of the Bare MTSM

$$Z_q = \frac{T_{xz}}{v_x} = \left(\mu_q \cdot \frac{\partial(\text{Eq. A4})}{\partial \text{z}} \middle/ \frac{\partial(\text{Eq. A4})}{\partial \text{t}} \right) = \frac{-2\mu_q k_q u_0 \sin(k_q L) e^{j\omega t}}{j 2 u_0 \cos(k_q L) e^{j\omega t}} = j(\mu_q \rho_q)^{1/2} \cdot \tan(k_q L)$$

where, Z_q – shear mechanical impedance at the surface.

T_{xz} – sinusoidal steady-state shear stress in the x-direction on a z-normal plane.

v_x – resulting x-directed surface shear particle velocity.

For the simulation of S_{21} parameters (attenuation, α) of MTSM sensor, the static capacitance, C_0, has to be involved.

$$Z_0 = \frac{1}{j\omega C_0}$$

$$Z_T = \frac{Z_q Z_0}{Z_q + Z_0}$$, and therefore,

$$S_{21} = 20 \cdot \log_{10} \left| \frac{100}{100 + Z_T} \right|$$

9.2 MTSM sensor with a lossless (rigid) film

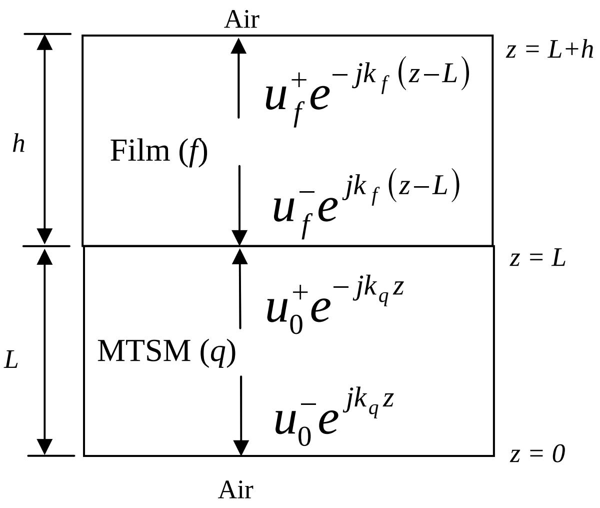

Figure 44. Depiction model of a MTSM sensor with a coupled rigid thin film. Acoustic shear waves travel upward (+) and downward (-) direction in both a MTSM sensor and a rigid thin film.

General equation of displacement in lossless film, u_f is

$$u_f = \left(u_f^+ e^{-jk_f(Z-L)} + u_f^- e^{jk_f(Z-L)}\right) e^{j\omega t} \qquad \text{………………………………..…..(A6)}$$

General equation of stress in lossless film, T_f is

$$T_f = \mu_f \frac{\partial u_f}{\partial z} \qquad \text{……………………………………………………..…….(A7)}$$

• 1st Boundary Condition (BC) at *z* = *L*+*h*:

Since $T_{air} = 0$, $T_f + T_{air} = 0$ at *z* = *L*+*h*.

$$\therefore T_f = \mu_f \left.\frac{\partial u_f}{\partial z}\right|_{z=L+h} = 0$$

From the equations (A6) and (A7),

$$T_f = \mu_f \frac{\partial}{\partial z}\left(\left(u_f^+ e^{-jk_f(z-L)} + u_f^- e^{jk_f(z-L)}\right)e^{j\omega t}\right) = 0 \qquad \text{at } z = L+h.$$

$$T_f = \left(-j\mu_f k_f u_f^+ e^{-jk_f h} + j\mu_f k_f u_f^- e^{jk_f h}\right)e^{j\omega t} = 0$$

$$u_f^- = u_f^+ e^{-2jk_f h}$$

Now equation (A6) becomes

$$u_f = u_f^+\left(e^{-jk_f(z-L)} + e^{-2jk_f h}e^{jk_f(z-L)}\right)e^{j\omega t} \qquad \text{……………………………...………(A8)}$$

• 2nd Boundary Condition (BC) at *z* = *L*:

Due to the boundary conditions, $u_q = u_f$ at *z* = *L*.

From the equations (A4) and (A8),

$$2u_0\cos(k_q L)e^{j\omega t} = u_f^+\left(1 + e^{-2jk_f h}\right)e^{j\omega t}$$

$$\therefore u_f^+ = \frac{2u_0\cos(k_q L)}{1 + e^{-2jk_f h}}\text{, then}$$

$$u_f^- = \frac{2u_0\cos(k_q L)e^{-2jk_f h}}{1 + e^{-2jk_f h}}.$$

Now the equation (A6) becomes

$$u_f = \left(\frac{2u_0 \cos(k_q L)}{1 + e^{-2jk_f h}} e^{-jk_f(z-L)} + \frac{2u_0 \cos(k_q L) e^{-2jk_f h}}{1 + e^{-2jk_f h}} e^{jk_f(z-L)} \right) e^{j\omega t} \quad \ldots\ldots\ldots \text{(A9)}$$

As a check up, at $z = L$, the equation (A9) becomes $u_f = 2u_0 \cos(k_q L) e^{j\omega t}$.

This is same as the equation (A4) at $z = L$.

• <u>3rd Boundary Condition (BC) at $z = L$:</u>

$$T_q + T_f = 0 \quad \text{or} \quad T_q = -T_f$$

$$T_q \Big|_{z=L} = -2\mu_q k_q u_0 \sin(k_q L)$$

$$T_f \Big|_{z=L} = \frac{-2j\mu_f k_f u_0 \cos(k_q L)\left(1 - e^{-2jk_f h}\right)}{1 + e^{-2jk_f h}}$$

$$\therefore 2\mu_q k_q u_0 \sin(k_q L) = \frac{-2j\mu_f k_f u_0 \cos(k_q L)\left(1 - e^{-2jk_f h}\right)}{1 + e^{-2jk_f h}} \quad \ldots\ldots\ldots\ldots\ldots\ldots\ldots \text{(A10)}$$

since $\dfrac{1 - e^{-j\theta}}{1 + e^{-j\theta}} = j \tan\dfrac{\theta}{2}$, the equation (A10) becomes

$$\mu_q k_q \tan(k_q L) = -\mu_f k_f \tan(k_f h) \quad \ldots\ldots\ldots\ldots\ldots\ldots\ldots\ldots\ldots\ldots\ldots\ldots \text{(A11)}$$

If one put the equation (A5) into the left side of the equation (A11)

$$\mu_q k_q \tan(k_q L) = \mu_q k_q \tan\left(\frac{\omega}{v_q} L \right) = \mu_q k_q \tan\left(\frac{\omega}{\omega_0} n\pi \right) = \mu_q k_q \tan\left(\frac{\omega_0 + \Delta\omega}{\omega_0} n\pi \right)$$

$$= \mu_q k_q \tan\left(n\pi + \frac{\Delta\omega}{\omega_0} n\pi \right) = \mu_q k_q \tan\left(\frac{\Delta\omega}{\omega_0} n\pi \right)$$

Now the equation (A11) becomes

$$\mu_q k_q \tan\left(\frac{\Delta\omega}{\omega_0} n\pi\right) = -\mu_f k_f \tan(k_f h) \qquad \ldots\ldots\ldots\ldots\ldots\ldots\ldots\ldots\ldots\ldots\ldots\ldots\text{(A12)}$$

$$\tan\left(\frac{\Delta\omega}{\omega_0} n\pi\right) = -\frac{\mu_f k_f}{\mu_q k_q} \tan(k_f h)$$

$$\left(\frac{\Delta\omega}{\omega_0} n\pi\right) = \tan^{-1}\left(-\frac{\mu_f k_f}{\mu_q k_q} \tan(k_f h)\right)$$

$$\Delta\omega = \frac{\omega_0}{n\pi} \tan^{-1}\left(-\frac{\mu_f v_q}{\mu_q v_f} \tan(k_f h)\right)$$

$$\therefore \Delta f = \frac{f_0}{n\pi} \tan^{-1}\left(-\frac{\mu_f v_q}{\mu_q v_f} \tan(k_f h)\right)$$

The equation (A12) can be simplified.

In case of $\frac{\Delta\omega}{\omega_0} << 1$ and $k_f h << 1$, then $\tan\left(\frac{\Delta\omega}{\omega_0} n\pi\right) \approx \frac{\Delta\omega}{\omega_0} n\pi$ and $\tan(k_f h) \approx k_f h$.

Now the equation (A12) becomes

$$\mu_q k_q n\pi \frac{\Delta\omega}{\omega_0} = -\mu_f k_f^2 h, \quad \frac{\Delta\omega}{\omega_0} \mu_q \left(\frac{\omega}{v_q}\right) n\pi = -\mu_f \left(\frac{\omega}{v_f}\right)^2 h.$$

$$\frac{\Delta\omega}{\omega_0} \mu_q \omega \left(\frac{\rho_q}{\mu_q}\right)^{1/2} n\pi = -\mu_f \omega^2 \left(\frac{\rho_f}{\mu_f}\right) h$$

$$\frac{\Delta\omega}{\omega_0} (\mu_q \rho_q)^{1/2} n\pi = -\omega \rho_f h = -(\omega_0 + \Delta\omega) \rho_f h$$

$$\therefore \Delta\omega = -\frac{\omega_0^2 \rho_f h}{n\pi (\mu_q \rho_q)^{1/2} + \omega_0 \rho_f h}$$

$$\therefore \Delta f = -\frac{2 f_0^2 \rho_f h}{n(\mu_q \rho_q)^{1/2} + 2 f_0 \rho_f h} \qquad \text{…………(A13)}$$

As a check up, when h << 1,

then $n(\mu_q \rho_q)^{1/2} >> 2 f_0 \rho_f h$ and $n(\mu_q \rho_q)^{1/2} + 2 f_0 \rho_f h \approx n(\mu_q \rho_q)^{1/2}$

Now the equation (A13) becomes

$$\therefore \Delta f = -\frac{2 f_0^2 \rho_f h}{n(\mu_q \rho_q)^{1/2}}$$ which is same as Sauerbrey equation.

9.3 MTSM sensor with viscous loading

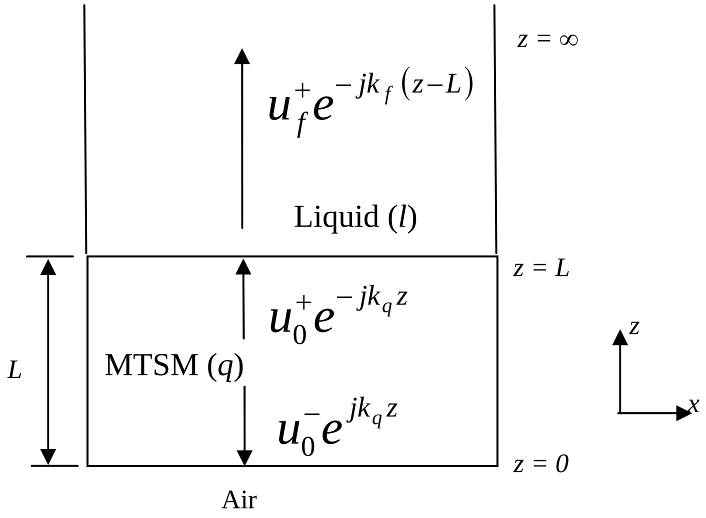

Figure 45. Depiction model of a MTSM sensor with a semi infinite liquid layer. Acoustic shear waves travel upward (+) and downward (-) direction in a MTSM sensor while only penetrate in upward direction due to the semi-infinite thickness of liquid layer.

• Boundary Conditions:

Continuity of the transverse displacement of the interface at bottom interface ($z = 0$)

$$u_{xq} = u_{xair}$$

$$T_{xq} = T_{xair}\big|_{T(air=vacuum)} = 0$$

- u_{xq} indicates the displacement of quartz crystal at the interface in x-axis.

- u_{xair} indicates the displacement of air at the interface in x-axis.

- T_{xq} indicates the stress of the quartz crystal at the interface.

- T_{xair} indicates the stress of the air at the interface.

Continuity of the transverse displacement of the interface at upper interface ($z = L$)

$$u_{xq} = u_{xl}$$

$$T_{xq} = T_{xl}$$

- u_{xl} indicates the displacement of liquid at the interface in x-axis.

- T_{xl} indicates the stress of the liquid at the interface.

To find displacement and stress in the liquid, one need to specify the allowable shear motion in the liquid.

• Model for a Liquid: Newtonian Liquid

- Navier-Stokes Equation: The motion of a non-turbulent, Newtonian fluid is governed by the Navier-Stokes equation. This equation describes how the velocity, pressure, temperature, and density of a moving fluid are related and the effects of viscosity on the flow.

$$\rho \frac{D\vec{v}}{dt} = -\nabla\rho + \rho g + \nabla\times\left[\eta\left(\nabla\times\vec{v}\right)\right] + \nabla\left[\left(\dot{\eta}+\frac{4}{3}\eta\right)\nabla\cdot\vec{v}\right] \quad \text{……………...……(A14)}$$

where: $\vec{v}$ = particle velocity, $\frac{D}{dt}$ = the substantive derivative

ρ = density, g = gravity

η = viscosity, $\dot{\eta}$ = second viscosity

Assumptions:

- η = constant, Incompressible fluid $\Rightarrow$ $\nabla\cdot\vec{v} = 0$

Then the equation (A14) can be rewritten as follows,

$$\rho\underbrace{\left[\frac{\partial v}{\partial t} + \left(\nabla\cdot\vec{v}\right)\vec{v}\right]}_{\frac{D\vec{v}}{dt}} = -\nabla p + \rho g + \eta\nabla^2\vec{v} \quad \text{…………………………..…...……..(A15)}$$

- Small acoustic wave amplitude (linear approximation): $\left(\nabla\cdot\vec{v}\right)\vec{v} = 0$

- No pressure influence: $\nabla p = 0$

- No gravity force influence: $\rho g = 0$

Then the equation (A15) will be,

$$\rho \frac{\partial \vec{v}}{\partial t} = \eta \nabla^2 \vec{v}$$ → a form of diffusion equation ………………………….(A16)

For shear waves propagating in the "*z*" direction with the displacement along "*x*" direction, the Navier-Stokes equation yields:

$$\frac{\partial v_x}{\partial t} = r \frac{\partial^2 v_x}{\partial z^2} \qquad \Rightarrow \qquad T = \eta \frac{\partial u_x}{\partial z},$$

where T = stress, and $r = \frac{\eta}{\rho}$ → kinematic viscosity.

The solution to the diffusion equation (A16):

$$v_x = v_{x0} e^{-jk_z z} \cdot e^{j\omega t}$$ ……………………………………………………….(A17)

where v_x – particle velocity in x-axis.

v_{x0} – initial particle velocity.

k_z – wave vector.

$k_z = k_l - jk_l$ l = liquid

$$k_l = \left(\frac{\omega}{2r}\right)^{1/2} = \left(\frac{\omega \rho_l}{2\eta_l}\right)^{1/2}$$ ……………………………………….…..(A18)

Im k_z (imaginary part of the wave vector k_z) = α_l - damping coefficient.

$$k_l = \frac{\omega}{v_l} \rightarrow v_l = \frac{\omega}{k_l} = \left(\frac{2r}{\omega}\right)^{1/2}$$

Then $v_x = v_{x0} e^{-\alpha_l z} \cdot e^{j(\omega t - k_l z)}$

Since shear waves only penetrates in a viscous media,

$$\frac{v_x(z = d_z)}{v_x(z = 0)} = e^{-\alpha_l \cdot d_z} = e^{-1}, \qquad d_z = \frac{1}{\alpha_l}$$

<u>• Boundary Conditions at the upper interface (*z = L*):</u>

$$u_{xq} = u_{xl}\Big|_{z=L}$$

$$v_{xq} = v_{xl}\Big|_{z=L} \quad \text{……………………………………………………………..(A19)}$$

v_{xq} – particle velocity of the quartz crystal in x-axis.

v_{xl} – particle velocity of liquid in x-axis

Now the equation (A17) at the interface $z = L$ becomes

$$v_{xl}(z,t) = v_{x0} e^{-\alpha_l (z-L)} \cdot e^{j[\omega t - k_l (z-L)]} \quad \text{…………………………………..(A20)}$$

<u>• Boundary Conditions at the upper interface (*z = L, t = 0*):</u>

Now the equation (A19) becomes

$$v_{xl} = v_{x0} \quad \text{……………………………………………….……………(A21)}$$

$$v_{xq} = 2 j\omega u_0 \cos(kL) \quad \text{…………………………………….………...….(A22)}$$

Comparing the equations (A21) and (A22), one gets:

$$v_{x0l} = 2j\omega u_0 \cos(kL)$$

The solution for shear waves in liquid: the equation (A20) takes a form:

$$v_{xl}(z,t) = 2j\omega_0 u_0 \cos(k_q L) e^{-\alpha_l (z-L)} e^{j[\omega t - k_l (z-L)]} \quad \ldots\ldots\ldots\ldots\ldots\ldots\ldots\ldots\ldots\ldots\text{(A23)}$$

• <u>Using the second Boundary Conditions at the upper interface ($z = L$):</u>

$$T_q = T_l$$

$$T_q = \mu_q \frac{\partial u_x}{\partial z}; \qquad T_l = \eta_l \frac{\partial v_x}{\partial z}$$

$$T_q = \mu_q \left[\frac{\partial}{\partial z} \text{Eq. (A4)} \right] = 2u_0 \mu_q k_q \sin(k_q z) e^{j\omega t} \Big|_{z=L} = 2u_0 k_q \sin(k_q L) e^{j\omega t}$$

$$T_l = \eta_l \left[\frac{\partial}{\partial t} (\text{Eq. (A23)}) \right] \Bigg|_{z=L} = -2j\omega u_0 \cos(k_q L) \cdot \alpha_l \cdot e^{j\omega t} - 2\omega u_0 \cos(k_q L) \cdot k_l \cdot e^{j\omega t}$$

$$= \text{Im}\, T_l + \text{Re}\, T_l$$

Boundary condition: the in-phase component of the shear stress on the liquid side of the interface must equal and opposite of the shear stress on the quartz side.

$T_q = \text{Re}\, T_l$, Re T_l – real part of the stress of liquid T_l

$$2\mu_q u_0 k_q \sin(k_q L) \cdot e^{j\omega t} = -2\eta_l \omega u_0 \cos(k_q L) \cdot k_l \cdot e^{j\omega t}$$

Hence, $\tan(k_q L) = -\omega \frac{\eta_l}{\mu_q} \frac{k_l}{k_q} = -\omega \frac{\eta_l}{\mu_q} \cdot \frac{\text{Eq. (A18)}}{\text{Eq. (A5)}}$

and $\tan\left(\omega \left(\frac{\rho_q}{\mu_q} \right)^{1/2} \cdot L \right) = -\left(\frac{\omega}{2} \frac{\rho_l \eta_l}{\rho_q \mu_q} \right)^{1/2}$ $\ldots\ldots\ldots\ldots\ldots\ldots\ldots\ldots\ldots\ldots\ldots\ldots\text{(A24)}$

but $k_q L = \omega \left(\frac{\rho_q}{\mu_q} \right)^{1/2} \cdot L \cdot \text{Eq.(A5)} = \frac{\omega}{\omega_0} \cdot \pi$

because $\left(\frac{\rho_q}{\mu_q}\right)^{1/2} \cdot L = \frac{\pi}{\omega_0}$ and $\omega = \omega_0 + \Delta\omega$.

$$\tan\left(\left(\frac{\omega_0 + \Delta\omega}{\omega_0}\right)\cdot\pi\right) = \tan\left(\left(1+\frac{\Delta\omega}{\omega_0}\right)\cdot\pi\right) = \tan\left(\pi + \frac{\Delta\omega}{\omega_0}\pi\right) = \tan\left(\frac{\Delta\omega}{\omega_0}\cdot\pi\right)$$

Then the equation (24) takes a form:

$$\tan\left(\frac{\Delta\omega}{\omega_0}\pi\right) = -(\omega_0 + \Delta\omega)^{1/2}\cdot\left(\frac{\rho_l\eta_l}{2\rho_q\mu_q}\right)^{1/2} \quad \text{………………………...………..(A25)}$$

For $\frac{\Delta\omega}{\omega_0} << 1,$ $\tan\left(\frac{\Delta\omega}{\omega_0}\pi\right) \approx \frac{\Delta\omega}{\omega_0}\pi$

And since $(\omega_0 + \Delta\omega)^{1/2} \approx \omega_0^{\ 1/2}$,

The equation (A25) takes a form:

$$\Delta\omega = -\frac{\omega_0^{\ 3/2}}{\pi}\left(\frac{\rho_l\eta_l}{2\rho_q\mu_q}\right)^{1/2}$$

$$\text{or} \quad \Delta f = -f_0^{\ 3/2}\left(\frac{\rho_l\eta_l}{\pi\rho_q\mu_q}\right)^{1/2} \quad \text{…………..Kanazawa equation ………..…(A26)}$$

or $\Delta f = -A\cdot(\rho_l\eta_l)^{1/2}$, where $A = f_0^{\ 3/2}\left(\frac{1}{\pi\rho_q\mu_q}\right)^{1/2}$

9.4 MTSM sensor with viscoelastic (VE) film

• Constitutive equation of VE Material:

$$T_f = \mu S + \eta \frac{dS}{dt} = \mu\left(\frac{du}{dz}\right) + \eta \frac{dv}{dz}$$

Since $v = \frac{du}{dt}$, if we let $v = v_0 e^{j\omega t}$, then $u = \frac{1}{j\omega} v_0 e^{j\omega t} = \frac{v}{j\omega}$. $\therefore v = j\omega u$

$$\therefore T_f = \mu\left(\frac{du}{dz}\right) + \eta\left(j\omega \frac{du}{dz}\right) = \left(\mu_f + j\omega\eta_f\right)\frac{du}{dz} \qquad \text{……………………...….(A27)}$$

Now let's assume $\mu_{eff} = \mu_f + j\omega\eta_f$ in this Maxwell Model.

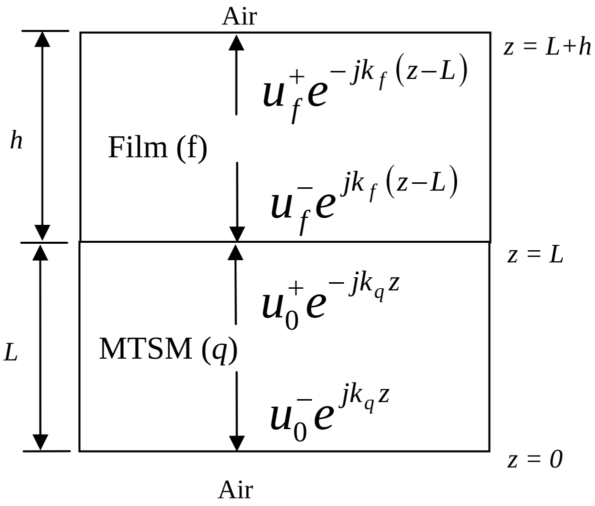

Figure 46. Depiction model of a MTSM sensor with a viscoelastic layer. Acoustic shear waves travel upward (+) and downward (-) direction in a MTSM sensor while the traveling characteristic of acoustic waves in VE medium mainly depends on the mechanical and geometrical properties of a VE layer.

General equation of displacement in VE film, u_f is

$$u_f = \left(u_f^+ e^{-jk_f(Z-L)} + u_f^- e^{jk_f(Z-L)}\right)e^{j\omega t} \qquad \text{………………………………….………………(A28)}$$

General equation of stress in VE film, T_f is

$$T_f = \mu_{eff}\frac{\partial u_f}{\partial z} = \left(\mu_f + j\omega\eta_f\right)\frac{du_f}{dz} \qquad \text{………………….…………….............(A29)}$$

However, since the film is VE material,

$k_f = \mathrm{Re}\left(k_f\right) - j\left(k_f\right) = k - j\alpha$: wave vector.

Particle velocity in VE film, $v_f = \left(\dfrac{\mu_{eff}}{\rho_f}\right)^{1/2} = \left(\dfrac{\mu_f + j\omega\eta_f}{\rho_f}\right)^{1/2}$

$$k_f = \frac{\omega}{v_f} = \omega\left(\frac{\rho_f}{\mu_f + j\omega\eta_f}\right)^{1/2}$$

$$k = \mathrm{Re}\left(k_f\right) = \omega\left(\frac{\rho_f^2}{\mu_f^2 + \left(\omega\eta_f\right)^2}\right)^{1/4}\cos\left(-\frac{1}{2}\tan^{-1}\left(\frac{\omega\eta_f}{\mu_f}\right)\right)$$

$$\alpha = \mathrm{Im}\left(k_f\right) = -\omega\left(\frac{\rho_f^2}{\mu_f^2 + \left(\omega\eta_f\right)^2}\right)^{1/4}\sin\left(-\frac{1}{2}\tan^{-1}\left(\frac{\omega\eta_f}{\mu_f}\right)\right)$$

• 1st Boundary Condition (BC) at $z = L+h$:

Since $T_{air} = 0$, $T_f + T_{air} = 0$ at $z = L+h$.

$$\therefore T_f = \mu_{eff}\left.\frac{\partial u_f}{\partial z}\right|_{z=L+h} = 0$$

From the equations (A28) and (A29),

$$T_f = \mu_{eff} \frac{\partial}{\partial z}\left(\left(u_f^+ e^{-jk_f(z-L)} + u_f^- e^{jk_f(z-L)}\right)e^{j\omega t}\right) = 0 \qquad \text{at } z = L+h.$$

$$T_f = \left(\mu_f + j\omega\eta_f\right)\left(-jk_f u_f^+ e^{-jk_f h} + jk_f u_f^- e^{jk_f h}\right)e^{j\omega t} = 0$$

$$-j\mu_f k_f u_f^+ e^{-jk_f h} + j\mu_f k_f u_f^- e^{jk_f h} + \omega\eta_f k_f u_f^+ e^{-jk_f h} - \omega\eta_f k_f u_f^- e^{jk_f h} = 0$$

$$\omega\eta_f k_f\left(u_f^+ e^{-jk_f h} - u_f^- e^{jk_f h}\right) + j\mu_f k_f\left(u_f^- e^{jk_f h} - u_f^+ e^{-jk_f h}\right) = 0 \quad \text{………….……(A30)}$$

To make the equation (A30) becomes 0, then $u_f^- e^{jk_f h} = u_f^+ e^{-jk_f h}$.

$$\therefore u_f^- = u_f^+ e^{-2jk_f h}$$

Now the equation (A28) becomes $u_f = u_f^+ (e^{-jk_f(z-L)} + e^{-2jk_f h} e^{jk_f(z-L)})e^{j\omega t}$ ……………(A31)

<u>• 2nd Boundary Condition (BC) at *z* = *L*:</u>

$$u_q = u_f$$

From the equations (A4) and (A31),

$$2u_0 \cos(k_q L)e^{j\omega t} = u_f^+\left(1 + e^{-2jk_f h}\right)e^{j\omega t}$$

$$\therefore u_f^+ = \frac{2u_0 \cos\left(k_q L\right)}{1 + e^{-2jk_f h}} \quad \text{……………………………………………..……. (A32)}$$

If one put the equation (A32) back into the equation (A31), then the equation (A31) becomes

$$u_f = \frac{2u_0 \cos\left(k_q L\right)}{1 + e^{-2jk_f h}}(e^{-jk_f(z-L)} + e^{-2jk_f h} e^{jk_f(z-L)})e^{j\omega t} \quad \text{……………………...….(A33)}$$

To check up the equation (A33) at *z* = *L*,

$u_f\big|_{z=L} = 2u_0 \cos(k_q L) e^{j\omega t}$, same as the equation (A4) at $z = L$.

• 3rd Boundary Condition (BC) at $z = L$:

$$T(q) + T(f) = 0 \quad \text{or} \quad T(q) = -T(f)$$

$$T(q)\big|_{z=L} = -2\mu_q k_q u_0 \sin(k_q L)$$

$$T(f) = \mu_{eff} \frac{du(f)}{dz} = (\mu_f + j\omega\eta_f)\frac{du(f)}{dz}$$

$$= (\mu_f + j\omega\eta_f)\frac{2u_0\cos(k_q L)}{1+e^{-2jk_f h}}\left(-jk_f e^{-jk_f(z-L)} + jk_f e^{-2jk_f h} e^{jk_f(z-L)}\right)e^{j\omega t}$$

$$\therefore 2\mu_q k_q u_0 \sin(k_q L) = (\mu_f + j\omega\eta_f)\left(\frac{2u_0\cos(k_r L)}{1+e^{-2jk_f h}}\left(jk_f\left(1-e^{-2jk_f h}\right)\right)\right) \text{ at z = L.}$$

$$\mu_q k_q \tan(k_q L) = jk_f(\mu_f + j\omega\eta_f)\left(\frac{1-e^{-2jk_f h}}{1+e^{-2jk_f h}}\right) = -k_f(\mu_f + j\omega\eta_f)\tan(k_f h)$$

Since $\tan(k_q L) = \tan\left(\frac{\Delta\omega}{\omega_0} n\pi\right)$,

$$\tan\left(\frac{\Delta\omega}{\omega_0} n\pi\right) = \frac{-k_f(\mu_f + j\omega\eta_f)\tan(k_f h)}{\mu_q k_q}$$

$$\frac{\Delta\omega}{\omega_0} n\pi = \tan^{-1}\left(\frac{-k_f(\mu_f + j\omega\eta_f)\tan(k_f h)}{\mu_q k_q}\right)$$

$$\therefore \Delta f = \frac{f_0}{n\pi}\tan^{-1}\left(\frac{-k_f(\mu_f + j\omega\eta_f)\tan(k_f h)}{\mu_q k_q}\right) \qquad \text{………………………(A34)}$$

In case with pure viscous liquid loading, $(\mu_f + j\omega\eta_f) \Rightarrow j\omega\eta_f$.

The magnitudes of the real and imaginary components of the propagation constant are equal, and it can be shown that in the limit of an infinitely thick layer of viscous load.

$\lim\limits_{h\to\infty}\tan\left(k_f h\right)=\frac{1}{j}$, then right side of the equation (A34) becomes

$$-k_f\left(\mu_f + j\omega\eta_f\right)\tan\left(k_f h\right)=-k_f\left(j\omega\eta_f\right)\frac{1}{j}=-\omega\left(\frac{\omega\rho_f\eta_f}{2}\right)^{1/2}$$

$$\therefore \Delta f = -\frac{f_0^{\,3/2}}{n}\left(\frac{\rho_f\eta_f}{\pi\rho_q\mu_q}\right)^{1/2} \quad \text{for 1}^{\text{st}} \text{ harmonic, } n = 1. \qquad \ldots\ldots\ldots\ldots\ldots\ldots\ldots\ldots\text{(A35)}$$

Now one can find that the equation (A35) is same as Kanazawa equation, (A26).

• Attenuation of the Bare MTSM with VE film

$$Z_f = \frac{T_{xz}}{v_x} = \left(\mu_{eff}\cdot\frac{\partial\left(\mathrm{A33}\right)}{\partial \mathrm{z}} \Bigg/ \frac{\partial\left(\mathrm{A33}\right)}{\partial \mathrm{t}}\right) = j\left(\mu_{eff}\,\rho_f\right)^{1/2}\cdot\tan\left(k_f h\right)$$

where, Z_q – shear mechanical impedance at the surface.

T_{xz} – sinusoidal steady-state shear stress in the *x*-direction on a *z*-normal plane.

v_x – resulting *x*-directed surface shear particle velocity.

For the simulation of S_{21} parameters (attenuation, α) of a MTSM sensor, the static capacitance, C_0, has to be involved and Z_q has to be added to Z_f to calculate the total impedance of motional branch, Z_s.

$$Z_0 = \frac{1}{j\omega C_0}$$

$$Z_s = Z_q + Z_f,$$

$$Z_T = \frac{Z_s Z_0}{Z_s + Z_0},$$

and therefore, $S_{21} = 20 \cdot \log_{10} \left| \frac{100}{100 + Z_T} \right|$

9.5 MatLab program codes for the simulations

For the simulation of the MTSM sensor with a VE film, the m-file format of MatLab software was used to generate 2-D type line graphs and 3-D type surface mesh graphs. For the line graphs, only one variable was changed while other three variables were fixed to mimic the phase of the VE film for the specific simulation. The simulation of the relative Δf was generated by using the equation A34, while the simulation of the attenuation was created by the equation A35 in appendix. For the surface mesh graphs, two variables were changed while other two variables were fixed. Followings are the program codes for the simulations in this thesis.

9.5.1 M-file of the simulations in Figure 12 and 13.

Following M-file is to generate the relative Δf and α simulations of MTSM in harmonics of an evaporation process of a Newtonian liquid. Simulations of different Newtonian liquid can be done by giving different viscosity or density values to the variables, nf and rf, in the M-file.

For the relative Δf simulation of MTSM in harmonics

```
clear;
hold on
%----- Info. about TSM sensor -------
uq=2.947e10;        %stiffness of MTSM
rq=2651;            %density of MTSM
vq=(uq/rq)^.5;      %wave velocity in MTSM
L=1.67e-4;          %thickness of MTSM
%--------- Info. about Film ------------------
h=1e-7:1e-8:1e-5;          %thickness
uf=0;                       %stiffness
rf=1000;                   %density
nf=.001;                   %viscosity
vf=(uf/rf)^.5;
%------ Info. about 1st harmonic --------------
n=1;                      %harmonic
f0=1e7;
w=2*pi*f0;
kq=w/vq;
k=w*(rf^2/(uf^2+(w*nf)^2))^.25*cos(-.5*atan(w*nf/uf));
a=-w*(rf^2/(uf^2+(w*nf)^2))^.25*sin(-.5*atan(w*nf/uf));
kf=k-j*a;
df=(f0/(n*pi))*atan(((-kf*(uf+j*w*nf)).*tan(kf.*h))/(uq*kq));
rdf=real(df);             %real part of df
Rrdf=rdf/f0;              %relative changes
```

```
plot(h,Rrdf,'-')
xlabel('Thickness [m]')
ylabel('Relative Changes in Res. Freq.')

%------ Info. about 3rd harmonic --------------
n=3;      %harmonic
f0=1e7*3;
w=2*pi*f0;
kq=w/vq;
k=w*(rf^2/(uf^2+(w*nf)^2))^.25*cos(-.5*atan(w*nf/uf));
a=-w*(rf^2/(uf^2+(w*nf)^2))^.25*sin(-.5*atan(w*nf/uf));
kf=k-j*a;
df=(f0/(n*pi))*atan(((-kf*(uf+j*w*nf)).*tan(kf.*h))/(uq*kq));
rdf=real(df);            %real part of df
Rrdf=rdf/f0;             %relative changes
plot(h,Rrdf,'--')
%------ Info. about 5th harmonic --------------
n=5;      %harmonic
f0=1e7*5;
w=2*pi*f0;
kq=w/vq;
k=w*(rf^2/(uf^2+(w*nf)^2))^.25*cos(-.5*atan(w*nf/uf));
a=-w*(rf^2/(uf^2+(w*nf)^2))^.25*sin(-.5*atan(w*nf/uf));
kf=k-j*a;
df=(f0/(n*pi))*atan(((-kf*(uf+j*w*nf)).*tan(kf.*h))/(uq*kq));
rdf=real(df);            %real part of df
Rrdf=rdf/f0;             %relative changes
plot(h,Rrdf,':')
%------ Info. about 7th harmonic --------------
n=7;      %harmonic
f0=1e7*7;
w=2*pi*f0;
kq=w/vq;
k=w*(rf^2/(uf^2+(w*nf)^2))^.25*cos(-.5*atan(w*nf/uf));
a=-w*(rf^2/(uf^2+(w*nf)^2))^.25*sin(-.5*atan(w*nf/uf));
kf=k-j*a;
```

```
df=(f0/(n*pi))*atan(((-kf*(uf+j*w*nf)).*tan(kf.*h))/(uq*kq));
rdf=real(df);             %real part of df
Rrdf=rdf/f0;              %relative changes

plot(h,Rrdf,'-.')
```

For the α simulation of MTSM in harmonics

```
clear;
uq=2.947e10;                    %TSM stiffness
rq=2651;                       %TSM density
nq=3.5e-4;                      %TSM viscosity
vq=(uq/rq)^.5;
e22=3.982e-11;
r=2.5e-3;                       %radius of 10 MHz MAIB
area=pi*r^2;
K2=7.74e-3;
hf=1e-7:1e-8:1e-6;               %film thickness
uf=0;                          %film stiffness
rf=1000;                       %film density
nf=.001;                         %film viscosity
vf=(uf/rf)^.5;
% 1 H =========================
N=1;       %harmonic
f0=1e7*N;
w=2*pi*f0;
kq=w/vq;
k=w*(rf^2/(uf^2+(w*nf)^2))^.25*cos(-.5*atan(w*nf/uf));
a=-w*(rf^2/(uf^2+(w*nf)^2))^.25*sin(-.5*atan(w*nf/uf));
kf1=k-j*a;
df=(f0/(N*pi))*atan(((-kf1*(uf+j*w*nf))*tan(kf1.*hf))./(uq*kq));
ResF=f0+real(df);
Realw=2*pi*ResF;
L=1.67e-4;
C0=e22*area/L;
C1=8*K2*C0/(N*pi)^2;
```

```
L1=1/(w^2*C1);
R1=nq/(uq*C1);
ueff=uf+(j*Realw*nf);
kf=Realw.*(rf./ueff).^.5;
Zm=j*(ueff*rf).^.5.*tan(kf.*hf);
A=N*pi/(4*K2*w*C0);
B=N*pi/(4*K2*w^2*C0);
R2=A*real(Zm)/(rq*uq)^.5;
L2=B*imag(Zm)/(rq*uq)^.5;
Zq=R1+(1./(j*Realw*C1))+(j*Realw*L1);
Ze=R2+(j*Realw.*L2);
Zs=Zq+Ze;
Z0=1./(j*Realw*C0);
Zt=(Zs.*Z0)./(Zs+Z0);
MagZt=100./(100+Zt);
RMagZt=real(MagZt);
IMagZt=imag(MagZt);
MZt=(RMagZt.^2+IMagZt.^2).^.5;
atte=20*log10(MZt);
plot(hf,-atte,'-'); hold on;
xlabel('Thickness [m]')
ylabel('Attenuation [dB]')
% 3 H ===============
N=3;       %harmonic
f0=1e7*N;
w=2*pi*f0;
kq=w/vq;
k=w*(rf^2/(uf^2+(w*nf)^2))^.25*cos(-.5*atan(w*nf/uf));
a=-w*(rf^2/(uf^2+(w*nf)^2))^.25*sin(-.5*atan(w*nf/uf));
kf1=k-j*a;
df=(f0/(N*pi))*atan(((-kf1*(uf+j*w*nf))*tan(kf1.*hf))./(uq*kq));
ResF=f0+real(df);
Realw=2*pi*ResF;
L=1.67e-4;
C0=e22*area/L;
C1=8*K2*C0/(N*pi)^2;
```

```
L1=1/(w^2*C1);
R1=nq/(uq*C1);
ueff=uf+(j*Realw*nf);
kf=Realw.*(rf./ueff).^.5;
Zm=j*(ueff*rf).^.5.*tan(kf.*hf);
A=N*pi/(4*K2*w*C0);
B=N*pi/(4*K2*w^2*C0);
R2=A*real(Zm)/(rq*uq)^.5;
L2=B*imag(Zm)/(rq*uq)^.5;
Zq=R1+(1./(j*Realw*C1))+(j*Realw*L1);
Ze=R2+(j*Realw.*L2);
Zs=Zq+Ze;
Z0=1./(j*Realw*C0);
Zt=(Zs.*Z0)./(Zs+Z0);
MagZt=100./(100+Zt);
RMagZt=real(MagZt);
IMagZt=imag(MagZt);
MZt=(RMagZt.^2+IMagZt.^2).^.5;
atte=20*log10(MZt);
plot(hf,-atte,'--'); hold on;
% 5 H ==============
N=5;      %harmonic
f0=1e7*N;
w=2*pi*f0;
kq=w/vq;
k=w*(rf^2/(uf^2+(w*nf)^2))^.25*cos(-.5*atan(w*nf/uf));
a=-w*(rf^2/(uf^2+(w*nf)^2))^.25*sin(-.5*atan(w*nf/uf));
kf1=k-j*a;
df=(f0/(N*pi))*atan(((-kf1*(uf+j*w*nf))*tan(kf1.*hf))./(uq*kq));
ResF=f0+real(df);
Realw=2*pi*ResF;
L=1.67e-4;
C0=e22*area/L;
C1=8*K2*C0/(N*pi)^2;
L1=1/(w^2*C1);
R1=nq/(uq*C1);
```

```
ueff=uf+(j*Realw*nf);
kf=Realw.*(rf./ueff).^.5;
Zm=j*(ueff*rf).^.5.*tan(kf.*hf);
A=N*pi/(4*K2*w*C0);
B=N*pi/(4*K2*w^2*C0);
R2=A*real(Zm)/(rq*uq)^.5;
L2=B*imag(Zm)/(rq*uq)^.5;
Zq=R1+(1./(j*Realw*C1))+(j*Realw*L1);
Ze=R2+(j*Realw.*L2);
Zs=Zq+Ze;
Z0=1./(j*Realw*C0);
Zt=(Zs.*Z0)./(Zs+Z0);
MagZt=100./(100+Zt);
RMagZt=real(MagZt);
IMagZt=imag(MagZt);
MZt=(RMagZt.^2+IMagZt.^2).^.5;
atte=20*log10(MZt);
plot(hf,-atte,':'); hold on;
% 7 H ===============
N=7;      %harmonic
f0=1e7*N;
w=2*pi*f0;
kq=w/vq;
k=w*(rf^2/(uf^2+(w*nf)^2))^.25*cos(-.5*atan(w*nf/uf));
a=-w*(rf^2/(uf^2+(w*nf)^2))^.25*sin(-.5*atan(w*nf/uf));
kf1=k-j*a;
df=(f0/(N*pi))*atan(((-kf1*(uf+j*w*nf))*tan(kf1.*hf))./(uq*kq));
ResF=f0+real(df);
Realw=2*pi*ResF;
L=1.67e-4;
C0=e22*area/L;
C1=8*K2*C0/(N*pi)^2;
L1=1/(w^2*C1);
R1=nq/(uq*C1);
ueff=uf+(j*Realw*nf);
kf=Realw.*(rf./ueff).^.5;
```

```
Zm=j*(ueff*rf).^.5.*tan(kf.*hf);
A=N*pi/(4*K2*w*C0);
B=N*pi/(4*K2*w^2*C0);
R2=A*real(Zm)/(rq*uq)^.5;
L2=B*imag(Zm)/(rq*uq)^.5;
Zq=R1+(1./(j*Realw*C1))+(j*Realw*L1);
Ze=R2+(j*Realw.*L2);
Zs=Zq+Ze;
Z0=1./(j*Realw*C0);
Zt=(Zs.*Z0)./(Zs+Z0);
MagZt=100./(100+Zt);
RMagZt=real(MagZt);
IMagZt=imag(MagZt);
MZt=(RMagZt.^2+IMagZt.^2).^.5;
atte=20*log10(MZt);
plot(hf,-atte,'-.'); hold off;
```

9.5.2 M-file of the simulations in Figure 14.

Following M-file is to generate the effect of the changes in viscosity and thickness to the MTSM response (relative Δf and α) in harmonics. Simulations of different harmonics can be done by giving a different harmonic value to the variable, n, in the M-file.

For the relative Δf simulation of MTSM in harmonics

```
%----- Info. about TSM sensor -------
uq=2.947e10;
rq=2651;
vq=(uq/rq)^.5;
L=1.67e-4;
```

```
%--------- Info. about Film ------------------
rf=1000;           %density
uf=0;             %stiffness
[nf,hf]=meshgrid([1e-3:1e-4:.1],[1e-7:1e-8:1e-5]);      %viscosity      &
thickness
vf=(uf/rf)^.5;
%------ Info. about 1st harmonic --------------
n=1;       %harmonic
f0=1e7*n;
w=2*pi*f0;
kq=w/vq;
k=w*(rf^2./(uf^2+(w.*nf).^2)).^.25.*cos(-.5*atan(w*nf/uf));
a=-w*(rf^2./(uf^2+(w.*nf).^2)).^.25.*sin(-.5*atan(w*nf/uf));
kf=k-j*a;
df=(f0/(n*pi))*atan(((-kf.*(uf+j*w*nf)).*tan(kf.*hf))/(uq*kq));
rdf=real(df);             %real part of df
Rrdf=rdf/f0;              %relative changes
mesh(hf,nf,Rrdf);
xlabel('Thickness [m]')
ylabel('Viscosity [kg/ms]')
zlabel('Relative Changes in Res. Freq.')
```

For the α simulation of MTSM in harmonics

```
clear;
uq=2.947e10;                      %TSM stiffness
rq=2651;                         %TSM density
nq=3.5e-4;                        %TSM viscosity
vq=(uq/rq)^.5;
e22=3.982e-11;
r=2.5e-3;                        %radius of 10 MHz MAIB
area=pi*r^2;
K2=7.74e-3;
[nf,hf]=meshgrid([1e-3:1e-4:.1],[1e-7:1e-8:1e-5]);
rf=1000;                         %film density
uf=1e5;                          %film stiffness
```

```
N=1;       %harmonic
f0=1e7*N;
w=2*pi*f0;
kq=w/vq;
k=w*(rf^2./(uf.^2+(w*nf).^2)).^.25.*cos(-.5*atan(w*nf./uf));
a=-w*(rf^2./(uf.^2+(w*nf).^2)).^.25.*sin(-.5*atan(w*nf./uf));
kf1=k-j*a;
df=(f0/(N*pi))*atan(((-kf1.*(uf+j*w*nf)).*tan(kf1.*hf))/(uq*kq));
ResF=f0+real(df);
Realw=2*pi*ResF;
L=1.67e-4;
C0=e22*area/L;
C1=8*K2*C0/(N*pi)^2;
L1=1/(w^2*C1);
R1=nq/(uq*C1);
ueff=uf+(j*Realw.*nf);
kf=Realw.*(rf./ueff).^.5;
Zm=j*(ueff.*rf).^.5.*tan(kf.*hf);
A=N*pi/(4*K2*w*C0);
B=N*pi/(4*K2*w^2*C0);
R2=A.*real(Zm)./(rq*uq)^.5;
L2=B.*imag(Zm)./(rq*uq)^.5;
Zq=R1+(1./(j*Realw*C1))+(j*Realw*L1);
Ze=R2+(j*Realw.*L2);
Zs=Zq+Ze;
Z0=1./(j*Realw.*C0);
Zt=(Zs.*Z0)./(Zs+Z0);
RZt=real(Zt);
IZt=imag(Zt);
MZt=(RZt.^2+IZt.^2).^.5;
atte=20*log10(100./(100+MZt));
mesh(hf,nf,-atte);
xlabel('Thickness [m]')
ylabel('Viscosity [kg/ms]')
zlabel('Attenuation [dB]')
```

9.5.3 M-file of the simulations in Figure 16.

Following M-file is to generate the effect of the changes in stiffness and thickness to the MTSM response (relative Δf and α) in harmonics. Simulations of different harmonics can be done by giving a different harmonic value to the variable, n, in the M-file.

For the relative Δf simulation of MTSM in harmonics

```
%----- Info. about TSM sensor -------
uq=2.947e10;
rq=2651;
vq=(uq/rq)^.5;
L=1.67e-4;
%--------- Info. about Film ------------------
nf=0.1;              %thickness
rf=1000;             %density
[hf,uf]=meshgrid([1e-7:1e-8:1e-5],[1e6:1e5:1e8]);
vf=(uf./rf).^.5;
%------ Info. about 1st harmonic --------------
n=1;      %harmonic
f0=1e7*n;
w=2*pi*f0;
kq=w/vq;
k=w*(rf^2./(uf.^2+(w*nf)^2)).^.25.*cos(-.5*atan(w*nf./uf));
a=-w*(rf^2./(uf.^2+(w*nf)^2)).^.25.*sin(-.5*atan(w*nf./uf));
kf=k-j*a;
df=(f0/(n*pi))*atan(((-kf.*(uf+j*w*nf)).*tan(kf.*hf))/(uq*kq));
rdf=real(df);             %real part of df
Rrdf=rdf/f0;              %relative changes
mesh(hf,uf,Rrdf);
xlabel('Thickness [m]')
```

```
ylabel('Stiffness [N/m^2]')
zlabel('Relative Changes in Res. Freq.')
```

For the α simulation of MTSM in harmonics

```
clear;
uq=2.947e10;                    %TSM stiffness
rq=2651;                        %TSM density
nq=3.5e-4;                      %TSM viscosity
vq=(uq/rq)^.5;
e22=3.982e-11;
r=2.5e-3;                       %radius of 10 MHz MAIB
area=pi*r^2;
K2=7.74e-3;
[hf,uf]=meshgrid([1e-7:1e-8:1e-5],[1e6:1e5:1e8]);
rf=1000;                        %film density
nf=1e-1;
% 1st Harmonic=======================================================
N=7;       %harmonic
f0=1e7*N;
w=2*pi*f0;
kq=w/vq;
k=w*(rf^2./(uf.^2+(w*nf)^2)).^.25.*cos(-.5*atan(w*nf./uf));
a=-w*(rf^2./(uf.^2+(w*nf)^2)).^.25.*sin(-.5*atan(w*nf./uf));
kf1=k-j*a;
df=(f0/(N*pi))*atan(((-kf1.*(uf+j*w*nf)).*tan(kf1.*hf))/(uq*kq));
ResF=f0+real(df);
Realw=2*pi*ResF;
L=1.67e-4;
C0=e22*area/L;
C1=8*K2*C0/(N*pi)^2;
L1=1/(w^2*C1);
R1=nq/(uq*C1);
ueff=uf+(j*Realw*nf);
kf=Realw.*(rf./ueff).^.5;
```

```
Zm=j*(ueff*rf).^.5.*tan(kf.*hf);
A=N*pi./(4*K2*w*C0);
B=N*pi./(4*K2*w.^2*C0);
R2=A.*real(Zm)./(rq*uq)^.5;
L2=B.*imag(Zm)./(rq*uq)^.5;
Zq=R1+(1./(j*Realw*C1))+(j*Realw*L1);
Ze=R2+(j*Realw.*L2);
Zs=Zq+Ze;
Z0=1./(j*Realw.*C0);
Zt=(Zs.*Z0)./(Zs+Z0);
MagZt=100./(100+Zt);
RMagZt=real(MagZt);
IMagZt=imag(MagZt);
MZt=(RMagZt.^2+IMagZt.^2).^.5;
atte=20*log10(MZt);
mesh(hf,uf,-atte);
xlabel('Thickness [m]')
ylabel('Stiffness [N/m^2]')
zlabel('Attenuation [dB]')
```

9.5.4 M-file of the simulations in Figure 18.

Following M-file is to generate the effect of the changes in stiffness and viscosity to the MTSM response (relative Δf and α) in harmonics. Simulations of different harmonics can be done by giving a different harmonic value to the variable, n, in the M-file.

For the relative Δf simulation of MTSM in harmonics

```
%----- Info. about TSM sensor -------
uq=2.947e10;
rq=2651;
vq=(uq/rq)^.5;
```

```
L=1.67e-4;
%--------- Info. about Film ------------------
hf=1e-5;              %thickness
rf=1000;             %density
[nf,uf]=meshgrid([1e-3:1e-4:.1],[1e6:1e5:1e8]);
vf=(uf./rf).^.5;
n=1;      %harmonic
f0=1e7*n;
w=2*pi*f0;
kq=w/vq;
k=(w*((rf^2)./(uf.^2+(w^2*nf.^2))).^.25).*cos(-.5*atan((w.*nf)./uf));
a=(w*((rf^2)./(uf.^2+(w^2*nf.^2))).^.25).*sin(-.5*atan((w.*nf)./uf));
kf=k-j*a;
df=(f0/(n*pi))*atan(((-kf.*(uf+j*w*nf)).*tan(kf.*hf))/(uq*kq));
rdf=real(df);            %real part of df
Rrdf=rdf/f0;             %relative changes
mesh(uf,nf,Rrdf);
xlabel('Stiffness [m]')
ylabel('Viscosity [kg/ms]')
zlabel('Relative Changes in Res. Freq.')
```

For the α simulation of MTSM in harmonics

```
clear;
uq=2.947e10;                      %TSM stiffness
rq=2651;                         %TSM density
nq=3.5e-4;                        %TSM viscosity
vq=(uq/rq)^.5;
e22=3.982e-11;
r=2.5e-3;                        %radius of 10 MHz MAIB
area=pi*r^2;
K2=7.74e-3;
[nf,uf]=meshgrid([1e-3:1e-4:.1],[1e6:1e5:1e8]);
rf=1000;                         %film density
hf=1e-5;
N=1;      %harmonic
```

```
f0=1e7*N;
w=2*pi*f0;
kq=w/vq;
k=w*(rf^2./(uf.^2+(w*nf).^2)).^.25.*cos(-.5*atan(w*nf./uf));
a=-w*(rf^2./(uf.^2+(w.*nf).^2)).^.25.*sin(-.5*atan(w*nf./uf));
kf1=k-j*a;
df=(f0/(N*pi))*atan(((-kf1.*(uf+j*w*nf)).*tan(kf1*hf))/(uq*kq));
ResF=f0+real(df);
Realw=2*pi*ResF;
L=1.67e-4;
C0=e22*area/L;
C1=8*K2*C0/(N*pi)^2;
L1=1/(w^2*C1);
R1=nq/(uq*C1);
ueff=uf+(j*Realw.*nf);
kf=Realw.*(rf./ueff).^.5;
Zm=j*(ueff*rf).^.5.*tan(kf*hf);
A=N*pi./(4*K2*w*C0);
B=N*pi./(4*K2*w.^2*C0);
R2=A.*real(Zm)./(rq*uq)^.5;
L2=B.*imag(Zm)./(rq*uq)^.5;
Zq=R1+(1./(j*Realw*C1))+(j*Realw*L1);
Ze=R2+(j*Realw.*L2);
Zs=Zq+Ze;
Z0=1./(j*Realw*C0);
Zt=(Zs.*Z0)./(Zs+Z0);
MagZt=100./(100+Zt);
RMagZt=real(MagZt);
IMagZt=imag(MagZt);
MZt=(RMagZt.^2+IMagZt.^2).^.5;
atte=20*log10(MZt);
mesh(uf,nf,-atte);
xlabel('Stiffness [N/m^2]')
ylabel('Viscosity [kg/ms]')
zlabel('Attenuation [dB]')
```

9.5.5 M-file of the simulations in Figure 20.

Following M-file is to generate the effect of the changes in density to the MTSM response (relative Δf and α) in harmonics.

For the relative Δf simulation of MTSM in harmonics

```
hold on
%----- Info. about TSM sensor -------
uq=2.947e10;
rq=2651;
vq=(uq/rq)^.5;
L=1.67e-4;
%--------- Info. about Film ------------------
h=1e-6;          %thickness
uf=1e8;          %stiffness
rf=500:1:2000;     %density
nf=0.1;         %viscosity
vf=(uf./rf).^.5;
%------ Info. about 1st harmonic --------------
n=1;      %harmonic
f0=1e7*n;
w=2*pi*f0;
kq=w/vq;
k=w*(rf.^2/(uf^2+(w*nf)^2)).^.25*cos(-.5*atan(w*nf/uf));
a=-w*(rf.^2/(uf^2+(w*nf)^2)).^.25*sin(-.5*atan(w*nf/uf));
kf=k-j*a;
df=(f0/(n*pi))*atan(((-kf.*(uf+j*w*nf)).*tan(kf*h))/(uq*kq));
rdf=real(df);          %real part of df
Rrdf=rdf/f0;           %relative changes
plot(rf,Rrdf,'-')
xlabel('Density [kg/m^3]')
ylabel('Delta Freq. [Hz]')
%------ Info. about 3rd harmonic --------------
n=3;      %harmonic
```

```
f0=1e7*n;
w=2*pi*f0;
kq=w/vq;
k=w*(rf.^2/(uf^2+(w*nf)^2)).^.25*cos(-.5*atan(w*nf/uf));
a=-w*(rf.^2/(uf^2+(w*nf)^2)).^.25*sin(-.5*atan(w*nf/uf));
kf=k-j*a;
df=(f0/(n*pi))*atan(((-kf.*(uf+j*w*nf)).*tan(kf*h))/(uq*kq));
rdf=real(df);         %real part of df
Rrdf=rdf/f0;          %relative changes
plot(rf,Rrdf,'--')
%------ Info. about 5th harmonic --------------
n=5;      %harmonic
f0=1e7*n;
w=2*pi*f0;
kq=w/vq;
k=w*(rf.^2/(uf^2+(w*nf)^2)).^.25*cos(-.5*atan(w*nf/uf));
a=-w*(rf.^2/(uf^2+(w*nf)^2)).^.25*sin(-.5*atan(w*nf/uf));
kf=k-j*a;
df=(f0/(n*pi))*atan(((-kf.*(uf+j*w*nf)).*tan(kf*h))/(uq*kq));
rdf=real(df);         %real part of df
Rrdf=rdf/f0;          %relative changes
plot(rf,Rrdf,':')
%------ Info. about 7th harmonic --------------
n=7;      %harmonic
f0=1e7*n;
w=2*pi*f0;
kq=w/vq;
k=w*(rf.^2/(uf^2+(w*nf)^2)).^.25*cos(-.5*atan(w*nf/uf));
a=-w*(rf.^2/(uf^2+(w*nf)^2)).^.25*sin(-.5*atan(w*nf/uf));
kf=k-j*a;
df=(f0/(n*pi))*atan(((-kf.*(uf+j*w*nf)).*tan(kf*h))/(uq*kq));
rdf=real(df);         %real part of df
Rrdf=rdf/f0;          %relative changes
plot(rf,Rrdf,'-.')
```

For the α simulation of MTSM in harmonics

```
clear;
uq=2.947e10;                    %TSM stiffness
rq=2651;                        %TSM density
nq=3.5e-4;                      %TSM viscosity
vq=(uq/rq)^.5;
e22=3.982e-11;
r=2.5e-3;                       %radius of 10 MHz MAIB
area=pi*r^2;
K2=7.74e-3;
hf=1e-6;
uf=1e8;
rf=500:1:2000;                        %film density
nf=.1;
vf=(uf./rf).^.5;
% 1 H ========================
N=1;      %harmonic
f0=1e7*N;
w=2*pi*f0;
kq=w/vq;
k=w*(rf.^2/(uf^2+(w*nf)^2)).^.25*cos(-.5*atan(w*nf/uf));
a=-w*(rf.^2/(uf^2+(w*nf)^2)).^.25*sin(-.5*atan(w*nf/uf));
kf1=k-j*a;
df=(f0/(N*pi))*atan(((-kf1*(uf+j*w*nf)).*tan(kf1*hf))/(uq*kq));
ResF=f0+real(df);
Realw=2*pi*ResF;
L=1.67e-4;
C0=e22*area/L;
C1=8*K2*C0/(N*pi)^2;
L1=1/(w^2*C1);
R1=nq/(uq*C1);
ueff=uf+(j*Realw*nf);
kf=Realw.*(rf./ueff).^.5;
Zm=j*(ueff.*rf).^.5.*tan(kf*hf);
A=N*pi/(4*K2*w*C0);
```

```
B=N*pi/(4*K2*w^2*C0);
R2=A*real(Zm)/(rq*uq)^.5;
L2=B*imag(Zm)/(rq*uq)^.5;
Zq=R1+(1./(j*Realw*C1))+(j*Realw*L1);
Ze=R2+(j*Realw.*L2);
Zs=Zq+Ze;
Z0=1./(j*Realw*C0);
Zt=(Zs.*Z0)./(Zs+Z0);
MagZt=100./(100+Zt);
RMagZt=real(MagZt);
IMagZt=imag(MagZt);
MZt=(RMagZt.^2+IMagZt.^2).^.5;
atte=20*log10(MZt);
plot(rf,-atte,'-'); hold on;
xlabel('Density [kg/m^3]')
ylabel('Attenuation [dB]')
% 3 H ==============
N=3;       %harmonic
f0=1e7*N;
w=2*pi*f0;
kq=w/vq;
k=w*(rf.^2/(uf^2+(w*nf)^2)).^.25*cos(-.5*atan(w*nf/uf));
a=-w*(rf.^2/(uf^2+(w*nf)^2)).^.25*sin(-.5*atan(w*nf/uf));
kf1=k-j*a;
df=(f0/(N*pi))*atan(((-kf1*(uf+j*w*nf)).*tan(kf1*hf))/(uq*kq));
ResF=f0+real(df);
Realw=2*pi*ResF;
L=1.67e-4;
C0=e22*area/L;
C1=8*K2*C0/(N*pi)^2;
L1=1/(w^2*C1);
R1=nq/(uq*C1);
ueff=uf+(j*Realw*nf);
kf=Realw.*(rf./ueff).^.5;
Zm=j*(ueff.*rf).^.5.*tan(kf*hf);
A=N*pi/(4*K2*w*C0);
```

```
B=N*pi/(4*K2*w^2*C0);
R2=A*real(Zm)/(rq*uq)^.5;
L2=B*imag(Zm)/(rq*uq)^.5;
Zq=R1+(1./(j*Realw*C1))+(j*Realw*L1);
Ze=R2+(j*Realw.*L2);
Zs=Zq+Ze;
Z0=1./(j*Realw*C0);
Zt=(Zs.*Z0)./(Zs+Z0);
MagZt=100./(100+Zt);
RMagZt=real(MagZt);
IMagZt=imag(MagZt);
MZt=(RMagZt.^2+IMagZt.^2).^.5;
atte=20*log10(MZt);
plot(rf,-atte,'--'); hold on;
% 5 H ==============
N=5;       %harmonic
f0=1e7*N;
w=2*pi*f0;
kq=w/vq;
k=w*(rf.^2/(uf^2+(w*nf)^2)).^.25*cos(-.5*atan(w*nf/uf));
a=-w*(rf.^2/(uf^2+(w*nf)^2)).^.25*sin(-.5*atan(w*nf/uf));
kf1=k-j*a;
df=(f0/(N*pi))*atan(((-kf1*(uf+j*w*nf)).*tan(kf1*hf))/(uq*kq));
ResF=f0+real(df);
Realw=2*pi*ResF;
L=1.67e-4;
C0=e22*area/L;
C1=8*K2*C0/(N*pi)^2;
L1=1/(w^2*C1);
R1=nq/(uq*C1);
ueff=uf+(j*Realw*nf);
kf=Realw.*(rf./ueff).^.5;
Zm=j*(ueff.*rf).^.5.*tan(kf*hf);
A=N*pi/(4*K2*w*C0);
B=N*pi/(4*K2*w^2*C0);
R2=A*real(Zm)/(rq*uq)^.5;
```

```
L2=B*imag(Zm)/(rq*uq)^.5;
Zq=R1+(1./(j*Realw*C1))+(j*Realw*L1);
Ze=R2+(j*Realw.*L2);
Zs=Zq+Ze;
Z0=1./(j*Realw*C0);
Zt=(Zs.*Z0)./(Zs+Z0);
MagZt=100./(100+Zt);
RMagZt=real(MagZt);
IMagZt=imag(MagZt);
MZt=(RMagZt.^2+IMagZt.^2).^.5;
atte=20*log10(MZt);
plot(rf,-atte,':'); hold on;
% 7 H ==============
N=7;       %harmonic
f0=1e7*N;
w=2*pi*f0;
kq=w/vq;
k=w*(rf.^2/(uf^2+(w*nf)^2)).^.25*cos(-.5*atan(w*nf/uf));
a=-w*(rf.^2/(uf^2+(w*nf)^2)).^.25*sin(-.5*atan(w*nf/uf));
kf1=k-j*a;
df=(f0/(N*pi))*atan(((-kf1*(uf+j*w*nf)).*tan(kf1*hf))/(uq*kq));
ResF=f0+real(df);
Realw=2*pi*ResF;
L=1.67e-4;
C0=e22*area/L;
C1=8*K2*C0/(N*pi)^2;
L1=1/(w^2*C1);
R1=nq/(uq*C1);
ueff=uf+(j*Realw*nf);
kf=Realw.*(rf./ueff).^.5;
Zm=j*(ueff.*rf).^.5.*tan(kf*hf);
A=N*pi/(4*K2*w*C0);
B=N*pi/(4*K2*w^2*C0);
R2=A*real(Zm)/(rq*uq)^.5;
L2=B*imag(Zm)/(rq*uq)^.5;
Zq=R1+(1./(j*Realw*C1))+(j*Realw*L1);
```

```
Ze=R2+(j*Realw.*L2);
Zs=Zq+Ze;
Z0=1./(j*Realw*C0);
Zt=(Zs.*Z0)./(Zs+Z0);
MagZt=100./(100+Zt);
RMagZt=real(MagZt);
IMagZt=imag(MagZt);
MZt=(RMagZt.^2+IMagZt.^2).^.5;
atte=20*log10(MZt);
plot(rf,-atte,'-.'); hold off;
```

9.5.6 M-file of the simulations in Figure 23.

Following M-file is to generate the Case A ($\theta \approx 0°$) in Figure 22: A signature of the viscosity (η) driven process.

For the relative Δf simulation of MTSM in harmonics

```
%----- Info. about TSM sensor -------
clear;
uq=2.947e10;
rq=2651;
vq=(uq/rq)^.5;
L=1.67e-4;
%--------- Info. about Film ------------------
hf=1e-5;              %thickness
rf=1000;             %density
uf=1e6;
%uf=1e6:9090.9:1e7;
nf=1e-3:1e-4:.1;
vf=(uf/rf).^.5;
x=1:.1:100;
%------ Info. about 1st harmonic --------------
n=1;       %harmonic
f0=1e7*n;
```

```
w=2*pi*f0;
kq=w/vq;
k=w*(rf^2./(uf.^2+(w*nf).^2)).^.25.*cos(-.5*atan(w*nf./uf));
a=-w*(rf^2./(uf.^2+(w*nf).^2)).^.25.*sin(-.5*atan(w*nf./uf));
kf=k-j*a;
df=(f0/(n*pi))*atan(((-kf.*(uf+j*w*nf)).*tan(kf*hf))/(uq*kq));
rdf=real(df);             %real part of df
Rrdf=rdf/f0;              %relative changes
plot(x,Rrdf,'-'); hold on;
xlabel('Normalized Axis of Stiffness and viscosity')
ylabel('Relative Changes in Res. Freq.')
%------ Info. about 3rd harmonic --------------
n=3;       %harmonic
f0=1e7*n;
w=2*pi*f0;
kq=w/vq;
k=w*(rf^2./(uf.^2+(w*nf).^2)).^.25.*cos(-.5*atan(w*nf./uf));
a=-w*(rf^2./(uf.^2+(w*nf).^2)).^.25.*sin(-.5*atan(w*nf./uf));
kf=k-j*a;
df=(f0/(n*pi))*atan(((-kf.*(uf+j*w*nf)).*tan(kf*hf))/(uq*kq));
rdf=real(df);             %real part of df
Rrdf=rdf/f0;              %relative changes
plot(x,Rrdf,'--'); hold on;
%----------Info. about 5th harmonic -------------
n=5;       %harmonic
f0=1e7*n;
w=2*pi*f0;
kq=w/vq;
k=w*(rf^2./(uf.^2+(w*nf).^2)).^.25.*cos(-.5*atan(w*nf./uf));
a=-w*(rf^2./(uf.^2+(w*nf).^2)).^.25.*sin(-.5*atan(w*nf./uf));
kf=k-j*a;
df=(f0/(n*pi))*atan(((-kf.*(uf+j*w*nf)).*tan(kf*hf))/(uq*kq));
rdf=real(df);             %real part of df
Rrdf=rdf/f0;              %relative changes
plot(x,Rrdf,':'); hold on;
%-----------Info. about 7th harmonic -------------------------
```

```
n=7;       %harmonic
f0=1e7*n;
w=2*pi*f0;
kq=w/vq;
k=w*(rf^2./(uf.^2+(w*nf).^2)).^.25.*cos(-.5*atan(w*nf./uf));
a=-w*(rf^2./(uf.^2+(w*nf).^2)).^.25.*sin(-.5*atan(w*nf./uf));
kf=k-j*a;
df=(f0/(n*pi))*atan(((-kf.*(uf+j*w*nf)).*tan(kf*hf))/(uq*kq));
rdf=real(df);              %real part of df
Rrdf=rdf/f0;               %relative changes
plot(x,Rrdf,'-.'); hold on;
```

For the α simulation of MTSM in harmonics

```
clear;
uq=2.947e10;                    %TSM stiffness
rq=2651;                        %TSM density
nq=3.5e-4;                      %TSM viscosity
vq=(uq/rq)^.5;
e22=3.982e-11;
r=2.5e-3;                       %radius of 10 MHz MAIB
area=pi*r^2;
K2=7.74e-3;
hf=1e-5;
rf=1000;                        %film density
uf=1e6;
%uf=1e6:9090.9:1e7;
vf=(uf./rf).^.5;
nf=1e-3:1e-4:.1;
x=1:.1:100;
% 1st Harmonic=================================================
N=1;       %harmonic
f0=1e7*N;
w=2*pi*f0;
kq=w/vq;
k=w*(rf^2./(uf.^2+(w*nf).^2)).^.25.*cos(-.5*atan(w*nf./uf));
```

```
a=-w*(rf^2./(uf.^2+(w*nf).^2)).^.25.*sin(-.5*atan(w*nf./uf));
kf=k-j*a;
df=(f0/(N*pi))*atan(((-kf.*(uf+j*w*nf)).*tan(kf*hf))/(uq*kq));
ResF=f0+real(df);
Realw=2*pi*ResF;
L=1.67e-4;
C0=e22*area/L;
C1=8*K2*C0/(N*pi)^2;
L1=1/(w^2*C1);
R1=nq/(uq*C1);
ueff=uf+(j*Realw.*nf);
kf=Realw.*(rf./ueff).^.5;
Zm=j*(ueff*rf).^.5.*tan(kf.*hf);
A=N*pi./(4*K2*Realw*C0);
B=N*pi./(4*K2*Realw.^2*C0);
R2=A.*real(Zm)./(rq*uq)^.5;
L2=B.*imag(Zm)./(rq*uq)^.5;
Zq=R1+(1./(j*w*C1))+(j*w*L1);
Ze=R2+(j*Realw.*L2);
Zs=Zq+Ze;
Z0=1./(j*w*C0);
Zt=(Zs.*Z0)./(Zs+Z0);
RZt=real(Zt);
IZt=imag(Zt);
MZt=(RZt.^2+IZt.^2).^.5;
atte=20*log10(100./(100+MZt));
plot(x,-atte,'-'); hold on;
xlabel('Normalized Axis of Stiffness and viscosity')
ylabel('Attenuation [dB]')
%=================================================================
N=3;       %harmonic
f0=1e7*N;
w=2*pi*f0;
kq=w/vq;
k=w*(rf^2./(uf.^2+(w*nf).^2)).^.25.*cos(-.5*atan(w*nf./uf));
a=-w*(rf^2./(uf.^2+(w*nf).^2)).^.25.*sin(-.5*atan(w*nf./uf));
```

```
kf=k-j*a;
df=(f0/(N*pi))*atan(((-kf.*(uf+j*w*nf)).*tan(kf*hf))/(uq*kq));
ResF=f0+real(df);
Realw=2*pi*ResF;
L=1.67e-4;
C0=e22*area/L;
C1=8*K2*C0/(N*pi)^2;
L1=1/(w^2*C1);
R1=nq/(uq*C1);
ueff=uf+(j*Realw.*nf);
kf=Realw.*(rf./ueff).^.5;
Zm=j*(ueff*rf).^.5.*tan(kf.*hf);
A=N*pi./(4*K2*Realw*C0);
B=N*pi./(4*K2*Realw.^2*C0);
R2=A.*real(Zm)./(rq*uq)^.5;
L2=B.*imag(Zm)./(rq*uq)^.5;
Zq=R1+(1./(j*w*C1))+(j*w*L1);
Ze=R2+(j*Realw.*L2);
Zs=Zq+Ze;
Z0=1./(j*w*C0);
Zt=(Zs.*Z0)./(Zs+Z0);
RZt=real(Zt);
IZt=imag(Zt);
MZt=(RZt.^2+IZt.^2).^.5;
atte=20*log10(100./(100+MZt));
plot(x,-atte,'--'); hold on;
%=============================================================
N=5;       %harmonic
f0=1e7*N;
w=2*pi*f0;
kq=w/vq;
k=w*(rf^2./(uf.^2+(w*nf).^2)).^.25.*cos(-.5*atan(w*nf./uf));
a=-w*(rf^2./(uf.^2+(w*nf).^2)).^.25.*sin(-.5*atan(w*nf./uf));
kf=k-j*a;
df=(f0/(N*pi))*atan(((-kf.*(uf+j*w*nf)).*tan(kf*hf))/(uq*kq));
ResF=f0+real(df);
```

```
Realw=2*pi*ResF;
L=1.67e-4;
C0=e22*area/L;
C1=8*K2*C0/(N*pi)^2;
L1=1/(w^2*C1);
R1=nq/(uq*C1);
ueff=uf+(j*Realw.*nf);
kf=Realw.*(rf./ueff).^.5;
Zm=j*(ueff*rf).^.5.*tan(kf.*hf);
A=N*pi./(4*K2*Realw*C0);
B=N*pi./(4*K2*Realw.^2*C0);
R2=A.*real(Zm)./(rq*uq)^.5;
L2=B.*imag(Zm)./(rq*uq)^.5;
Zq=R1+(1./(j*w*C1))+(j*w*L1);
Ze=R2+(j*Realw.*L2);
Zs=Zq+Ze;
Z0=1./(j*w*C0);
Zt=(Zs.*Z0)./(Zs+Z0);
RZt=real(Zt);
IZt=imag(Zt);
MZt=(RZt.^2+IZt.^2).^.5;
atte=20*log10(100./(100+MZt));
plot(x,-atte,':');
%=================================================================
N=7;       %harmonic
f0=1e7*N;
w=2*pi*f0;
kq=w/vq;
k=w*(rf^2./(uf.^2+(w*nf).^2)).^.25.*cos(-.5*atan(w*nf./uf));
a=-w*(rf^2./(uf.^2+(w*nf).^2)).^.25.*sin(-.5*atan(w*nf./uf));
kf=k-j*a;
df=(f0/(N*pi))*atan(((-kf.*(uf+j*w*nf)).*tan(kf*hf))/(uq*kq));
ResF=f0+real(df);
Realw=2*pi*ResF;
L=1.67e-4;
C0=e22*area/L;
```

```
C1=8*K2*C0/(N*pi)^2;
L1=1/(w^2*C1);
R1=nq/(uq*C1);
ueff=uf+(j*Realw.*nf);
kf=Realw.*(rf./ueff).^.5;
Zm=j*(ueff*rf).^.5.*tan(kf.*hf);
A=N*pi./(4*K2*Realw*C0);
B=N*pi./(4*K2*Realw.^2*C0);
R2=A.*real(Zm)./(rq*uq)^.5;
L2=B.*imag(Zm)./(rq*uq)^.5;
Zq=R1+(1./(j*w*C1))+(j*w*L1);
Ze=R2+(j*Realw.*L2);
Zs=Zq+Ze;
Z0=1./(j*w*C0);
Zt=(Zs.*Z0)./(Zs+Z0);
RZt=real(Zt);
IZt=imag(Zt);
MZt=(RZt.^2+IZt.^2).^.5;
atte=20*log10(100./(100+MZt));
plot(x,-atte,'-.'); hold off;
```

VITA

Name:	Sun Jong Kwoun
Place of Birth:	Seoul, Korea
Education:	Drexel University, Philadelphia, PA Master of Science in Biomedical Engineering 09/1997 – 08/2001 Advisor: Drs. Ryszard M. Lec and Frank K. Ko Drexel University, Philadelphia, PA Bachelor of Science in Electrical and Computer Engineering 09/1992 - 06/1997

Publications:

1. Sun Jong Kwoun, R. M. Lec, R. A. Cairncross, P. Shah & C. J. Brinker "Characterization of superhydrophobic materials using multiresonance acoustic shear wave sensors" IEEE Transactions on Ultrasonics, Ferroelectrics, and Frequency Control, vol. 53, pp. 1400-1403, 2006.

2. Sun Jong Kwoun, R. M. Lec, R. A. Cairncross, P. Shah & C. J. Brinker "The Study of Interaction of Superhydrophobic (SH) Materials with Fluids using TSM sensors" - Proceedings of the 2005 IEEE International Frequency Control Symposium and Exposition, 2005. 29-31 Aug. 2005 pp. 78-83.

3. Sun Jong Kwoun, Baohua Han, Frank K. Ko, and Ryszard M. Lec "A novel polymer nanofiber interface for chemical sensor applications" IEEE/EIA International Frequency Control Symposium and Exhibition, p. 51-57, Kansas City, MI, USA, June 7-9, 2000.